Photoelectron Spectroscopy Studies of Anionic Clusters: CO_2 Reduction, Metal Hydrides, Low Barrier Hydrogen Bonding, and Solvent Stabilization

by

Jacob David Graham

A dissertation submitted to Johns Hopkins University in conformity with the requirements for the degree of Doctor of Philosophy

Baltimore, Maryland

September 2015

Abstract

Anion photoelectron spectroscopy was combined with theoretical studies to examine the electronic and geometric properties of negative ions. A diverse range of negative ions were studied including metal hydrides, complexes with a CO_2 moiety and systems containing strong, low barrier hydrogen bonds. In particular, the intermolecular bonding in the above negative ions is a central theme of this thesis. In certain cases, the additional electron occupies a molecular bonding orbital that stabilizes the entire anionic complex. This scenario is identified in both the organic complex $(Quinoline\text{-}CO_2)^-$ and aluminum hydride AlH_4^- where the removal of an electron changes these species into van der Waals complexes. In other cases, ionic bonding is found to be the dominant interaction in a negative ion complex. Examples of such systems studied include $(Cobalt\text{-}Pyridine\text{-}CO_2)^-$ and dimers of deprotonated acids that form low barrier hydrogen bonds such as the formate-formic acid anion. Selected dissociation energies in the above described complexes are examined. Additionally, the stabilizing effect of water on several unstable anions is studied. These include hydrated forms of formaldehyde, acetaldehyde and acetone anions.

Research Advisor: Dr. Kit H. Bowen

Readers: Dr. Harris J. Silverstone

Dr. Art Bragg

Acknowledgments

I would first like to thank my research advisor, Dr. Kit Bowen. He is an incredibly kind and thoughtful person combined with excellent scientific mind. He has always provided his graduate students with the support and guidance necessary for success, and this was no exception in my case. For any problem, both inside and outside the lab, Kit always seems to know a part of the problem you haven't considered and what to do about it.

I would like to thank Allyson Buytendyk who has been my lab partner for the vast majority of my graduate school career. We generally approach problems differently and our joint solutions are better for it. Many of the experiments described in this thesis were made possible due to her insights, cleverness and general pragmatism.

Dr. Di Wang and Dr. Andrej Grubisic's instrumental upgrades to the Pulsed Source Apparatus made nearly all of my graduate work possible. I'm thankful that they've been incredibly helpful in troubleshooting various issues with the instrument and providing general advice.

I would like to also thank the entire Bowen group for the supportive environment they create. Colin Xhang is a very creative scientist who can always bring clarity to a problem I'm having. Yi Wang is always friendly and willing to help. Xin Tang and Zachary Hicks are the acting surface chemists of the group and have valuable advice and viewpoints. Evan Collins is extremely selfless when doling out his time helping others, and his determination when bulldozing through obstacles is an impressive sight. Ryan Wood's machining help, scientific discussions and general personality made many lab days easier.

Recent graduates Dr. Jing Chen, Dr. Angela Buonaugurio, Dr. Haopeng Wang, Dr. Xiang Li, and Dr. Sarah Stokes have all been supportive both before and after leaving the group.

Sandy Ciborowski and Gaoxiang Liu are the new faces of the Pulsed Source Apparatus and are quickly picking up the experimental acumen necessary for the instrument. They are both excellent learners (with insightful questions) and look to have a promising careers in the group. Nic Blando and Sara Marquez are also very positive additions to the group and are learning quickly.

Both Dr. Bob Compton and Dr. Nathan Hammer, my former undergraduate research advisor, have been invaluable resources for our implementing Rydberg electron transfer. They have always been willing to sit down and explain many experimental aspects that probably seem obvious to them.

I would also like to thank the departmental facilities manager, Boris Steinberg, who has been an invaluable resource.

Finally, I would like to thank my family for the encouragement they've given me throughout my Ph.D. And last but certainly not least, I would like to thank my wife, Jennifer, whose unconditional love and support I can always rely on.

Table of Contents

List of Tables

List of Figures

I. Introduction

The study of fundamental interactions between electrons and matter is useful to a wide variety of seemingly unrelated fields ranging from CO_2 sequestration to enzyme catalysis. Negative ions have an excess electron relative to their neutral counterpart and as such they are examples of how an electron perturbs and interacts with neutral complexes. Negative ions can take the form of atoms, molecules or clusters with clusters being aggregates of molecules or atoms. Clusters are particularly interesting as they lie in a region between the atomic and bulk and are ideal for studying interatomic or intermolecular interactions. A single excess electron interacting with a cluster can cause a variety of chemistry to occur such as proton transfer or bond formation.

Negative ions are amenable to many powerful experimental techniques since they can be accelerated and manipulated by electric and magnetic fields. Our lab uses a combination of mass spectrometry and photoelectron spectroscopy to study the electronic structure of isolated anions. Negative ion photoelectron spectroscopy is conducted by crossing a mass selected beam of anions with a fixed frequency photon beam. The kinetic energies of photodetached electrons are governed by the energy conserving relationship:

$$h\nu = EBE + EKE$$

where hν is the photon energy, EBE is the electron binding energy, and EKE is the kinetic energy of the photodetached electron. Although the above relationship does not include the recoil energy of the now neutral molecule or cluster, conservation of momentum causes the much lighter electron to carry away nearly all of the kinetic energy,

and this recoil energy can be omitted. Since the photon energy is known, measurement of the electron's kinetic energy allows one to determine electron binding energies.

Since photodetachment is a fast process, relative photoelectron intensities are governed by the Franck-Condon overlap between the ground-state anion and neutral electronic states. An idealized potential energy diagram for neutral and anionic states of a diatomic molecule is shown in Figure III.1.1. The adiabatic electron affinity or AEA is the energetic difference between the ground-state anion and the ground-state neutral. If there is very large geometrical change (and thus very poor Franck-Condon overlap) between the ground-state anion and the ground-state neutral, this transition may not be observed. Additionally, vertical detachment energy (VDE) is defined as a photodetachment transition from the ground-state anion to the region on the neutral potential energy surface with the maximum Franck-Condon overlap and as such this transition is the most intense transition observed in a photoelectron spectrum. Determining the AEA and VDE can provide many insights into the nature of an anionic species.

The work in this thesis is split into several chapters. **Chapter II** describes the experimental aspects typical of pulsed negative ion photoelectron spectroscopy. A description of pulsed ion sources, time-of-flight mass spectroscopy and electron energy analyzers is presented.

Chapter III of this thesis concerns CO_2 binding in the presence of a negative charge. CO_2 reduction is an important topic in developing CO_2 sequestration methods. A combination of anion photoelectron spectroscopy and density functional calculations was

used to assess CO_2 binding in both Quinoline-CO_2 and Cobalt-Pyridine-CO_2 anionic complexes. In Quinoline-CO_2 it is shown that an excess electron increases the binding energy from 0.16 eV to 0.64 eV. For Cobalt-Pyridine-CO_2 it is found that ionic bonding is the dominant characteristic and the CO_2 moiety bound by 1.41 eV.

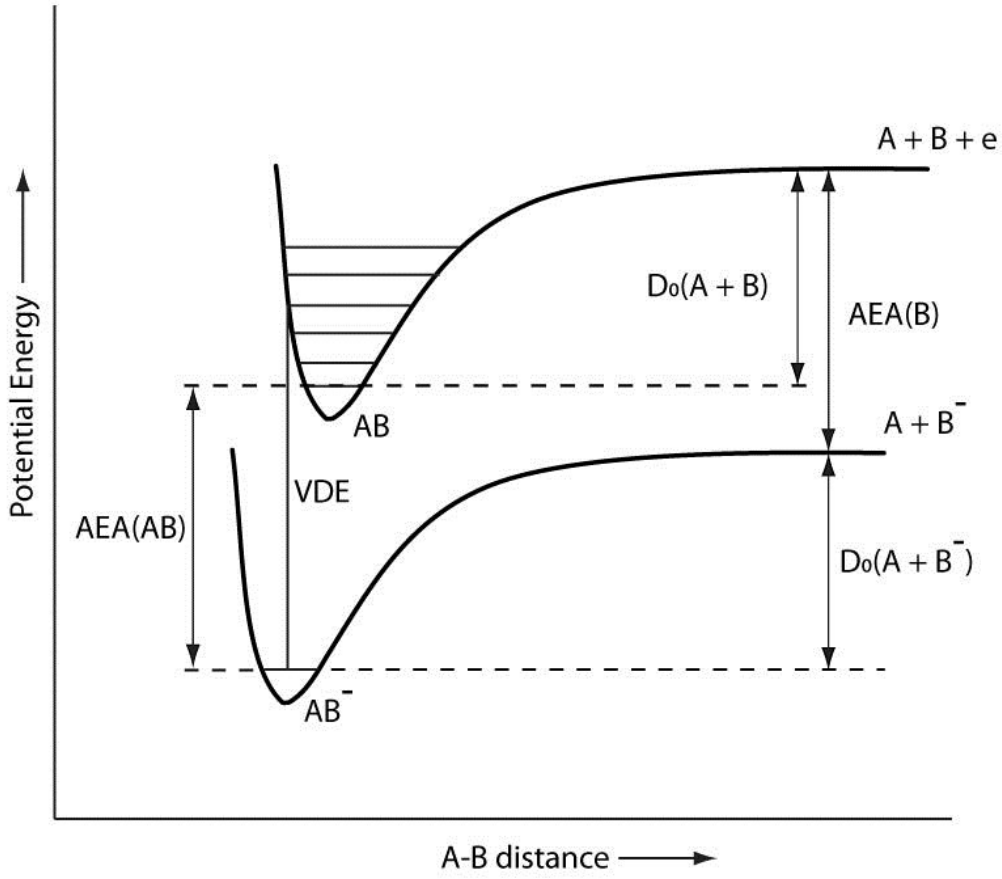

Figure III.1.1: Potential energy diagram

Chapter IV of this thesis presents work involving metal hydride systems. AlH_4^- is a common anion encountered by organic chemists in the reducing agent lithium aluminum hydride, however little study has been performed on the anion in isolation. We

have measured its vertical detachment energy and performed extensive calculations on its electronic structure. It was determined that removing the excess electron completely destabilizes the molecule. The magnesium hydride (MgH^-) anion and its deuterated form (MgD^-) are also studied. Magnesium hydrides may have future hydrogen storage applications and the photoelectron spectra of these diatomic molecules are compared to the results of high-level *ab-initio* calculations.

Strong, low barrier hydrogen bonding (LBHB) is discussed in **Chapter V**. In a LBHB, a proton is shared between anions whose conjugate acids have matching pK_a values. By examining shifts in photoelectron spectra we are able to compare the binding energy of several enzymatically relevant systems including: formate-formic acid, acetate-acetic acid, imidazolide-imidazole, and phenol-phenolate anionic complexes relative to the HF_2^- complex which has the strongest known hydrogen bond. Even the weakest bound of these, the imidazolide-imidazole anion, was shown to have a binding energy of nearly half that of the HF_2^- complex. Although these experiments provide upper limits to what strengths may be available inside an enzyme active site, they do reinforce the feasibility of low barrier hydrogen bonds playing a role in enzyme catalysis.

Solvent stabilization of unstable anions is discussed in **Chapter VI**. Here, we examine the stabilization effect water has on the formaldehyde, acetaldehyde, and acetone anions by stepwise hydration. We observe the minimum number of water molecules necessary to stabilize the anions to be 2, 3, and 4 for formaldehyde, acetaldehyde, and acetone, respectively. Photoelectron spectra of observed clusters were

recorded and various methods to extrapolate the negative electron affinity of the monomer are discussed.

Lastly, the **Appendix** of this thesis discusses the instrument upgrades performed to the instrument to add Rydberg electron transfer capability. Several example anionic systems generated by Rydberg electron transfer are shown.

II. Experimental Methods

As introduced in the preceding section, negative ion photoelectron spectroscopy is conducted by crossing a mass selected beam of anions with a fixed frequency photon beam. Such an experiment can be divided into three successive steps: anion formation, mass selection, and photodetachment. Most of the experiments described in this thesis were performed on the Pulsed Source Apparatus (PSA) which combines an anion source vacuum chamber, a time-of-flight mass spectrometer and two types of electron kinetic energy analyzers (magnetic bottle and velocity map imaging). This instrument operates in a pulsed manner (10 Hz) meaning that mass selection and photodetachment can rely on time-of-flight methods which are described later. Additionally, high power pulsed lasers can be used for both anion sources and photodetachment.

Anions are generally more difficult to prepare than cations, and successfully generating an anionic species is typically the most difficult part of an anion photoelectron spectroscopy experiment. By necessity, this lab has developed and implemented a wide range of anion sources. A small sampling of ion sources available in our lab would include laser vaporization, pulsed arc cluster ionization source (PACIS), and more recently Rydberg electron transfer.

Our laser vaporization ion source involves ablating a rotating and translating metal rod with the focused output (532 nm) of a Nd:YAG laser. A pulsed valve (backed by helium) then opens for 200 microseconds. As this gas expands, material ablated off the metal rod condenses and cools forming clusters with varying charge states. The

output of this source is directed through a skimmer and into the time-of-flight mass spectrometer. A side view schematic of this source is shown in Figure III.1.1. Additionally, mixed cluster systems can be generated by seeding the helium carrier gas with another gas (like CO_2) or high vapor pressure samples (like formic acid).

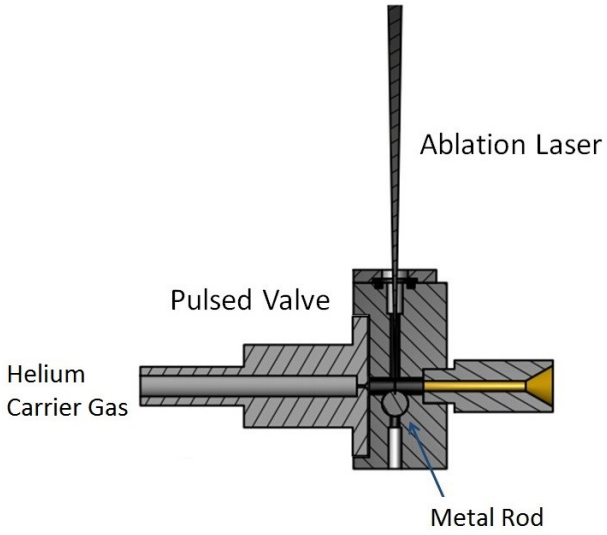

Figure III.1.1: Laser Vaporization Ion Source

The pulsed arc cluster ionization source (PACIS) is uniquely suited to generating metal hydride anions. The PACIS uses a 30 microsecond long, 150 V electrical discharge from an anode to a metal cathode while simultaneously admitting hydrogen carrier gas through a pulsed valve. The discharge produces a high density region of free metal atoms, electrons, and free hydrogen atoms. This mixture is directed down a 20 cm long tube where they react and cool before exiting into high vacuum. A schematic of the PACIS source is shown in Figure III.1.2.

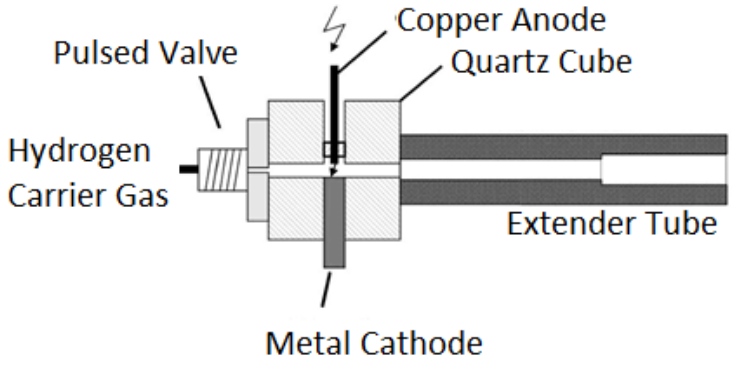

Figure III.1.2: Pulsed Arc Cluster Ionization Source

Rydberg electron transfer (RET) is the most recent anion source available and involves the collisional transfer of an electron from a highly excited Rydberg atom to a target neutral species. In our version of RET, Rydberg atoms are generated by laser excitation of potassium atoms. In many other laboratories this anion "source" was an experiment itself and adding Rydberg electron transfer capability was a large undertaking. Details regarding our RET setup are in the appendix of this thesis.

Ions are mass analyzed with time-of-flight mass spectrometry which is performed by accelerating ions to a uniform kinetic energy and recording the time the ions take to a travel a fixed distance. Since the kinetic energy of a moving particle is given by:

$$KE = \frac{1}{2}m\left(\frac{d}{t}\right)^2$$

where m is the mass of the particle, d is the distance traveled and t is the total flight time of the particle. Two ions traveling the same distance with the same kinetic energy will have a total travel time proportional to the square root of their mass ratio. Combining the

above equation with the kinetic energy of a charged particle in a uniform electric field and solving for t yields:

$$t = \frac{d}{\sqrt{2Vq}}\sqrt{m}$$

where V is the accelerating voltage and q is the charge of the particle. Reducing the constants in this equation to a proportionality constant, C, yields:

$$t = C\sqrt{m}$$

Ions are accelerated by high voltage (~1.5 kilovolts) pulses applied to extraction plates arranged using de Heer's ion acceleration method.[1] De Heer's arrangement is a modification of the standard Wiley and McLaren[2] setup and is optimized for a large ion extraction volume. The spread in initial ion position is compensated by using two acceleration regions. Because the temporal spread between ions is small (microseconds) for a laboratory sized apparatus (meters) an ion detector must have a very fast temporal response which is achieved using microchannel plate detectors.

To guarantee that only one mass is photodetached during an experimental run, a time-of-flight mass spectrometer needs a method of discriminating against other masses. As time-of-flight mass spectrometry spreads ions temporarily and not spatially, a single mass-to-charge ratio can be selected using a pulsed electric field. This instrument uses a "mass gate" which is a series of three girds that the ions must pass through before entering either photodetachment region. The mass gate is designed so that the first and last grid are held at ground potential, while the central grid is biased (-1.7 kilovolts) to

reject ions. This bias is momentarily grounded at the exact moment when a sought after mass passes through.

There are two types of electron kinetic energy analyzers installed on this instrument. The first is termed a magnetic bottle.[3] In this arrangement photodetached electrons are born in the presence of a strong diverging magnetic field that is coupled to a uniform and lengthy (~3 meters) magnetic field. These electrons are guided along the magnetic field lines towards a microchannel plate detector. Since all detected electrons travel the same distance and have the same mass, their kinetic energy can be determined from their arrival time. Doppler broadening is the major source of electron energy spread and is reduced through ion deceleration. This instrument employs an ion deceleration scheme developed by Gantefoer[4] that simultaneously focuses the ion beam while decelerating.

Another technique for measuring the kinetic energy of photodetached electrons is velocity map imaging.[5,6] Here, photodetached electrons are accelerated by an electric field towards a position sensitive detector. This position sensitive detector is a large active area microchannel plate coupled to a phosphor screen and CCD camera. This detector records a 2D projection of the 3D expansion of photoelectrons. Through an inverse Abel transform (BASEX)[7] one can reconstruct the initial 3D expansion and obtain a photoelectron spectrum. Our co-linear velocity map imaging arrangement does not suffer from the Doppler broadening of the magnetic bottle technique and additionally records the anisotropy of photodetached electrons.

References

1. W. A. de Heer and P. Milani Rev. Sci. Instrum. 62, 670 (1991).

2. W. C. Wiley and I. H. McLaren, Rev. Sci. Instrum. 26, 1150 (1955).

3. P. Kruit and F. H. Read, J. Phys. E Sci. Instrum. 16, 313 (1983).

4. C.-Y. Cha, G. Gantefoer, and W. Eberhardt, Rev. Sci. Instrum. 63, 5661 (1992).

5. D. W. Chandler and P. L. Houston, J. Chem. Phys. 87 1445 (1987).

6. A. T. J. B. Eppink and D. H. Parker, Rev. Sci. Instrum. 68, 3477 (1997).

7. V. Dribinski, A. Ossadtchi, V. A. Mandelshtam and H. Reisler, Rev. Sci. Instrum. **73**, 2634 (2002).

III. CO_2 Binding in Anionic Complexes

The rising concentration of CO_2 in Earth's atmosphere has motivated a flurry of research regarding CO_2 capture and sequestration. However, the relative inertness of CO_2 makes capture a difficult and expensive process. Current industrial scale methods involve CO_2 absorption by aqueous alkanolamine solutions with several promising advanced methods involving adsorption by highly porous metal organic frameworks. Many of these methods involve a thermochemical cycle between capture and regeneration and are therefore energetically costly.

However, the study of an excess negative charge interacting with CO_2 (i.e. CO_2 reduction) may suggest an electrochemical route to CO_2 capture. While CO_2 is metastable as a negative ion, CO_2 can interact strongly with other species when negatively charged. Seong Kim (Seoul National University) demonstrated this with his study of $(\text{pyridine-}CO_2)^-$ anions. Both pyridine and CO_2 are unable to individually bind an electron, however when clustered together strongly bind an excess electron. Kim postulated that the excess electron filled a binding molecular orbital between the two moieties. This single electron is able to switch the complex from a van der Waals interaction into a covalent interaction.

Kim's original studies involved anionic complexes of CO_2 and either pyrazine, pyridazine, pyrimidine or triazine. Here, CO_2's carbon atom binds to the nitrogen atom of these N-Heterocycle complexes. While it would be instructive to study the dissocation energy of each N-Heterocycle-CO_2 anionic complex, the negative electron affinity of each N-Heterocycle molecule complicates determinations of binding energy with both

experimental and theoretical methods. Quinoline, however, is a N-Heterocyclic complex that possesses a positive electron affinity. We have generated the Quinoline-CO_2 anionic complex, and through a combination of anion photoelectron spectroscopy and density functional theory calculations found a bond dissociation energy of 0.64 eV.

Additionally, we chose to study the (Cobalt-Pyridine-CO_2)$^-$ anionic complex as a primitive model of CO_2 binding to a negatively charged metal organic. Again, this cluster was studied through combination of anion photoelectron spectroscopy and density function theory. Here, we studied several dissociation pathways, and found CO_2 to be strongly bound with a binding energy of 1.42 eV.

III.1 CO_2 Binding in the (Quinoline-CO_2)$^-$ Anionic Complex

Jacob Graham, Allyson Buytendyk, Yi Wang, and Kit H. Bowen, Jr.

Department of Chemistry, Johns Hopkins University, Baltimore, MD 21218, USA

Seong Keun Kim

Department of Chemistry, Seoul National University, Seoul, 151-747, Korea

III.1.1 Introduction

Carbon dioxide has long been known to bind weakly to certain amines[1], and more recently it has been found to bind to some metal organic frameworks (MOFs).[2] Carbon dioxide also forms gas-phase, anionic complexes with several atoms and molecules.[3-27] In the $[CO_2(H_2O)]^-$ anionic complex, for example, an intact CO_2^- sub-anion is stabilized by its interaction with water.[3,4] In seminal work, using a combination of mass spectrometry, photoelectron spectroscopy, and *ab initio* calculations, Kim and coworkers[5] found significant covalent character in the intermolecular bond between CO_2 and pyridine in the gas phase (Pyridine-CO_2)$^-$ anionic complex. Vibrational predissociation studies by Johnson and coworkers[6] confirmed its structure and the covalent bonding character inferred by Kim. In further studies with CO_2 and the heterocyclic nitrogen molecules: pyrazine, pyridazine, pyrimidine, triazine, and 2-aminopyridine, analogously bonded binary anionic complexes were also found.[7,8]

In all these cases, bonding took place between the carbon atom in CO_2 and a nitrogen atom in its heterocyclic molecular partner. From a Lewis acid-base perspective, the heterocycle's nitrogen atom, i.e., its lone electron pair, was the electron donor and CO_2 was the electron acceptor, both well-known properties of these constituents. As neutral adducts some degree of binding would have been expected, but with the addition of excess electrons, robust binary anionic complexes were formed. Kim referred to the process by which this occurs as "associative electron attachment", i.e., where a chemical bond was formed due to electron attachment, even though there was no such bond in the corresponding neutral.[7] In each of the cases considered here, bond formation was likely due to delocalization of the excess electron over both the heterocycle's ring and the CO_2 moiety, i.e., over the entire molecular framework. This helps to rationalize why even though neither CO_2 nor any of its above-mentioned partners possess positive adiabatic electron affinities, together, they formed stable anionic complexes.

While covalent bonding character has been demonstrated for (N-Heterocycle-CO_2)$^-$ anionic complexes, carbon dioxide's binding energy there has not. Neither of the experimental techniques used to study them could have provided that information, and theoretical calculations were stymied by the necessity of dealing with molecules having negative adiabatic electron affinities. Quinoline, on the other hand, is different from the other N-heterocyclic molecules listed above in that it has a positive adiabatic electron affinity (0.16 eV).[28] This affords an opportunity to determine carbon dioxide's binding energy in the (Quinoline-CO_2)$^-$ anionic complex and by implication to estimate it in other (N-Heterocycle-CO_2)$^-$ anionic complexes as well. In the work presented here, we used a combination of mass spectrometry, anion photoelectron spectroscopy, and density

functional calculations to study the (Quinoline-CO_2)$^-$ anionic complex and to identify a value for carbon dioxide's binding energy there.

III.1.2 Experimental and Computational Methods

Anion photoelectron spectroscopy is conducted by crossing a mass-selected beam of negative ions with a fixed-frequency photon beam and energy-analyzing the resultant photodetached electrons. The photodetachment process is governed by the relationship hν = EBE + EKE, where hν is the photon energy, EBE is the electron binding energy, i.e., the transition energy between the anion and a particular vibronic state of its neutral counterpart, and EKE is the electron kinetic energy.

Negative ions of quinoline were formed in a biased (-500 V) supersonic expansion nozzle-ion source, where the quinoline sample was placed in the source's stagnation chamber, heated to 70 °C, and co-expanded with ~2 atmospheres of argon gas through a 23 μm orifice into a vacuum maintained at 10^{-4} Torr. Simultaneously, CO_2 was admitted very near the nozzle on its vacuum side and allowed to mix with the jet. Negative ions were formed by injecting low energy electrons from an even more negatively-biased, thoriated-iridium filament into the expanding jet, where a micro-plasma was formed in the presence of a weak axial magnetic field. The resulting anions were then extracted, collimated, and transferred into the flight tube of a 90° magnetic sector mass spectrometer with a mass resolution of 400. Mass-selected anions of (Quinoline-CO_2)$^-$ were then crossed with the intra-cavity laser beam of an argon ion laser (~100 Watts), while photodetached electrons were energy-analyzed in a hemispherical electron energy analyzer having a resolution of 20 meV.[29] The photoelectron spectrum

reported here was recorded with 2.540 eV photons (488 nm), and it was calibrated against the photoelectron spectrum of the O^- anion. An identical photoelectron spectrum of $(Quinoline\text{-}CO_2)^-$ was also observed in our lab using a pulsed anion photoelectron spectrometer that employed time-of-flight mass selection, a Nd:YAG laser, and a magnetic bottle electron energy analyzer.[30]

Density functional theory (DFT) calculations were conducted using the Gaussian 09 software package.[31] All calculations were performed using the wb97xd functional[32] and Aug-CC-pVTZ basis set.[33,34] Geometry optimizations were performed without symmetry constraints and were followed by vibrational frequency calculations to verify the identification of stationary points and to obtain zero point energies.

III.1.3 Results

The photoelectron spectrum of the $(Quinoline\text{-}CO_2)^-$ anionic complex is presented in Figure III.1.1. This spectrum consists of a single broad band with an onset at EBE ~1.3 eV and an intensity maximum at EBE = 1.8 eV, the latter being its vertical detachment energy (VDE). Unlike the vibrationally-structured photoelectron spectrum of the quinoline molecular anion,[28] no vibrational features were resolved in the photoelectron spectrum of the $(Quinoline\text{-}CO_2)^-$ anionic complex.

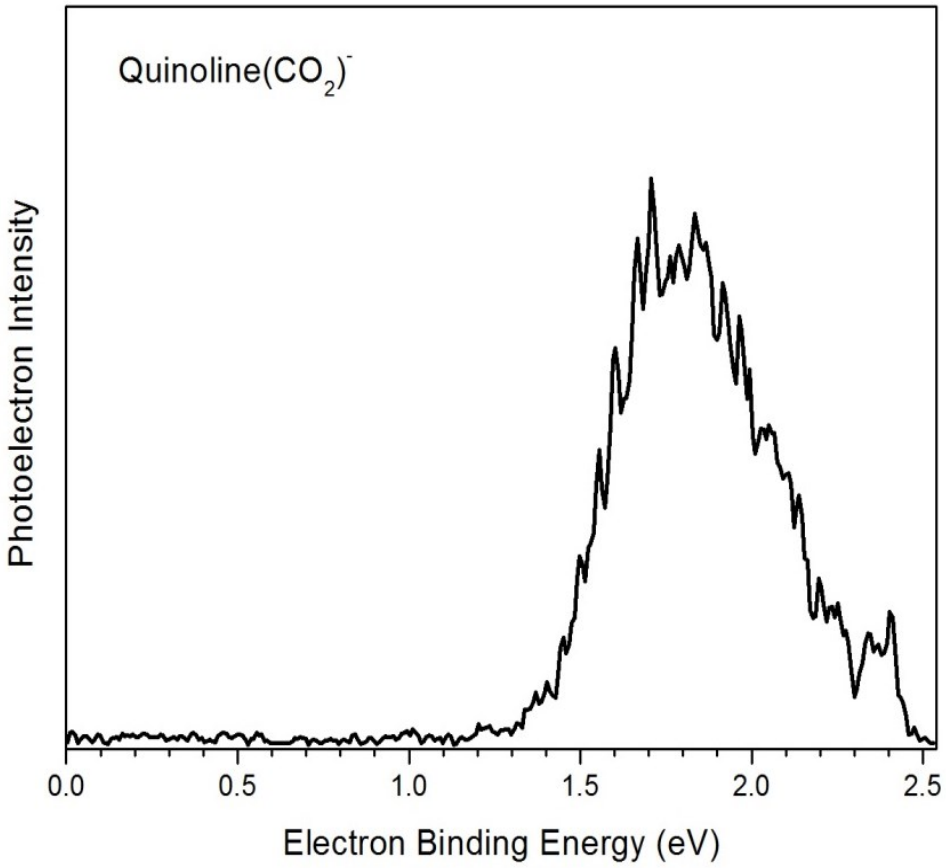

Figure III.1.1: The anion photoelectron spectrum of the (Quinoline-CO_2)$^-$ anionic complex recorded with 488 nm photons.

Figure III.1.2 presents the optimized geometries that we calculated for both the $(Quinoline\text{-}CO_2)^-$ anionic complex (Fig. 2A) and the $Quinoline\text{-}CO_2$ neutral complex (Fig. 2B). As can be seen in Fig. 2A, the C-N bond length in the $(Quinoline\text{-}CO_2)^-$ anionic complex is 1.55 Å and its CO_2 moiety is bent by 132^0. By comparison, the C-N bond distance in the $Quinoline\text{-}CO_2$ neutral complex is 2.83 Å. These structural parameters are quite similar to those of $(Pyridine\text{-}CO_2)^-$ and $(Pryridine\text{-}CO_2)$. Kim[5] and Johnson[6] calculated the C-N bond length in the $(Pyridine\text{-}CO_2)^-$ anionic complex to be 1.46 Å and 1.52 Å, respectively, while Leopold[35] measured the C-N bond distance in the $Pyridine\text{-}CO_2$ neutral complex to be 2.798 Å. Furthermore, based on a Natural Population Analysis (NPA), we found the negative charge on the quinoline moiety to be 0.41*e,* while that on the CO_2 moiety is 0.59*e*. Even though the excess negative charge is delocalized over the entire anionic complex, it is somewhat more localized on the CO_2 moiety than on the quinoline moiety. Figure III.1.3 presents the highest occupied molecular orbital (HOMO) of the $(Quinoline\text{-}CO_2)^-$ anionic complex. While both the HOMO and NPA approaches indicate electron delocalization over the whole complex, they are mapping different aspects of excess electron density.

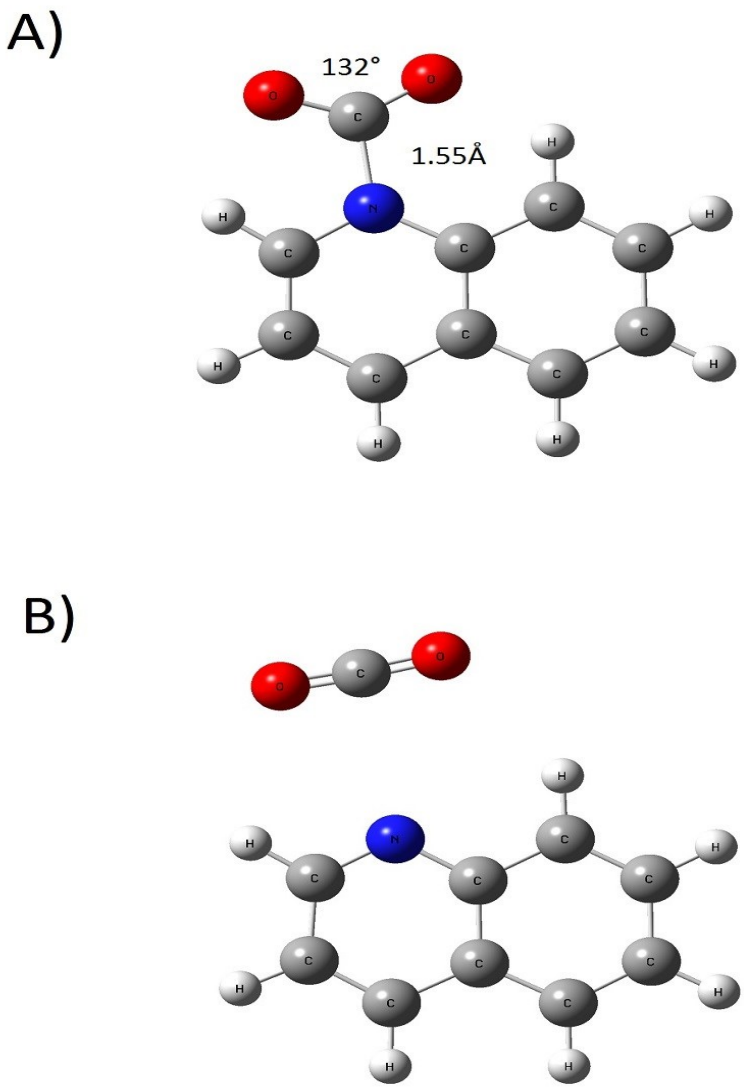

Figure III.1.2: Relaxed geometries of (A) the $(Quinoline\text{-}CO_2)^-$ anionic complex and (B) the $Quinoline\text{-}CO_2$ neutral complex.

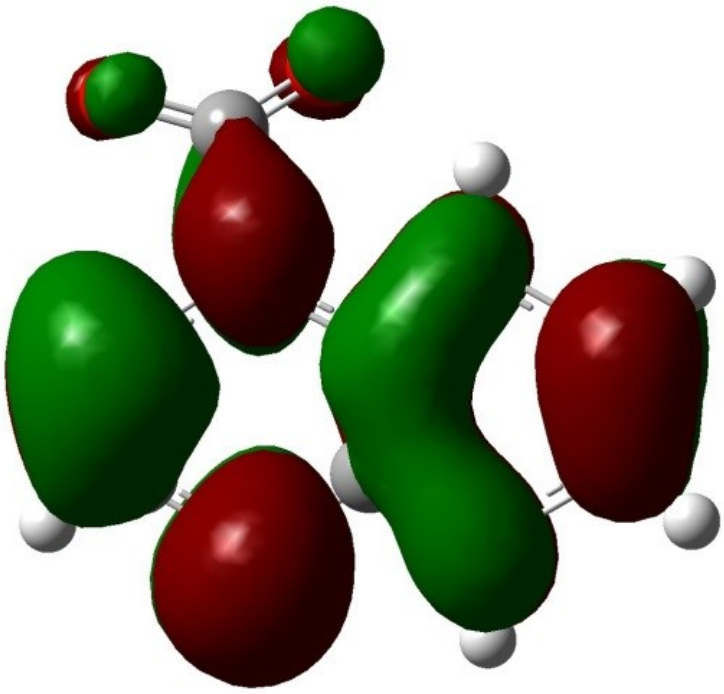

Figure III.1.3: The highest occupied molecular orbital (HOMO) of the (Quinoline-CO_2)$^-$ anionic complex.

The energy difference between the (Quinoline-CO_2)$^-$ anionic complex in its relaxed geometry and the Quinoline-CO_2 neutral complex in that same geometry is the VDE value. Our calculated VDE of 1.77 eV is in very good agreement with the experimentally observed value of 1.8 eV. We also calculated the zero-point corrected, adiabatic electron affinity (EA) of Quinoline-CO_2 and found it to be 0.67 eV. However, due to the geometry difference between the relaxed structure of the anionic complex (Fig. 2A) and that of its neutral counterpart (Fig. 2B), it would not be surprising if Franck-Condon overlap between the two were to be insufficient for the origin transition to be observed in the experimental spectrum. That appears to be the case, since no significant

features were seen in the spectrum in the vicinity of EBE = 0.67 eV. Thus, the EA value of the Quinoline-CO_2 complex could not be determined from the photoelectron spectrum alone.

Additionally, the zero-point corrected adiabatic electron affinity of quinoline itself was calculated to be 0.19 eV, compared with our experimental value of 0.16 eV.[28] Since the latter value derives from a straightforward assignment of our vibrationally-structured photoelectron spectrum of the quinolone molecular anion and is thus probably quite accurate, the 0.03 eV discrepancy between theory and experiment is probably a measure of the accuracy of our calculations. Relevant values are summarized in Table III.1.1.

Table III.1.1 Experimental and Calculated Electron Affinities and Vertical Detachment Energies for Quinoline and Quinoline-CO_2 Complexes.

	Exp EA	Calc EA	Calc EA with ZPE	Exp VDE	Calc VDE
Quinoline	0.16[a]	0.05[a]	0.19[a]	--------	---------
Quinoline-CO_2	<1.3	0.64	0.67	1.8	1.77

(a) ref. 28

III.1.4 Discussion

How strongly is CO_2 bound in the (Quinoline-CO_2)$^-$ anionic complex? Initially, we had hoped to determine this from the thermochemical relationship,

$$D_0(\text{Quinoline-}CO_2)^- = EA(\text{Quinoline-}CO_2) - EA(\text{Quinoline}) + D_0(\text{Quinoline-}CO_2) \quad (1)$$

using our experimental values for EA (Quinoline-CO_2) and EA (Quinoline) and a calculated value for D_0 (Quinoline-CO_2), which was in any case expected to be relatively small. This approach, however, could not be used when the origin transition failed to appear in the photoelectron spectrum of the (Quinoline-CO_2)$^-$ anionic complex, due to a lack of Franck-Condon overlap.

We then turned to a computational approach. Theoretical attempts to calculate the binding energy of CO_2 in the earlier mentioned (N-Heterocycle-CO_2)$^-$ anionic complexes would have been stymied by the difficulty of dealing with molecules having negative adiabatic electron affinities, i.e., both CO_2 and the N-heterocyclic molecules mentioned above. Quinoline, on the other hand, possesses a positive adiabatic electron affinity, and that made it possible for us to calculate the absolute energy of its anion. The dissociation energy of the (Quinoline-CO_2)$^-$ anionic complex, D_0 (Quinoline-CO_2)$^-$, breaking into the quinoline molecular anion, (Quinoline)$^-$ and CO_2, is given by:

$$D_0 [(\text{Quinoline-}CO_2)^-] = E [(\text{Quinoline})^-] + E [CO_2] - E [(\text{Quinoline-}CO_2)^-] \quad (2)$$

where E [M] refers to the calculated absolute energy of species, M, in its relaxed geometry and with its zero point energy included. From this approach, D_0[(Quinoline-CO_2)$^-$] was found to be 0.64 eV.

Likewise, the dissociation energy of the (Quinoline-CO_2) neutral complex, D_0 (Quinoline-CO_2), breaking into the neutral quinoline molecule and CO_2, is given by:

$$D_0 [(\text{Quinoline-}CO_2)] = E [\text{Quinoline}] + E [CO_2] - E [(\text{Quinoline-}CO_2)] \quad (3)$$

where again E [M] refers to the calculated absolute energy of species, M, in its relaxed geometry and with its zero point energy included. In this way, D_0 [(Quinoline-CO_2)] was found to be 0.16 eV. By comparison, the binding energy of the Pyridine-CO_2 neutral complex has been calculated to be 0.10 - 0.20 eV.[36] The fact that our calculated and measured values for EA (Quinoline), i.e., 0.19 eV and 0.16 eV, respectively, are so close to one another provides reassurance in the validity of the calculations.

Our results indicate that carbon dioxide is bound by 0.64 eV in the (Quinoline-CO_2)$^-$ anionic complex. This suggests that the earlier discussed (N-Heterocycle-CO_2)$^-$ anionic complexes also have comparable CO_2 binding energies. Following Kim's and Johnson's conclusions that the (Pyridine-CO_2)$^-$ anionic complex exhibits significant covalent bonding character, it seems likely that the (Quinoline-CO_2)$^-$ anionic complex does too. Still, 0.64 eV is well below the bond strength of a most covalent bonds. On the other hand, it is much stronger than a van der Waals bond and also stronger than most hydrogen bonds. A binding energy of 0.64 eV lies in an intermediate range, i.e., along a continuum of bond strengths between those of van der Waals and chemical interactions. It fits best among the interaction strengths of Lewis acid-base pairs (adducts). For neutral-neutral complexes, these span binding energies form ~0.2 eV to significantly over an electron volt.[37,38] For binary complexes with net negative charges, however, there are few signposts to guide us within the context of Lewis acid-base pairs. Perhaps, the best we have are $O_2^-(CO_2)$ and $NO^-(CO_2)$, which could be thought of as Lewis acid-base pairs and whose binding energies have been measured[16] or calculated[39] to be 0.82 eV and 0.9 eV, respectively. Like (Quinoline-CO_2)$^-$, their non-CO_2 moieties form stable negative ions, but unlike (Quinoline-CO_2)$^-$, neither $O_2^-(CO_2)$ nor $NO^-(CO_2)$ can significantly

delocalize their excess charges. In fact, both $O_2^-(CO_2)$ and $NO^-(CO_2)$ might better be considered to be ion-molecule complexes. By contrast, because all the (N-Heterocycle-$CO_2)^-$ anionic complexes discussed here owe their stabilities to their ability to delocalize their excess charges, they belong to a distinct class of negatively-charged complexes.

For CO_2, taking on partial negative charge means that it must bend to a corresponding degree and correspondingly bending presumes the acquisition of negative charge density. They are two side of the same coin; for CO_2, bending and accepting negative charge are synonymous. This relationship lies at the heart of CO_2 activation, and it is much in evidence in the binding of CO_2 within (N-Heterocycle-$CO_2)^-$ anionic complexes.

Acknowledgements

We thank Alex Boldyrev and Ken Leopold for valuable correspondence on this topic. This research was supported in part by the U.S. Department of Energy, Office of Basic Energy Sciences, Division of Chemical Sciences, Geosciences and Biosciences under Award DE-FG02-12ER16362. This material is also based in part on work supported by the U. S. National Science Foundation under grant number CHE-1360692. This work was also supported in part by the Global Frontier R&D Program of the Center for Multi-Scale Energy Systems funded by the National Research Foundation under grant number, NRF-2014M3A6A7060583 (SKK).

References

1. G. Astarita, *Chem. Engr, Sci,* **16**, 202-207 (1961).

2. K. Sumida, D. L. Rogow, J.A. Mason, T. M. McDonald, E. D. Bloch, Z. R. Herm, T-H. Bae, and J. R. Long, *Chem. Rev*. **112**, 724-781 (2012).

3. C. E. Klots, *J. Chem. Phys.* **71**, 4172 (1979).

4. T. Tsukuda and T. Nagata, *J. Phys, Chem. A* **107**, 8476 (2003).

5. S. Y. Han, I. Chu, J. H. Kim, J. K. Song, and S. K. Kim, *J. Chem. Phys*. **113**, 596 (2000).

6. M. Z. Kamrath, R. A. Relph, and M. A. Johnson, *J. Am. Chem. Soc.* **132**, 15508 (2010).

7. S. H. Lee, N. Kim, D. G. Ha, and S. K. Kim, *J. Am. Chem. Soc*. **130**, 16241 (2008).

8. N. Kim, *Bull. Korean Chem. Soc*. **34**, 2247 (2013).

9. M. J. DeLuca, B. Niu, and M. A. Johnson, *J. Chem. Phys*. **88**, 5857 (1988).

10. S. H. Fleischman and K. D. Jordan, *J. Phys. Chem.* **91**, 1300 (1987).

11. T. Tsukuda, M. A. Johnson, and T. Nagata, *Chem. Phys. Lett.* **268**, 429 (1997).

12. J. W. Shin, N. I. Hammer, M. A. Johnson, H. Schneider, A. Glöβ, and J.M. Weber, *J. Phys. Chem. A* **109**, 3146 (2005).

13. D. W. Arnold, S. E. Bradforth, E. H. Kim, D. M. Neumark, *J. Chem. Phys.* **102**, 3493 (1995).

14. H. Schneider, A. D. Boese, and J. M. Weber*, J. Chem. Phys.* **123**, 074316 (2005).

15. A. Muraoka, Y. Inokuchi, N. I. Hammer, J,-W, Shin, M. A. Johnson, and T. Nagata, *J. Phys, Chem. A* **113**, 8942 (2009).

16. K. Hiraoka and S. Yamabe, *J. Chem. Phys.* **97**, 643 (1992).

17. K. Sudoh, Y. Matsuyama, A. Muraoka, R. Nakanishi, and T. Nagata, *Chem. Phys, Lett.* **433** 10-14 (2006).

18. T. Sanford, S.-Y. Han, M. A. Thompson, R. Parson, and W.C. Lineberger, *J. Chem. Phys.* **122**, 054307 (2005).

19. J. M. Weber, *Int. Rev. Phys. Chem*. **33**, 489 (2014).

20. A. D. Boese, H. Schneider, A. N. Glöß, and J. M. Weber, *J. Chem. Phys.* **122**, 154301 (2005).

21. B. J. Knurr and J. M. Weber, *J. Am. Chem. Soc.* **134**, 18804 (2012).

22. B. J. Knurr and J. M. Weber, *J. Phys. Chem. A* **118**, 4056 (2014).

23. B. J. Knurr and J. M. Weber, *J. Phys. Chem. A* **118,** 10246 (2014).

24. B. J. Knurr and J. M. Weber, *J. Phys. Chem. A* **118**, 8753 (2014).

25. R,F. Hoeckebdorf, K. Fischmann, Q. Hao, C. v.d. Linde, O. P, Balaj, C-K. Siu, and M. K. Beyer, *Intern. J. Mass Spectro*. **354**, 175 (2013).

26. A. Akhgarnusch, R. F. Hoeckebdorf, Q. Hao, K. P. Jaeger, C-K. Siu, and M. K. Beyer, *Angew, Chem. Int. Ed.* **53**, 9327 (2013).

27. A. Akhgarnusch and M. K. Beyer, *Intern. J. Mass Spectro*. **365**, 295 (2014).

28. A. M. Buytendyk, Y. Wang, J. D. Graham, A. K. Kandalam, B. Kiran and K. H. Bowen, *Molecular Physics*. (2015) [DOI: 10.1080/00268976.2014.1003261].

29. J. V. Coe, J. T. Snodgrass, C. B. Freidhoff, K. M. McHugh, and K. H. Bowen, *J. Chem. Phys.,* **87**, 4302-4309 (1987).

30. D. Wang, J.D. Graham, A.M. Buytendyk, and K.H. Bowen, *J. Chem. Phys*., **135**, 164308 (2011).

31. Gaussian 09, Revision A.2, M. J. Frisch, G. W. Trucks, H. B. Schlegel, G. E. Scuseria, M. A. Robb, J. R. Cheeseman, G. Scalmani, V. Barone, B. Mennucci, G. A. Petersson, H. Nakatsuji, M. Caricato, X. Li, H. P. Hratchian, A. F. Izmaylov, J. Bloino, G. Zheng, J. L. Sonnenberg, M. Hada, M. Ehara, K. Toyota, R. Fukuda, J. Hasegawa, M. Ishida, T. Nakajima, Y. Honda, O. Kitao, H. Nakai, T. Vreven, J. A. Montgomery, Jr., J. E. Peralta, F. Ogliaro, M. Bearpark, J. J. Heyd, E. Brothers, K. N. Kudin, V. N. Staroverov, R. Kobayashi, J. Normand, K. Raghavachari, A. Rendell, J. C. Burant, S. S. Iyengar, J. Tomasi, M. Cossi, N. Rega, J. M. Millam, M. Klene, J. E. Knox, J. B. Cross, V. Bakken, C. Adamo, J. Jaramillo, R. Gomperts, R. E. Stratmann, O. Yazyev, A. J. Austin, R. Cammi, C. Pomelli, J. W. Ochterski, R. L. Martin, K. Morokuma, V. G. Zakrzewski, G. A. Voth, P. Salvador, J. J. Dannenberg, S. Dapprich, A. D. Daniels, Ö. Farkas, J. B. Foresman, J. V. Ortiz, J. Cioslowski, and D. J. Fox, Gaussian, Inc., Wallingford CT, 2009.

32. J.-D. Chai and M. Head-Gordon, *Phys. Chem. Chem. Phys*., **10**, 6615-20 (2008).

33. D. E. Woon and T. H. Dunning, Jr. *J. Chem. Phys*. **90**, 1007 (1989).

34. D. E. Woon and T. H. Dunning, Jr. *J. Chem. Phys*. **98**, 1358 (1993).

35. J. L. Doran B. Hon and K. R. Leopold, *J. Mol. Struct.* **1019**, 191 (2012).

36. K. D. Vogiatzis, A. M.avrandonakis, W. Klopper, G. E. Froudakis, *ChemPhysChem.* **10**, 374 (2009).

37. K. R. Leopold, *Adv. Mol. Struct. Res.* **2**, 103 (1996).

38. K. R. Leopold, M. Canagaratna, and J. A. Philips, *Accts. Chem. Res.* **30**, 57 (1997).

39. M. Zhou, L. Zhang, and Q. Qin, *J. Am Chem. Soc.* **122**, 4483 (2000).

III.2 Carbon Dioxide is Tightly Bound in the [Co(Pyridine)(CO2)]- Anionic Complex

Jacob D. Graham, Allyson M. Buytendyk, Xinxing Zhang, and Kit H. Bowen, Jr.

Department of Chemistry, Johns Hopkins University, Baltimore, MD 21218, USA

Seong K. Kim

Department of Chemistry, Seoul National University, Seoul, 151-747, Korea

III.2.1 Abstract

The $[Co(Pyridine)(CO_2)]^-$ anionic complex is studied through a combination of photoelectron spectroscopy and density functional calculations. This complex can be thought of as a primitive model system for CO_2 binding to a metal organic in the presence of an excess electron. The anion complex is identified as having a central cobalt atom with pyridine and CO_2 moieties arranged as ligands. The relatively large 2.7 eV vertical detachment energy of the complex suggests that the species is strongly interacting and calculated dissociation energies indicate CO_2 is particularly strongly bound with removal of a CO_2 having an high energy barrier of 1.42 eV.

III.2.2 Introduction

After Kim and co-workers first established that an excess electron induces covalent bonding in the Pyridine-CO_2 complex,[1] subsequent work provided strong evidence of covalent bonding in other negatively-charged complexes composed of CO_2

and the heterocyclic nitrogen molecules: pyrazine, pyridazine, pyrimidine, triazine and 2-aminopyridine.[2-3] In addition, we recently examined the $[Quinoline(CO_2)]^-$ anionic complex using both photoelectron spectroscopy and density functional theory calculations and were able to determine carbon dioxide's binding energy to be 0.6 eV.[4] This interaction strength is typical of a Lewis acid-base pair (adduct).

Transition metals and CO_2 have also been found to interact strongly when negatively charged. Through infrared photodissociation studies, Weber and co-workers have surveyed a variety of $M(CO_2)_n^-$ clusters. Their work with $Ag(CO_2)_n^-$ and $Au(CO_2)_n^-$ cluster anions[5-6] determined that they have strongly bound core ions of the form $M(CO_2)^-$ whereas their work with $Co(CO_2)_n^-$ and $Ni(CO_2)_n^-$ cluster anions found that they have tightly bound core ions of the form $M(CO_2)_2^-$.[7-8]

Carbon dioxide capture by metal organic frameworks (MOF's) has attracted particular interest due to the extremely high surface areas and tunable properties of MOF's.[9] Carbon dioxide adsorbs primarily onto open metal sites in MOF's. Since we know that an excess electron can induce strong binding between CO_2 and some transition metal atoms as well as between CO_2 and N-heterocyclic molecules, and we have previously characterized the $[Co(Pyridine)]^-$ dimeric anion[10], we therefore have chosen to study the cluster anion, $[Co(Pyridine)(CO_2)]^-$ as a primitive model for CO_2 binding to negatively charged sites in a MOF. In $[Pyridine(CO_2)]^-$, the CO_2 binds to the nitrogen atom's lone pair, while in $[Co(Pyridine)]^-$ the cobalt is positioned above the pyridine ring. The issue is where and how strongly CO_2 interacts in the $[Co(Pyridine)(CO_2)]^-$ anionic complex. These model interactions are the focus of this paper, where we used a

combination of anion photoelectron spectroscopy and density functional theory calculations to study them.

III.2.3 Experimental and Computational Methods

Anion photoelectron spectroscopy is conducted by crossing a beam of mass-selected negative ions with a fixed-frequency photon beam and energy-analyzing the resultant photodetached electrons. The photodetachment process is governed by the energy-conserving relationship $h\nu = EBE + EKE$, where $h\nu$ is the photon energy, EBE is the electron binding energy, and EKE is the electron kinetic energy. The apparatus consists of an laser vaporization ion source, a time-of-flight mass analyzer, a Nd:YAG photodetachment laser, and a magnetic bottle photoelectron spectrometer. The instrumental resolution of the photoelectron spectrometer is ~35 meV at a 1 eV EKE. The third (355 nm) harmonic of a Nd:YAG laser was used to photodetach the mass selected anions. Photoelectron spectra were calibrated against the well-known atomic transitions of Cu^-.

The laser vaporization ion source used for this work consists of a rotating and translating cobalt rod and a pulsed valve (pressurized with 4 bars of helium and 10% CO_2 seeded with pyridine vapor). To generate the clusters of interest, the cobalt rod is ablated with the second harmonic of a Nd:YAG laser while the pulsed valve expands the pyridine and CO_2 helium mixture over the vaporized cobalt. This mixture of cobalt atoms, CO_2, and pyridine reacts and cools in the expanding helium jet before passing through a skimmer and into the time-of-flight mass spectrometer.

Density functional theory calculations were performed with the Gaussian 09 software package.[11] All calculations were carried out with the B3LYP functional[12-13] and 6-31++G(2d,2p) basis set.[14] The B3LYP functional was found satisfactory for Weber and co-workers $[Co(CO_2)_n]^-$ study[7]. For the [Co(Pyridine)(CO_2)] anion, ten different starting anionic geometries with various placements of cobalt, CO_2, and pyridine, were optimized in different spin states. These anions were optimized without symmetry constraints and using default convergence parameters. Many geometries converged to a few similar geometries. Frequency analysis was performed to confirm the identification of a stationary point and provide zero-point energies. Vertical detachment energies were determined from the energetic difference between a given geometrically relaxed anion and a corresponding neutral species with the geometry of the relaxed anion. Natural Population Analysis was used to determine the partial charge of the cobalt, CO_2, and pyridine moieties within the larger anionic complex. Dissociation energies were determined by subtracting the total energy of the bound complex from the sum of the energies of the selected dissociated products.

III.2.4 Results

The anion photoelectron spectra of $[Pyridine(CO_2)]^-$, $[Co(Pyridine)]^-$, $Co(CO_2)^-$, $[Co(Pyridine)(CO_2)]^-$ and are shown stacked in Figure III.2.1. The $[Co(Pyridine)]^-$ and $[Pyridine(CO_2)]^-$ anions have been studied previously and are displayed for comparison. The photoelectron spectrum of $[Co(CO_2)]^-$ is characterized by a single broad and vibrationally unresolved transition that begins at 1.6 eV EBE and continues at higher

EBE until the end of the recorded spectrum. A 2.2 eV maximum is assigned as the vertical detachment energy (VDE) of the $[Co(CO_2)]^-$ complex.

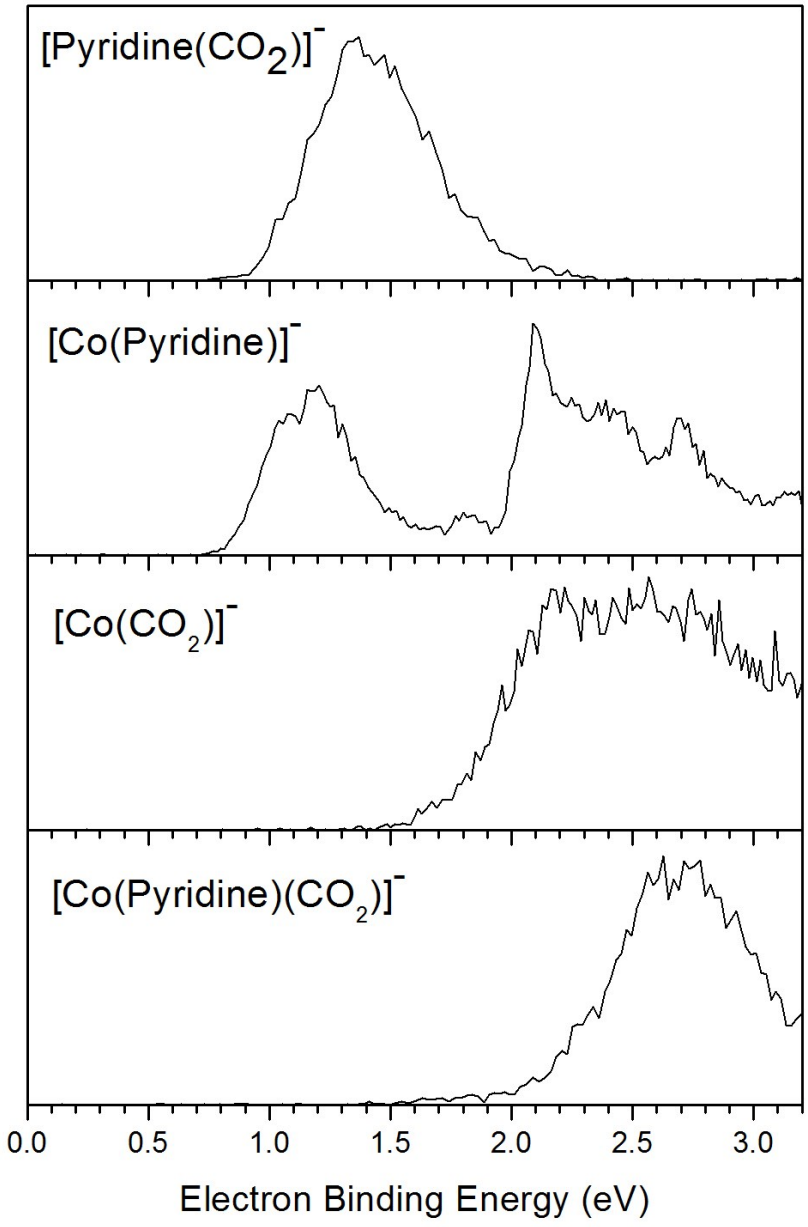

Figure III.2.1: Anion photoelectron spectra of $[Pyridine(CO_2)]^-$, $[Co(Pyridine)]^-$, $[Co(CO_2)]^-$ and $[Co(Pyridine)(CO_2)]^-$.

The photoelectron spectrum of $[Co(Pyridine)(CO_2)]^-$ consists of a single broad and vibrationally unresolved transition that begins at 2.0 eV EBE and displays a relatively large vertical detachment energy (VDE) of 2.7 eV. The 2.7 eV VDE of the $[Co(Pyridine)(CO_2)]^-$ anion contrasts sharply with the VDEs of the $[Co(Pyridine)]^-$ and $[Pyridine(CO_2)]^-$ anionic complexes at 1.2 eV and 1.4 eV, respectively. Ion-molecule solvation strength (i.e. physisorption) is roughly 0.2 eV and typically increases the VDE of an anion by the same amount. The large VDE shift (1.5 eV) from the $[Co(Pyridine)]^-$ anion to the $[Co(Pyridine)(CO_2)]^-$ anion indicates that CO_2 is not simply solvating the $[Co(Pyridine)]^-$ anion and the CO_2 moiety is better described as chemisorbed to the $[Co(Pyridine)]^-$ anion. This analysis can also be extended to rule out a cobalt atom "solvating" a $[Pyridine(CO_2)]^-$ anion and while the VDE shift between $[Co(CO_2)]^-$ and $[Co(Pyridine)(CO_2)]^-$ is smaller at 0.5 eV, a stronger interaction than solvation must still be present.

Three candidate anionic geometries for $[Co(Pyridine)(CO_2)]^-$ were identified computationally. These structures are labeled A, B, and C in Figure III.2.2. These three lowest geometries all have a central cobalt atom with CO_2 and pyridine arranged as ligands. The A configuration has the lowest total energy, while B and C are 0.09 eV and 0.20 eV higher in energy, respectively. VDEs are also indicated with 2.05 eV for A, 1.79 eV for B, and 2.74 eV for C. As the photoelectron spectrum of $[Co(Pyridine)(CO_2)]^-$ has an energy threshold at 2.0 eV, it would appear unlikely that A or B, with a VDEs of 2.05 eV and 1.79 eV, respectively, are dominant geometries. However, the C geometry with its calculated VDE of 2.74 eV has excellent agreement with our experimental VDE of 2.7 eV and thus this geometry would appear to be the dominant species present.

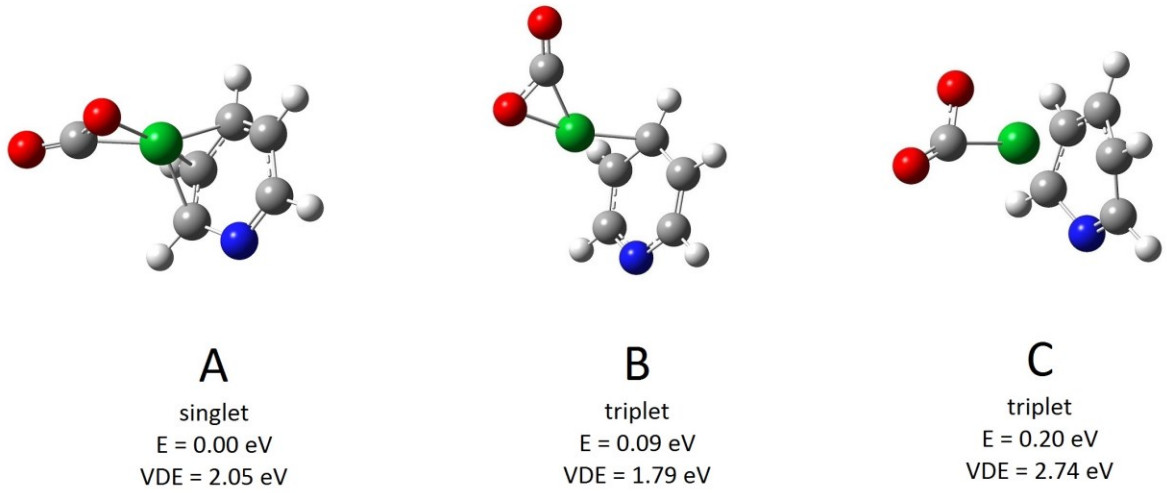

Figure III.2.2: Optimized anionic geometries of $[Co(Pyridine)(CO_2)]^-$. Relative energies, VDEs, and spins are indicated. Carbon atoms are shown in grey, oxygen in red, cobalt in green, hydrogen in white, and nitrogen in blue.

The identified C geometry of the $[Co(Pyridine)(CO_2)]$ anion was further investigated via natural population analysis which suggests ionic character bonding. Partial charges were found to be +0.38e on the Co atom with Pyridine and CO_2 having -0.62e and -0.76e, respectively. This charge distribution is similar to that found by Weber and co-workers for the $Co(CO_2)_2^-$ anion where the central cobalt atom is positively charged and both CO_2 moieties are negatively charged.

Dissociation energies of the C complex were examined through three dissociation channels. These include the $[Co(Pyridine)(CO_2)]^-$ complex dissociating into Pyridine + $CoCO_2^-$, Co + $PyridineCO_2^-$, or CO_2 + $CoPyridine^-$. Calculated values are listed in Table III.2.1. Of the three examined dissociation channels, dissociation into pyridine + $CoCO_2^-$ has the smallest energy barrier at 0.81 eV. Dissociation of $[Co(Pyridine)(CO_2)]^-$ into CO_2

+ CoPyridine$^-$ was found to have a very high energy barrier of 1.42 eV and dissociation of [Co(Pyridine)(CO_2)]$^-$ into Co + PyridineCO_2^- was found to be 1.65 eV. Since VDE shifts should roughly track interaction strength, a comparison can be made between calculated dissociation energies and relevant observed VDE shifts. For instance, the smallest calculated dissociation barrier of 0.81 eV (for dissociation into Pyridine + $CoCO_2^-$) is roughly consistent with the smallest observed VDE shift of 0.5 eV from $CoCO_2^-$ to [Co(Pyridine)(CO_2)]$^-$. While, the largest observed VDE shift of 1.5 eV from CoPyridine$^-$ to [Co(Pyridine)(CO_2)]$^-$ is consistent with the calculated dissociation barrier for dissociation into CO_2 + CoPyridine$^-$ of 1.42 eV. Finally, the calculated dissociation barrier of 1.65 eV for [Co(Pyridine)(CO_2)]$^-$ dissociating into Co + PyridineCO_2^- is roughly consistent with the observed VDE shift of 1.3 eV from PyridineCO_2^- to [Co(Pyridine)(CO_2)]$^-$.

Table III.2.1: Calculated dissociation energies.

Dissociation Pathway	D_o (eV)
[Co(Pyridine)(CO_2)]$^-$ → Pyridine + $CoCO_2^-$	0.81
[Co(Pyridine)(CO_2)]$^-$ → Co + PyridineCO_2^-	1.65
[Co(Pyridine)(CO_2)]$^-$ → CO_2 + CoPyridine$^-$	1.42

Through photoelectron measurements and DFT calculations, the [Co(Pyridine)(CO_2)]$^-$ anionic complex has been shown to be a strongly interacting species. The CO_2 moiety in particular is shown to be bound tightly to the anionic complex with calculations indicating a dissociation barrier of 1.42 eV.

Acknowledgements

This research was supported by the U.S. Department of Energy, Office of Basic Energy Sciences, Division of Chemical Sciences, Geosciences and Biosciences under Award DE-FG02-12ER16362. This material is based on work supported in part by the National Science Foundation under grant number CHE-1360692.

References

1. S. Y. Han, I. Chu, J. H. Kim, J. K. Song, and S. K. Kim, J. Chem. Phys. **113**, 596 (2000).

2. S. H. Lee, N. Kim, D. G. Ha, and S. K. Kim, J. Am. Chem. Soc. **130**, 16241 (2008).

3. N. Kim, Bull. Korean Chem. Soc. **34**, 2247 (2013).

4. J. D. Graham, A. Buytendyk, Y. Wang, S. K. Kim, K. H. Bowen, J. Chem. Phys. **142**, 234307 (2015).

5. B. J. Knurr, J. M. Weber, J. Phys. Chem. A, **117**, 10764–10771 (2013).

6. B. J. Knurr, J. M. Weber, J. Am. Chem. Soc. **134,** 18804-18808 (2012).

7. B. J. Knurr and J. M. Weber, J. Phys. Chem. A **118**, 4056-4062 (2014).

8. B. J. Knurr, J. M. Weber, J. Phys. Chem. A, **118** 8753-8757 (2014).

9. K. Sumida, D. L. Rogow, J. A. Mason, T. M. McDonald, E. D. Bloch, Z. R. Herm, T. H. Bae, J. R. Long, Chem. Rev. **122** 724-781 (2012).

10. B. D. Edmonds, A. K. Kandalam, S. N. Khanna, X. Li, A. Grubisic, I. Khanna, and K. H. Bowen, J. Chem. Phys. **124**, 074316 (2006).

11. Gaussian 09, Revision A.2, M. J. Frisch, G. W. Trucks, H. B. Schlegel, G. E. Scuseria, M. A. Robb, J. R. Cheeseman, G. Scalmani, V. Barone, B. Mennucci, G. A. Petersson, H. Nakatsuji, M. Caricato, X. Li, H. P. Hratchian, A. F. Izmaylov, J. Bloino, G. Zheng, J. L. Sonnenberg, M. Hada, M. Ehara, K. Toyota, R. Fukuda, J. Hasegawa, M. Ishida, T. Nakajima, Y. Honda, O. Kitao, H. Nakai, T. Vreven, J. A. Montgomery, Jr., J. E. Peralta, F. Ogliaro, M. Bearpark, J. J. Heyd, E. Brothers, K. N. Kudin, V. N. Staroverov, R. Kobayashi, J. Normand, K. Raghavachari, A. Rendell, J. C. Burant, S. S. Iyengar, J. Tomasi, M. Cossi, N. Rega, J. M. Millam, M. Klene, J. E. Knox, J. B. Cross, V. Bakken, C. Adamo, J. Jaramillo, R. Gomperts, R. E. Stratmann, O. Yazyev, A. J. Austin, R. Cammi, C. Pomelli, J. W. Ochterski, R. L. Martin, K. Morokuma, V. G. Zakrzewski, G. A. Voth, P. Salvador, J. J. Dannenberg, S. Dapprich, A. D. Daniels, Ö. Farkas, J. B. Foresman, J. V. Ortiz, J. Cioslowski, and D. J. Fox, Gaussian, Inc., Wallingford CT, 2009.

12. A. D. Becke, J. Chem. Phys. **98**, 5648 (1993).

13. C. Lee, W. Yang, and R. G. Parr, Phys. Rev. B **37**, 785 (1988).

14. R. Krishnan, J. S. Binkley, R. Seeger, and J. A. Pople, J. Chem. Phys. **72**, 650 (1980).

IV. Metal Hydride Anions

Relatively recently, only a few aluminum hydrides were known such as alanes (AlH_3) and alanates (AlH_4^-) despite boron hydrides being relatively well understood. Using the PACIS anion source, Andrej Grubisic and co-workers[1] were able to synthesize and study a whole host of new $Al_nH_m^-$ ($4 \leq n \leq 8$, $0 \leq m \leq 10$) complexes. Here, we have examined the alanates anion, AlH_4^-. While this anion is relatively well known, it has had limited gas phase experimental focus. The anion is particularly stable and its high electron binding energy had previously made it inaccessible to study. The addition of a high photon energy (6.4 eV) ArF excimer laser was necessary to record the anion photoelectron spectrum of the species. Computational results found that the neutral complex is thermodynamically unstable which is consistent with the broad photoelectron spectrum observed. Additionally, we have examined the anion of the magnesium hydride anion and its deuterated form, MgH^- and MgD^-. The photoelectron spectra of these diatomic molecules are compared to the results of high-level *ab-initio* calculations and found to be in excellent agreement.

References

1. A. Grubisic, X. Li, S. T. Stokes, J. Cordes, G. F. Gantefoer, K. H. Bowen, B. Kiran, P. Jena, R. Burgert, and H. Schnockel, J. Am. Chem. Soc. 129, 5969-5975 (2007).

IV.1 The Alanate Anion, AlH_4^-: Photoelectron Spectrum and Computations

J. D. Graham, A. M. Buytendyk, X. Zhang, E. L. Collins, and K. H. Bowen

Department of Chemistry, Johns Hopkins University, Baltimore, Maryland 21218, USA

B. Kiran

Department of Chemistry, McNeese State University. Lake Charles, LA 70609, USA

G. Gantefoer

Department of Physics, Konstanz University, 78457 Konstanz, Germany

B. W. Eichhorn,

Department of Chemistry, University of Maryland, College Park, MD, 20742 USA

G. L. Gutsev

Department of Physics, Florida A&M University, Tallahassee, FL, 32307, USA

S. Behera and P. Jena

Department of Physics, Virginia Commonwealth University, Richmond, VA 23284, USA

IV.1.1 Abstract

The alanate anion, AlH_4^-, was generated in the gas phase using a pulsed arc cluster ionization source. Its photoelectron spectrum was then measured with 193 nm photons. The spectrum consists of a broad feature, spanning electron binding energies from 3.8 eV to over 5.3 eV. This band reflects the photodetachment transitions between the ground state of the AlH_4^- anion and the ground state of its thermodynamically unstable neutral

counterpart, AlH_4. The vertical detachment energy (VDE) of AlH_4^- was measured to be 4.4 eV. Additionally, VDE values were also computed in a comprehensive theoretical study and compared both with the previously computed value and with our experimentally-determined value.

IV.1.2 Introduction

The AlH_4^- anion is perhaps the best known aluminum hydride in chemistry. The AlH_4^- anion is the anionic moiety in alkali alanate salts, such as $LiAlH_4$ and $NaAlH_4$, these being powerful reducing agents.[1] AlH_4^- is also of interest as a candidate for hydrogen storage, e.g., as in $Mg(AlH_4)_2$, owing to its high hydrogen gravimetric density.

The AlH_4^- anion has been observed and studied in cryogenic matrices[2-5] and has been found to be relatively unreactive during gas phase thermochemical measurements.[6] Calculations by Boldyrev and co-workers[7,8] showed that the high stability of this anion arises from its excess electron occupying a bonding molecular orbital spread over each of its Al-H bonds. They also found the vertical detachment energy (VDE) of this anion to be 4.83 eV, and that AlH_4^- is stable against dissociation into $AlH_2^- + H_2$ and into $AlH_3 + H^-$ by 3.0 eV and 3.3 eV, respectively. Additionally, other computations have found neutral AlH_4 to be unstable, dissociating along a barrier-free potential surface into AlH_2 and H_2.[9]

Although we had previously observed the AlH_4^- anion along with other aluminum hydride anionic species in mass spectra[10], here we report the measurement of its anion photoelectron spectrum for the first time. Additionally, we have expanded on previous theoretical work by calculating the vertical detachment energy of the AlH_4^- anion at various higher levels of theory. We also computed the energetic differences between

AlH_4^- and its decomposition products, AlH_2^- and H_2 and between the unbound neutral AlH_4 and its decay products, AlH_2 and H_2.

IV.1.3 Experimental Methods

AlH_4^- ions were generated in the gas phase using a pulsed arc cluster ionization source (PACIS). A detailed description of the PACIS can be found elsewhere[11], but a brief overview is given here. During operation, a pulsed valve backed by 200 psi of UHP hydrogen is opened for about 200 microseconds and fills a region between a copper anode and grounded aluminum cathode. A 30 microsecond long, 100 V pulse is applied to the copper anode that discharges through the hydrogen gas and subsequently vaporizes the aluminum cathode. The combination of free atomic hydrogen and vaporized aluminum is entrained with the remaining molecular hydrogen and carried along a 20 cm flow tube where it reacts, cools, and forms AlH_4^- along with other aluminum hydrides. AlH_4^- is then extracted and mass-selected before photodetachment.

Anion photoelectron spectroscopy is conducted by crossing a beam of mass-selected negative ions with a fixed-frequency photon beam and energy-analyzing the resultant photodetached electrons. The photodetachment process is governed by the energy-conserving relationship, $h\nu$ = EBE + EKE, where $h\nu$ is the photon energy, EBE is the electron binding energy, and EKE is the electron kinetic energy. Our instrument consists of a PACIS, a time-of-flight mass spectrometer, a magnetic bottle electron energy analyzer, and an excimer laser. The ArF excimer laser detaches photoelectrons with 193 nm (6.42 eV) photons. The magnetic bottle has an energy resolution of better

than 50 meV at EKE = 1 eV and photoelectron spectra are calibrated against well-known transitions of atomic Cu^-.

IV.1.4 Computational Methods

Our calculations of AlH_4, AlH_4^-, AlH_2, AlH_2^- and H_2 have been carried out using a number of different methods which include density functional theory (DFT), hybrid Hartree-Fock-DFT, and post-HF methods combined with basis sets whose quality ranges from triple-ξ to penta-ξ. The methods applied are the BPW91 (DFT),[12,13] B3LYP[14,15] and M06[16] (HFDFT), second-order Moller-Plesset perturbation theory (MP2),[17] coupled-cluster with single and doubles (CCSD) and non-iterative triples CCSD(T),[18] and the outer valence Green's function (OVGF).[19-21] The OVGF computations were performed with the geometry optimized at the B3LYP level of theory. The basis sets used for Al and H atoms are 6-311+*G**, 6-311++*G*(*3df,3pd*)),[22] cc-pVQZ, cc-pV5Z, and aug-cc-pV5Z,[23] as implemented in Gaussian 03[24] and 09[25] codes.

IV.1.5 Experimental Results

The photoelectron spectrum of AlH_4^- is presented in Figure IV.1.1. The spectrum consists of a broad feature, spanning electron binding energies from 3.8 eV to over 5.3 eV. This feature corresponds to transitions between the ground electronic state of the anion and the ground state of the thermodynamically unstable neutral species. The vertical detachment energy (VDE) of AlH_4^- was measured to be 4.4 eV. Since 6.42 eV photons are energetic enough to dissociate AlH_4^- into $AlH_2^- + H_2$ or $AlH_3 + H^-$, it is possible that these products could have also been formed and subsequently

photodetached in the ion-photon interaction region of our spectrometer. Nevertheless, we saw no evidence for either AlH_2^- at EBE = 1.5 eV (its VDE value) or for H^- at EBE = 0.75 eV (its electron affinity value).

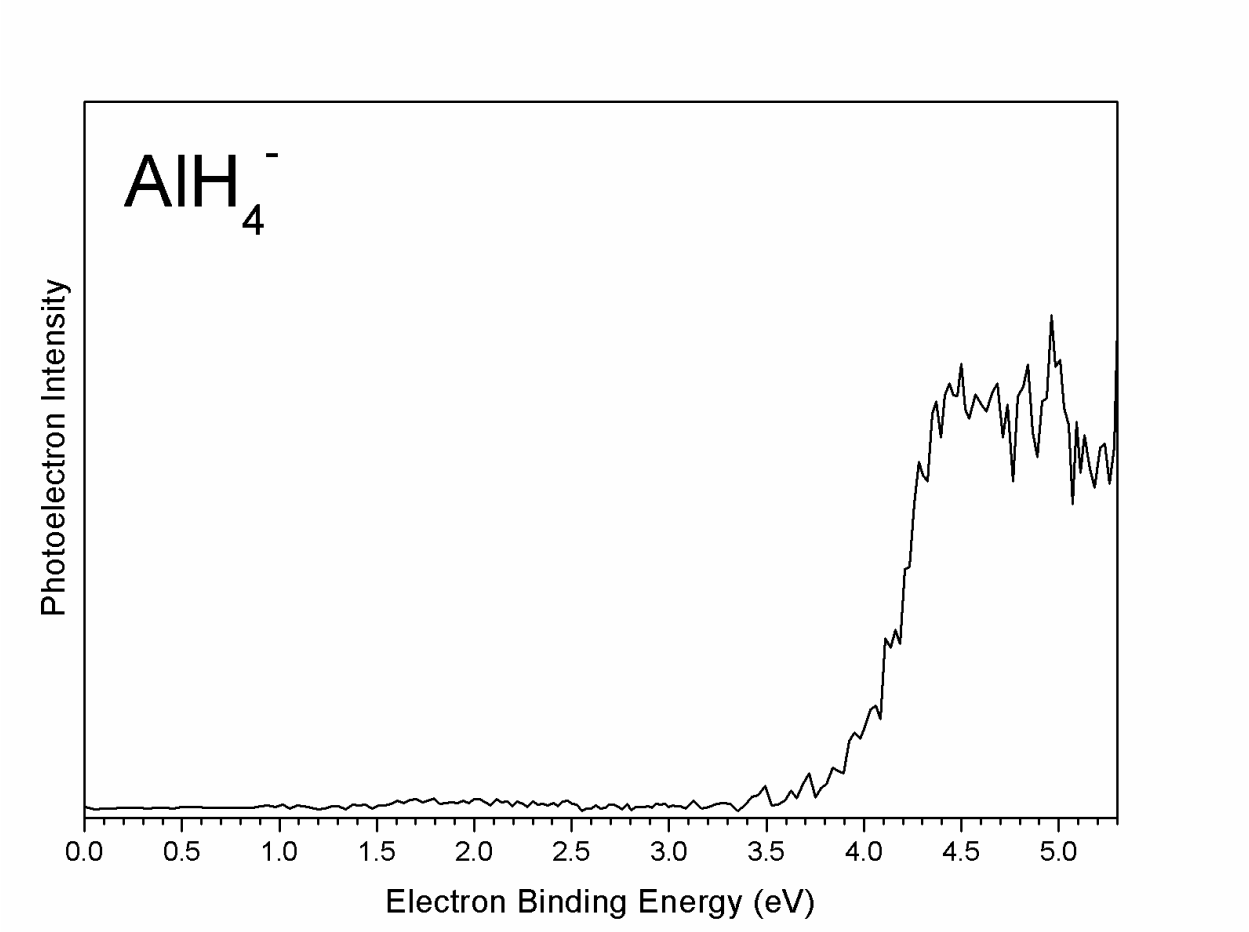

Figure IV.1.1: The photoelectron spectrum of the AlH_4^- anion.

IV.1.6 Computational Results

We began our optimizations without imposing symmetry constraints, followed by re-optimization of the structures obtained within the actual symmetry of their nuclei. All optimizations have been followed by harmonic vibrational frequency calculations in

order to confirm that the structure obtained corresponds to a minimum on the potential energy surface. The convergence threshold in total energy and force was $1x10^{-8}$ eV and $1x10^{-3}$ eV/Å, respectively.

The AlH_4^- anion geometry converged to a geometry of T_d symmetry and its ground state is $^1A_1$. Figure IV.1.2(a) shows the geometrical structure of the AlH_4^- ground state optimized at the B3LYP/6-311++*G*(3*df,3pd*) level, along with the charges on its atoms obtained from the Natural Atomic Orbital (NAO)[26] population analysis. In the AlH_4^- anion, the charge of the central atom is +0.63*e*, which means that the extra electron is delocalized over hydrogen atoms, each carrying a negative charge of –0.41*e*. The AlH_4^- anion satisfies the superhalogen[27,28] formula, MX_{k+1} for monovalent ligands, *X*, where *k* is the maximal formal valence of the central atom, *M*. This is because the maximal formal valence of an aluminum atom with the electronic configuration of [Ne]$3s^2 3p^1$ is three. Formally, the extra electron in AlH_4^- serves as the fourth valence electron of aluminum, which forms single bonds of the 30%(Al) + 70%(H) type with each hydrogen atom in AlH_4^-. The vertical detachment energy (VDE) of the anion is computed at the anion equilibrium geometry according to the following expression,

$VDE(AlH_4^-)$ = E(AlH_4 at its anion's equilibrium geometry) – E(AlH_4^- at equilibrium geometry) (1)

where *E* is the electronic energy. The values obtained from this equation using different methods and basis sets are listed in Table IV.1.1 alongside the value measured from the experimental spectrum.

Table IV.1.1: Energetic difference between AlH_4^- anion and the unbound neutral AlH_4 decay products. AlH_2 and H_2, (E_{asym}), vertical electron detachment energy (VDE) of the AlH_4^- anion, interatomic distances and harmonic vibrational frequency of the H – H vibration (ω_e) in the AlH_4 isomer given in Figure IV.1.2(b), and the differences in total electronic (ΔE) energy and total energy (ΔE_{tot}) for the neutral isomer channels (N ISO) $AlH_4 \rightarrow AlH_2 + H_2$ and (A ISO) $AlH_4^- \rightarrow AlH_2^- + H_2$ computed using different methods and basis sets.

Method	Basis set	E_{asym}, eV	VDE, eV	R(H–H), Å	R(Al–H_2), Å	ω_e(H–H), eV	ΔE, eV
BPW91	6-311++*G*(3*df,3pd*))	2.97	4.14	0.76	2.21	0.50	ΔE(N ISO) = +0.04 ΔE_{tot}(N ISO) = –0.06 ΔE(A ISO) = +0.08 ΔE_{tot}(A ISO) = –0.04
	cc-pVQZ	2.87	4.14	0.77	2.12	0.49	ΔE(N ISO) = +0.08 ΔE_{tot}(N ISO) = –0.04
	cc-pV5Z	2.89	4.13	0.77	2.12	0.49	ΔE(N ISO) = +0.08 ΔE_{tot}(N ISO) = –0.03
B3LYP	6-311+*G**	3.14	4.69	0.75	2.53	0.53	
	6-311++*G*(3*df,3pd*)	3.17	4.69	0.75	2.41	0.52	ΔE(N ISO) = +0.06 ΔE_{tot}(N ISO) = –0.05 ΔE(A ISO) = +0.03 ΔE_{tot}(A ISO) = –0.06
	aug-cc-pV5Z	3.09	4.47	0.75	2.23	0.52	ΔE(N ISO) = +0.07 ΔE_{tot}(N ISO) = –0.04
M06	6-311++*G*(3*df,3pd*)	3.11	4.43	0.75	2.29	0.50	
	aug-cc-pV5Z	3.02	4.40	0.76	2.22	0.51	ΔE(N ISO) = +0.19 ΔE_{tot}(N ISO) = –0.16
MP2	6-311+G*	2.59	4.50	0.74	3.06	0.56	
	6-311++*G*(*3df, 3pd*))	2.84	4.61	0.74	2.48	0.54	
	cc-pVQZ	2.95	4.83	0.75	2.27	0.54	ΔE(N ISO) = +0.09 ΔE_{tot}(N ISO) = –0.02
CCSD	6-311+*G**	2.62	4.39	0.75	3.17	0.51	
	6-311++*G*(3*df,3pd*))	2.91	4.52	0.75	2.51	0.50	

CCSD(T)	6-311+*G**	2.63	4.39	0.75	3.14	0.51	
	6-311++*G*(3*df, 3pd*))	2.94	4.52	0.75	2.46	0.50	ΔE(N ISO) = +0.04 ΔE_{tot}(N ISO) = –0.05 ΔE(A ISO) = +0.04 ΔE_{tot}(A ISO) = –0.12
OVGF	6-311+*G**		4.61				
	6-311++*G*(3*df, 3pd*))		4.74				
Exp.			4.4 [a]			0.547[b]	

[a] This work.

[b] Experimental value of ω_e for the gas-phase H_2 is 0.547 eV (see Ref.[30]) .

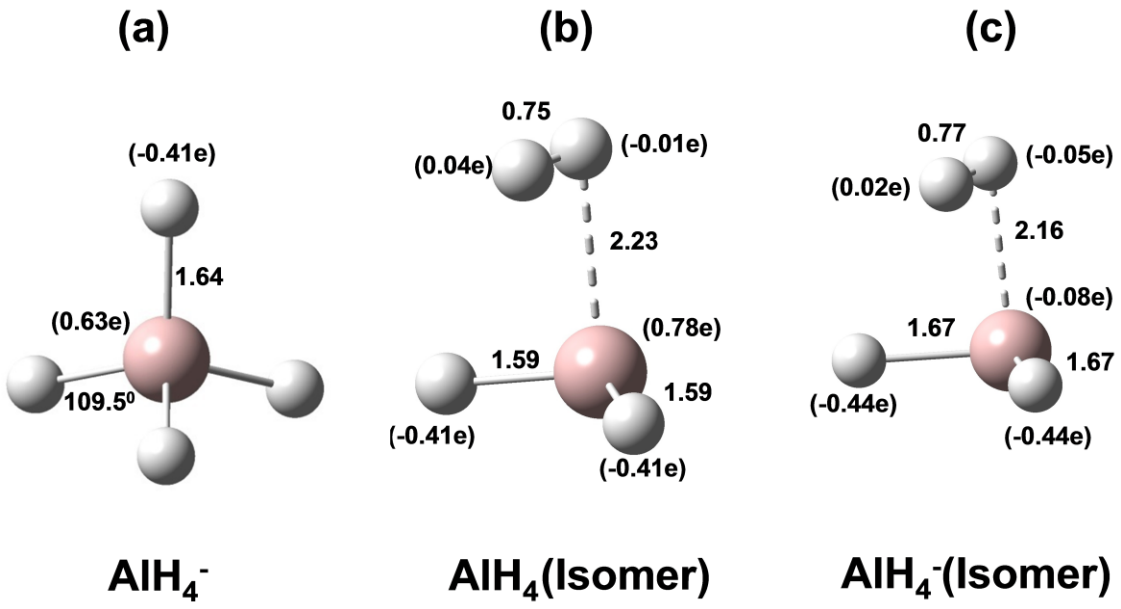

Figure IV.1.2: Geometrical structures of the AlH_4^- ground state (a) and electronically stable states of the neutral (b) and anion (c) isomers as optimized at the B3LYP/6-311++G(3df,3pd) level. Bond lengths are in Å and charges on atoms are in units of electronic charge.

It was found previously[3] and confirmed by the results of our computations that the neutral AlH_4 geometry optimization, beginning with the anion T_d geometry, leads to a transition state of C_{2v} symmetry. We performed an extensive search for a stable state of AlH_4 and found an isomer of the $H_2 \otimes AlH_2$ adduct type of C_s symmetry with all positive harmonic vibrational frequencies. This AlH_4 isomer is stable with respect to the sum of total electronic energies of both AlH_2 and H_2 and AlH_3 and H (see Figure IV.1.3). This neutral isomer is also shown in Figure IV.1.2(b) and as is seen from the charges on atoms, the positive charge on the aluminum atom is nearly balanced by the negative charges in the chemically bound hydrogen atoms. The hydrogen atoms in the quasi-molecularly bound H_2 molecule carry negligible charge and bind weakly to the AlH_2 complex through the charge polarization mechanism.[29] This weak interaction is evident from the differences in total electronic energies, ΔE computed according to equation,

$$\Delta E(\text{N ISO}) = E(AlH_2) + E(H_2) - E(AlH_4 \text{ Isomer}) \quad (2)$$

where N and ISO indicate ΔE is for the neutral AlH_4 isomer. This value is listed in Table IV.1.1 and varies between +0.04 eV and +0.19 eV depending on the method and basis set used.

However, the neutral isomer becomes thermodynamically unstable with respect to the $AlH_4 \rightarrow AlH_2 + H_2$ decay channel when the zero point vibrational energies (ZPVE) are added to the total electronic energies of the AlH_4, AlH_2, and H_2 species. Adding the zero point vibrational energies to the total electronic energies, we compute the differences in total energies for the neutral isomer as:

$$\Delta E_{tot}(\text{N ISO}) = E_{tot}(AlH_2) + E_{tot}(H_2) - E_{tot}(AlH_4 \text{ Isomer}) \quad (3)$$

where E_{tot} is the sum of the total electronic energy of a given species and the corresponding ZPVE. The ΔE_{tot}(N ISO) values computed according to Eq. (3) are negative (see Table IV.1.1) which means that the neutral isomer is thermodynamically unstable.

As there is no stable neutral AlH_4 species, in place of an adiabatic electron affinity, we define E_{asym} as the energetic difference between AlH_4^- and the unbound neutral AlH_4 decay products, AlH_2 and H_2, as

$$E_{asym} = E_{tot}(AlH_2) + E_{tot}(H_2) - E_{tot}(AlH_4^-) \quad (4)$$

The computed E_{asym} values are listed in Table IV.1.1.

Additionally, a stable anion isomer was found and is shown in Figure IV.1.2(c). The anion isomer shows similar behavior to the neutral isomer and is weakly bound at the BPW91, B3LYP and CCSD(T) levels with the 6-311++*G*(3*df,3pd*) basis. In a similar manner as the neutral isomer, the ΔE value for the anion isomer was computed according to the equation,

$$\Delta E(\text{A ISO}) = E(AlH_2^-) + E(H_2) - E(AlH_4^- \text{ Isomer}) \quad (5)$$

where A and ISO indicate ΔE is for the anionic AlH_4^- isomer. Again, as with the neutral isomer, including zero point vibrational energy to the energy of each component yields,

$$\Delta E_{tot}(\text{A ISO}) = E_{tot}(AlH_2^-) + E_{tot}(H_2) - E_{tot}(AlH_4^- \text{ Isomer}) \quad (6)$$

The computed ΔE_{tot}(A ISO) values are negative which indicates that the anion isomer is thermodynamically unstable. The decay channels for the ground-state AlH_4^- anion calculated at the BPW91/6-311++*G*(3*df,3pd*) level are shown in Figure IV.1.3.

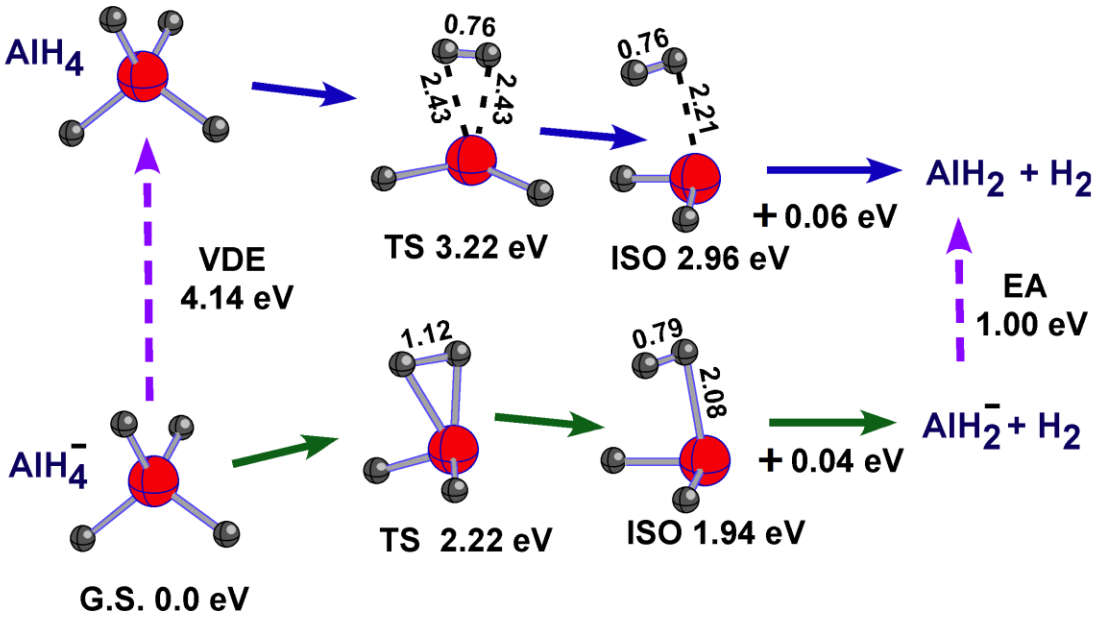

Figure IV.1.3: Decay channels of the AlH_4^- anion (in its ground state) and of the AlH_4 neutral, both computed at the BPW91/6-311++G(3df) level of theory. Ground state is abbreviated G.S., transition state is abbreviated TS and isomer is abbreviated ISO. Bond lengths are in Å.

IV.1.7 Discussion

Using several computational methods belonging to the density functional theory (DFT), hybrid DFT, second-order perturbation theory, and couple-cluster groups, we studied the geometrical and electronic structure of AlH_4 and AlH_4^-. The AlH_4^- anion is

thermodynamically stable by 1.98 eV with respect to the to the $AlH_4^- \rightarrow AlH_2^- + H_2$ decay channel according to our BPW91/6-111++*G*(*3df,3pd*) computations. On the contrary, the neutral AlH_4 is thermodynamically unstable and dissociates to AlH_2 and H_2. The temporary AlH_4 radical presents a case of when a species is electronically stable within the Born-Oppenheimer approximation but is unstable with respect to nuclear motions. The energy of the vertical detachment of an extra electron strongly depends on the method and basis used and is enclosed in the range from 4.13 eV to 4.83 eV according to the results of our computations by different methods. The broad width of the photoelectron spectrum of the AlH_4^- anion is consistent with the instability of neutral AlH_4. Our experimental VDE value of 4.4 eV for the AlH_4^- anion is within the range of our theoretical estimates. The closest to experimental values are obtained at the B3LYP/aug-cc-pV5Z (4.47 eV), M06/aug-cc-pV5Z (4.40 eV), CCSD/6-311+*G** (4.39 eV), and CCSD(T)/6-311+*G** (4.39 eV) levels. The values obtained using the BPW91 method are somewhat underestimated, whereas the OVGF values are somewhat overestimated compared to the experimental value. Since agreement between experiment and theory is quite reasonable, one can conclude that the theoretical results are reliable.

Acknowledgements

This material is based upon work supported by the Air Force Office of Scientific Research (AFOSR) under Grant No. FA9550-11-1-0068 (K.H.B.). Portions of this research were conducted with high performance computational resources provided by the Louisiana Optical Network Initiative.

References

1. Cotton, F. A.; Wilkinson, G. *Advanced Inorganic Chemistry*; Interscience: New York, 1996.

2. Pullumbi, P.; Bouteiller, Y.; Manceron, L. *J. Chem. Phys.* **1994**, 101, 3610-3617.

3. Andrews, L.; Wang, X. *J. Phys. Chem. A*, **2004**, 108, 4202–4210.

4. Wang, X.; Andrews, L.; Tam, S.; DeRose, M.; Fajardo, M. *J. Am. Chem. Soc.*, **2003**, 125, 9218–9228

5. Andrews, L.; Wang, X. *Science*, **2003**, 299, 2049-2052.

6. Goebbert, D.; Hernandez, H.; Francisco, J.; Wenthold, P. *J. Am. Chem. Soc.*, **2005**, 127, 11684–11689

7. Boldyrev A. I.; Simons, J. *J. Chem. Phys.*, **1993**, 99, 4628-4637.

8. Boldyrev, A. I.; von Niessen, W. *Chem. Phys.*, **1991**, 155, 71-78.

9. Wong, S.; Li, W.; Paddon-Row, M. *J. Mol. Struc-Theochem.* **1991**, 226, 285-301.

10. Zhang, X.; Wang, H.; Collins, E.; Lim, A.; Ganteför, G.; Kiran, B.; Schnöckel H.; Eichorn, B.; Bowen, K. *J. Chem. Phys.* **2013**, 138, 124303.

11. Cha, G.; Ganteför G.; Eberhardt, W. *Rev. Sci. Instrum.* **1992**, 63, 5661-5666.

12. Becke, A. D. *Phys. Rev. A* **1988**, 38, 3098-3100.

13. Perdew, J. P.; Wang, Y. *Phys. Rev. B* 1922, 45, 13244-13249.

14. Becke, A. D. *J. Chem. Phys.* **1993**, 97, 5648-5652.

15. Lee, C.; Yang, W.; Parr, R. G. *Phys. Rev. B* **1988**, 37, 785-789.

16. Zhao, Y.; Truhlar, D. G. *J. Phys. Chem. A* **2006**, 110, 13126-13130.

17. Head-Gordon, M.; Pople, J. A.; Frisch, M. J. *Chem. Phys. Lett.* **1998**, 153, 503-506.

18. Bartlett, R. J.; Musial, M. *Rev. Mod. Phys.* **2007**, 79, 291-352.

19. Cederbaum, L. S. *J. Phys. B*, **1975**, 8, 290-303.

20. Ortiz, J. V. *J. Chem. Phys.* **1996**, 104, 7599-7605.

21. Zakrzewski, V. G.; von Niessen, W. *J. Comp. Chem.* **1993**, 14, 13-18.

22. Krishnan, R.; Binkley, J. S.; Seeger, R.; Pople, J. A. *J. Chem. Phys.* **1980**, 72, 650-654.

23. Woon, D. E.; Dunning Jr., T. H. *J. Chem. Phys.* **1993**, 98, 1358-1371; Dunning Jr., T. H. *J. Chem. Phys.* **1989**, 90, 1007-1023.

24. Frisch, M. J.; Trucks, G. W.; Schlegel, H. B.; Scuseria, G. E.; Robb, M. A.; Cheeseman, J. R.; Montgomery, Jr., J. A.; Vreven, T.; Kudin, K. N.; et al. *Gaussian 03*, rev. C.02; Gaussian, Inc.: Wallingford CT, 2004.

25. Frisch, M. J.; Trucks, G. W.; Schlegel, H. B.; Scuseria, G. E.; Robb, M. A.; Cheeseman, J. R.; Scalmani, G.; Barone, V.; Mennucci, B.; Petersson, G. A.; Nakatsuji, et al. *Gaussian 09*, rev. A.2. ed.; Gaussian Inc.: Wallingford, CT, 2009,

26. Reed, A. E.; Curtiss, L. A.; Weinhold, F. *Chem. Rev.* **1988**, 88, 899-926.

27. Gustev, G. L.; Boldyrev, A. I. *Chem. Phys.* **1981**, 56, 277-283.

28. Gustev, G. L.; Boldyrev, A. I. *Adv. Chem. Phys.* **1985**, 61, 169.

29. Niu, J.; Rao, B.; Jena, P. *Phys. Rev. Lett.* **1992**, 68, 2277-2280.

30. Hotop, H.; Lineberger, W. C. *J. Phys. Chem. Ref. Data.* **1985**, 14, 731-750.

IV.2 Photoelectron Spectra of the MgH^- and MgD^- Anions

Allyson Buytendyk, Jacob Graham, Haopeng Wang, Xinxing Zhang, Evan Collins, Y. J. Ko and Kit H. Bowen

Department of Chemistry, Johns Hopkins University, Baltimore, Maryland 21218, USA

Gerd Gantefoer

Department of Physics, University of Konstanz, 78457 Konstanz, Germany

Bryan Eichhorn

Department of Chemistry, University of Maryland, College Park, MD 20742, USA

Anushoba Regmi and Kiran Boggavarapu

Department of Chemistry, McNeese State University, Lake Charles, LA 70609, USA

IV.2.1 Abstract

The molecular anions, MgH^- and MgD^- were generated in a pulsed arc cluster ionization source (PACIS) and studied using anion photoelectron, velocity-map imaging spectroscopy. The electron affinities of MgH and MgD were determined to be 0.90 ± 0.05 eV and 0.89 ± 0.05 eV, respectively. These findings were supported by *ab initio* calculations. Our experimental and theoretical results were compared with those from previous studies.

IV.2.2 Introduction

Magnesium hydride, MgH, has been detected in stellar atmospheres through its optical spectrum,[1,2] and as a light metal hydride, it may also find applications in hydrogen storage and in propulsion.[3] Both MgH and MgD have been extensively studied by experimental[1,2,4-9] and computational[10-14] methods. Their negative ions, however, have received less attention. MgH^- anions were first observed almost fifty years ago in a mass spectrometric study which generated them in a Penning discharge negative ion source.[15] At about the same time, semi-empirical calculations predicted the electron affinities of several gaseous radicals, including MgH.[13] A decade later, again using a Penning discharge source, threshold photodetachment experiments were conducted on MgH^- anions by using the combination of a high pressure xenon lamp and a monochromator as a variable wavelength light source.[16] These experiments provided the first measurement of the electron affinity (EA) of MgH. Around the same time, a cesium beam, sputter ion source was developed to produce MgH^- anions for use in heavy ion, tandem accelerator experiments.[17] Somewhat later, theory provided the bond length and vibrational frequency of the MgH^- anion[18] as well as its magnetizability.[19]

Here, we report the generation of MgH^- and MgD^- anions using a third type of anion source, we present their vibrationally-resolved anion photoelectron spectra, we determine the electron affinities of MgH and MgD, we present calculations which support our findings, and we compare our results with those from previous studies. The present anion photoelectron study of the alkaline earth metal hydride anion, MgH^- joins

previous photoelectron studies of metal hydride anions including alkali metal,[20] transition metal,[21,22] and semi-metal[23,24] diatomic hydride anions.

IV.2.3 Experimental and Computational Methods

Anion photoelectron spectroscopy is conducted by crossing a mass-selected beam of negative ions with a fixed-frequency photon beam and energy-analyzing the resultant photodetached electrons. This technique is governed by the energy-conserving relationship, hν = EBE + EKE, where hν, EBE, and EKE are the photon energy, electron binding (transition) energy, and the electron kinetic energy, respectively.[25] Electron kinetic energy is measured using a velocity-map imaging (VMI)[26,27] spectrometer. There, mass-gated anions are crossed with 532 nm, linearly polarized photons in an electric field, so that resultant photodetached electrons are accelerated along the axis of the ion beam towards a position sensitive detector (75 mm diameter dual microchannel plate detector with a phosphor screen coupled to a CCD camera). The sum of ~50,000 electrons form a 2D image which is then reconstructed into a slice of the 3D distribution via the BASEX[28] method. Photoelectron spectra were calibrated against the well-known photoelectron spectrum of NO^-.

In the present work, MgH^- anions were generated in a pulsed arc cluster ionization source (PACIS), which has been described in detail elsewhere and shown schematically in Figure IV.2.1.[29] Briefly, a ~30 μsec duration, 150 V electrical pulse, applied at 10 Hz across an anode and its sample cathode, vaporized magnesium metal and formed a plasma. Simultaneously, a 200 psi pulse of ultrahigh purity hydrogen gas was delivered into the arc region using a pulsed valve (Parker Series 9). There, many of the H_2

molecules were dissociated into hydrogen atoms and together with magnesium atoms and free electrons were directed down a 20 cm long tube, where they reacted and cooled before exiting into high vacuum. The resulting anions were then extracted into a time-of-flight mass spectrometer, mass-selected using a mass gate, and photodetached with second harmonic photons from a Nd:YAG laser and energy analyzed as described above. MgD^- was generated similarly, but with deuterium gas.

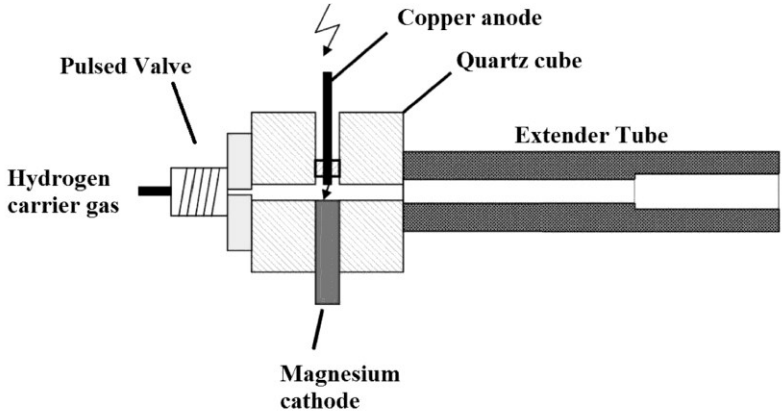

Figure IV.2.1: Schematic diagram of the pulsed arc cluster ionization source (PACIS).

Our calculations were conducted at both the B3LYP/aug-cc-pVQZ and the CCSD(T)/aug-cc-pVQZ levels of theory.[30] Electron affinities were corrected with zero point energies which were calculated at each respective level of theory.[30]

IV.2.4 Results and Discussion

Figure IV.2.2 presents the mass spectrum showing the MgH^- anions. The expected isotopic ratios of magnesium at masses, 24, 25, and 26 amu are reproduced in the intensity pattern of MgH^- anions at masses, 25, 26, and 27. Figure IV.2.3 presents the

anion photoelectron spectra of $^{24}MgH^-$ and $^{24}MgD^-$, both measured using 532 nm (2.33 eV) photons.

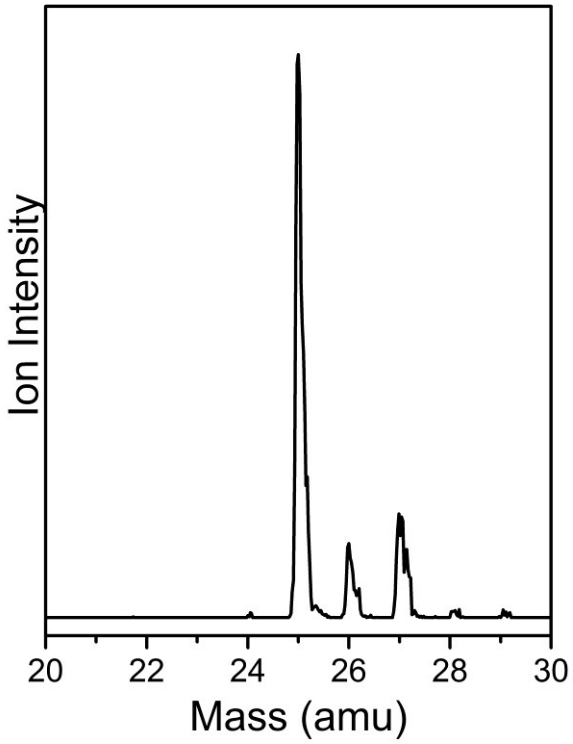

Figure IV.2.2: Mass spectrum showing the three isotopic forms of MgH^- anions.

In the photoelectron spectrum (PES) of MgH^- anion, the observed transitions are centered at EBE = 0.90, 1.08, and 1.24 eV, while in the MgD^- anion spectrum, the transitions are centered at EBE = 0.89 and 1.02 eV. The adiabatic electron affinity, EA, is the energy difference between the lowest energy state of the anion and the lowest energy state of its neutral counterpart. The lowest EBE transition in each spectrum is its origin-containing transition, i.e., the $X\ ^2\Sigma^+$ (v'=0) ← $X\ ^1\Sigma^+$ (v"=0) transition, and it defines the adiabatic electron affinity. Thus, EA(MgH) and EA(MgD) were determined to be 0.90 ± 0.05 eV and 0.89 ± 0.05 eV, respectively. Our electronic structure calculations, at the

B3LYP/aug-cc-pVQZ found the EA for MgH and MgD to be 0.86 eV and 0.85 eV, respectively. Similarly, at the CCSD(T)/aug-cc-pVQZ level of theory, the EA of MgH and MgD were calculated to be 0.86 eV and 0.85 eV, respectively.

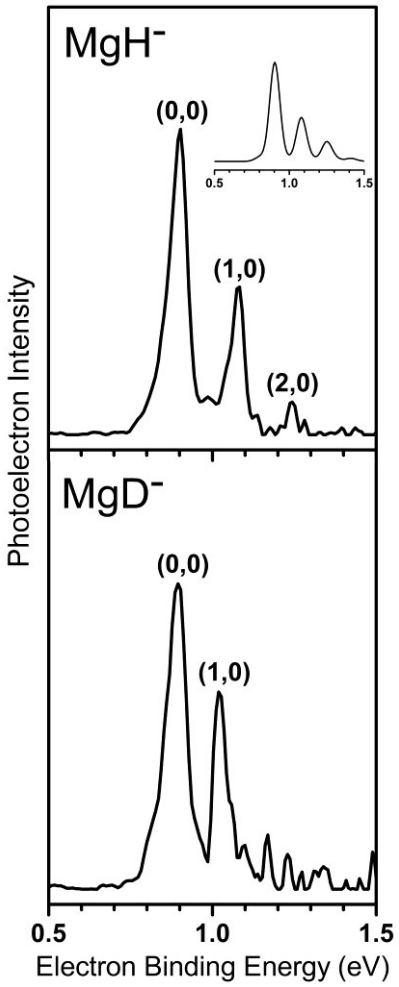

Figure IV.2.3: Photoelectron spectra of MgH^- and MgD^- anions, both measured with 2.33 eV photons. The Franck-Condon fit for MgH^- is shown as an inset above the MgH^- spectrum.

The peak separations in the photoelectron spectra of the MgH^- and MgD^- anions agree relatively well with the known vibrational frequencies of MgH and MgD, respectively.[4,5] The spacing between the two lowest EBE peaks in the spectra of MgH^- and MgD^- are 1452 cm^{-1} and 1049 cm^{-1}, respectively, whereas the vibrational frequencies of MgH and MgD are 1495 cm^{-1} and 1078 cm^{-1}, respectively. Therefore, we assigned the three lowest EBE peaks in the photoelectron spectrum of MgH^- as the (0,0), (1,0), and (2,0) vibrational transitions, respectively. Likewise, we assigned the two lowest EBE peaks in the photoelectron spectrum of MgD^- as the (0,0) and (1,0) vibrational transitions, respectively. Peak locations, adjacent peak splitings, and assignments are presented inTable IV.2.1. We also conducted Franck-Condon analyses using the program, PESCAL2010.[31] The best fit is shown as an inset above the photoelectron spectrum of MgH^- in Figure IV.2.3. While hot bands were not evident in the spectra, an anion temperature of ~ 450 K was implied.

Table IV.2.1: Transition assignments for the photoelectron spectra of MgH- and MgD-

	Peak Location (eV)	**Adjacent Spacing** (cm^{-1})	**Assignment** $X\ ^2\Sigma^+ \leftarrow X\ ^1\Sigma^+$ (v', v")
MgH^-	0.90		(0,0)
		1452	
	1.08		(1,0)
		1290	
	1.24		(2,0)
MgD^-	0.89		(0,0)
		1049	
	1.02		(1,0)

The first measurement of the photodetachment spectrum of MgH^- was conducted by Rackwitz and coworkers[16], who recorded the total photodetachment cross section versus photon energy in discrete steps. In threshold photodetachment spectra, such as this, one observes inflection points rather than line spectra as are seen in fixed-frequency photoelectron spectra. Based on their data, these investigators reported the electron

affinity of MgH to be 1.05 eV, as compared with 0.90 eV in our work. Inspection of their published threshold photodetachment spectrum, however, shows that the first inflection point actually occurs at 0.9 eV. Thus, the two experiments are in good agreement.

The first calculation of the electron affinity of MgH was performed by Gaines and Page, who utilized semi-empirical methods.[13] These investigators found its value to be 1.08 eV. More recently, the EA for MgH was computed at a higher level of theory by Eizaguirre *et al.*[11], who reported a value of 0.83 eV. In the present study, our computations at both the B3LYP/aug-cc-pVQZ and the CCDS(T)/aug-cc-pVQZ level of theory found the EA value of MgH to be 0.86 eV, as compared to our experimentally-determined value of 0.90 ± 0.05 eV.

IV.2.5 Conclusion

We have prepared the diatomic anions, MgH^- and MgD^- in a pulsed arc cluster ionization source and measured their anion photoelectron spectra using velocity-map imaging, electron energy analysis. The electron affinities of MgH and MgD were determined to be 0.90 ± 0.05 eV and 0.89 ± 0.05 eV, respectively. These findings were supported by *ab initio* calculations at the B3LYP/aug-cc-pVQZ and the CCDS(T)/aug-cc-pVQZ level of theory which found the electron affinity of MgH to be 0.86 eV. Both our experimental and theoretical results were in good agreement with those from previous studies.

Acknowledgements

This work was supported by the Air Force Office of Scientific Research through grant numbers, FA9550-11-1-0068 (K.H.B.) and FA9550-11-1-xxxx (B.E.). K.B. acknowledges funding support through a BoR-RCS grant.

References

1. H. D. Babcock, Astrophys. J. **102**, 154 (1945).

2. J. Tomkin and D. L. Lambert, Astrophys. J. **235**, 925 (1980).

3. A. Zaluska, L. Zaluski and J.O. Stroem-Olsen, Appl. Phys. A **72**,157 (2001).

4. W. J. Balfour and H. M. Cartwright, Astron. Astrophys. Supp. Sec., **26**, 389 (1976).

5. W. J. Balfour and H. M. Cartwright, Can. J. Phys. **53**, 1477 (1975).

6. L. B. Knight and William Weltner, J. Chem. Phys. **54**, 3875 (1971).

7. B. Lemoine, C. Demuynck, J. L. Destombes and P. B. Davies, J. Chem. Phys. **89**, 673 (1988).

8. A. Guntsch, Z. Phys. **93**, 534 (1935).

9. W. D. Slafer and D. J. Benard, Appl. Phys. Lett. **32**, 654 (1978).

10. A. C. H. Chan and E. R. Davidson, J. Chem. Phys. **52**, 4108 (1970).

11. A. Eizaguirre, O. Mó, M. Yáñez and J.-C. Guillemin, Chem. Eur. J.**14**, 10423 (2008).

12. P. G. Wenthold, Int. J. Mass Spectrum. **195/196**, 319 (2000).

13. A. F. Gaines and F. M. Page, Trans. Faraday Soc. **62**, 3086 (1966).

14. J.-M. Mestdagh, P. de Pujo, B. Soep and F. Spiegelman, Chem. Phys. Lett. **471**, 22 (2009).

15. K. Bethge, E. Heinicke and H. Baumann, Phys. Lett. **23**, 542 (1966).

16. R. Rackwitz, D. Feldmann, H. J. Kaiser and H. Heinicke, Z. Naturforsh. **32A**, 595 (1977).

17. R. Middleton, Nucl. Instrum. Methods **141**, 373 (1977).

18. R. J. Hinde, J. Phys. Chem. A **104**, 7580 (2000).

19. S. P. A. Sauer, T. Enevoldsen and J. Oddershede, J. Chem. Phys. **98**, 9748 (1993).

20. H. W. Sarkas, J. H. Hendricks, S. T. Arnold, V. L. Slager and K. H. Bowen, J. Chem. Phys., **100**, 1884 (1994).

21. A. E. Stevens, C.S. Feigerle and W.C. Lineberger, J. Chem. Phys. **78**, 5420 (1983).

22. A. E. S. Miller, C.S. Feigerle and W.C. Lineberger, J. Chem. Phys. **87**, 1549 (1987).

23. C. B. Freidhoff, J. T. Snodgrass, J. V. Coe, K. M. McHugh, and K. H. Bowen, J. Chem. Phys., **84**, 1051 (1986).

24. K. M. Ervin and W. C. Lineberger, J. Chem. Phys., **122**, 194303 (2005).

25. J. V. Coe, J. T. Snodgrass, C. B. Freidhoff, K. M. McHugh and K. H. Bowen, J. Chem. Phys. **87**, 4302 (1987).

26. A. T. J. B. Eppink and D. H. Parker, Rev. Sci. Instrum. **68**, 3477 (1997).

27. R. Mabbs, E. Surber and A. Sanov, Analyst **128**, 765 (2003).

28. V. Dribinski, A. Ossadtchi, V. A. Mandelshtam and H. Reisler, Rev. Sci. Instrum. **73**, 2634 (2002).

29. X. Li, A. Grubisic, S. T. Stokes, J. Cordes, G. F. Gantefoer, K. H. Bowen, B. Kiran, M. Willis, P. Jena, R. Burgert, and H. Schnoeckel, Science **315**, 356 (2007).

30. M. J. Frisch, *et al*. Gaussian 09, Revision A.1; Gaussian, Inc. Wallingford, CT, 2009.

31. K.M. Ervin, J. Ho and W.C. Lineberger, J. Phys. Chem. **92**, 5405 (1988).

V. Low Barrier Hydrogen Bonding

The strongest known hydrogen bond is a low barrier hydrogen bond (LBHB) in the HF_2^- complex with a dissociation energy of 2.0 eV. In a LBHB, a proton is shared between anions whose conjugate acids have matching pK_a values and the "low barrier" term refers to the barrier between the potential wells the proton is shared between. Some enzymologists hypothesize that the remarkable rates seen in enzyme catalysis are due in part to the formation of strong, short LBHBs.

We have examined low barrier hydrogen bonding in enzymatically relevant model systems involving carboxylic acids and imidazole. Using shifts in photoelectron spectra we are able to reasonably compare the binding energy of the anions: formate-formic acid, acetate-acetic acid, phenol-phenolate, and imidazolide-imidazole anionic complexes relative to the HF_2^- complex. Even the weakest bound of these, the imidazolide-imidazole anion, was shown to have a binding energy of nearly half that of the HF_2^- complex. Although these are gas-phase experiments, and are in principle the upper limits to what strengths are available inside an enzyme active site, one can postulate that the structured nature of an enzyme active site could maintain some of the gas phase strength of these hydrogen bonds.

V.1 Strong, Low Barrier Hydrogen Bonds may be Available to Enzymes

Jacob D. Graham, Allyson M. Buytendyk, Di Wang, and Kit H. Bowen

Department of Chemistry, Johns Hopkins University, Baltimore, MD 21218, USA

Kim D. Collins

BioMET and Department of Microbiology and Immunology, University of Maryland School of Medicine, Baltimore, MD 21201, USA

V.1.1 Abstract

The debate over the possible role of strong, low barrier hydrogen bonds in stabilizing reaction intermediates at enzyme active sites has taken place in the absence of an awareness of the upper limits to the strengths of low barrier hydrogen bonds involving amino acid side chains. Hydrogen bonds exhibit their maximum strengths in isolation, i.e., in the gas phase. In this work, we measured the ionic hydrogen bond strengths of three enzymatically-relevant model systems in the gas phase using anion photoelectron spectroscopy; we calibrated these against the hydrogen bond strength of HF_2^-, measured using the same technique, and we compared our results with other gas-phase experimental data. The model systems studied here: the formate-formic acid, acetate-acetic acid, and imidazolide-imidazole anionic complexes, all exhibit very strong hydrogen bonds, whose strengths compare favorably with that of the hydrogen bifluoride anion, the strongest known hydrogen bond. The hydrogen bond strengths of these gas-

phase complexes are stronger than those typically estimated as being required to stabilize enzymatic intermediates. If there were to be enzyme active site environments that can facilitate the retention of a significant fraction of the strengths of these isolated (gas-phase), hydrogen bonded couples, then low barrier hydrogen bonding interactions might well play important roles in enzymatic catalysis.

V.1.2 Introduction

Enzymes are remarkably efficient catalysts, notable for bringing about rate enhancements of up to 10^{26} with great specificity under gentle conditions.[1] In the early days of enzymology, it was frequently assumed that there must exist some unknown physio-chemical phenomenon that was making a large contribution to these impressive rate enhancements. Even now, fifty years since modern methods were first brought to bear and with enzymatic catalysis firmly established as a pillar of biochemistry, the basis for the proficiency of enzymes, i.e., their "secret", remains elusive.

The early 1990's saw a flurry of activity that provided clues for elucidating this issue. In 1991, the x-ray structure determination by Petsko and Ringe[2] of a triosephosphate isomerase-transition state analog complex[3] and the simultaneous NMR and infrared work of Knowles[4,5] showed that neutral His-95 is the general acid stabilizing the enediolate intermediate in the reaction catalyzed by triose phosphate isomerase (TIM). In 1993, Gerlt and Gassman[6,7] estimated that TIM His-95 was stabilizing the enediolate intermediate by at least 7 kcal/mol, and they postulated that this occurred because the imidazole side chain of neutral His-95 and the enediolate intermediate had matching pK_a values, facilitating the formation of a short, strong (ionic) hydrogen bond between them.

At about the same time, Cleland and Kreevoy[8] as well as Frey[9] also postulated the formation of strong, low barrier hydrogen bonds (LBHB) between moieties with matching pK_a values to be an integral part of enzyme catalytic mechanisms. Over time, additional circumstantial evidence came to light in support of the LBHB hypothesis.[10,11] Often, LBHB's were recognized in enzyme structures by their short lengths, their small deuterium fractionation factors, and/or their large downfield, proton NMR chemical shifts.[12,13]

While the LBHB hypothesis in enzyme catalysis had its proponents, it also had its critics, and it remains a controversial issue to this day.[14-16] Its opponents note that the existence of ionic hydrogen bonds in enzyme active sites does not in itself imply that they are unusually strong there, and in fact, they doubt that they are. Arguments from both sides are often based on the known or presumed strengths of ionic hydrogen bonds in different environments. Everyone agrees that hydrogen bonds are at their strongest in the gas phase, i.e., *in vacuo*. Moreover, species whose hydrogen bonds are strong in the gas phase often exhibit quite weak hydrogen bonding in aqueous solution, this likely being due to competition with water for hydrogen bonding. Both Guthrie and Perrin cite the weakening of hydrogen bond strengths in water as evidence that proponents' arguments based on strong hydrogen bonds in the gas phase are not relevant to hydrogen bond strengths in enzymes.[14,15] In solids, x-ray crystallography has provided many examples of short, hydrogen bonds in enzyme structures. Nevertheless, these structural findings are unconvincing to some critics; they do not concede that short hydrogen bond lengths in crystalline enzyme structures imply strong hydrogen bonds.[16] They furthermore argue

that hydrogen bonding in crystals is simply not relevant to the environment of the enzyme's active site.

Trending against these criticisms of the LBHB hypothesis are two observations about the cloistered environments of enzyme active sites, on which the viability of short, strong hydrogen bonds there critically depends. First, enzyme active sites typically possess protein loops that fold down over the bound substrate to exclude water.[17] Thus, these sites are largely sequestered from water, making the fact that hydrogen bonds are weakened in aqueous solution beside the point; enzyme sites are not typical aqueous environments. Second, the expectation of strong enzyme-transition state interactions, with the enzyme "bear-hugging" the transition state[18], suggests a relatively compact, semi-rigid environment at the enzyme active site and brings to mind the relatively immobile, structured environments of crystals, where there is evidence for short, possibly strong hydrogen bonds in some enzyme structures. Both of these characteristics are enabled by the macromolecular architecture of enzymes.

An essential tenet of the criticism against the LBHB hypothesis is that the strengths of enzymatically-relevant hydrogen bonds would have to be unexpectedly high in order for it to be plausible. Indeed, under the LBHB hypothesis, hydrogen bond strengths in the range of 10-20 kcal/mol have been proposed as being necessary to account for the stabilization of enzymatic intermediates.[8,19] How might nature achieve such high hydrogen bond strengths at enzyme active sites? Hydrogen bonded couples have the freedom to form their optimal geometric structures and thus their maximal strengths in the gas phase, i.e., *in vacuo,* primarily because there they do not have competing hydrogen bonding interactions. In condensed phase environments, where

potentially competing hydrogen bonding interactions among molecules are plentiful and the optimal structures of hydrogen bonded couples are correspondingly compromised, the average hydrogen bond strength is substantially weaker than in its gas phase counterpart. Environments that suppress competition for forming hydrogen bonds might be expected to allow hydrogen bonded couples to retain a portion of their *in vacuo*, hydrogen bond strengths. The nearly water-free, quasi-rigid structures of enzyme active sites are potentially opportune environments. Thus, it is plausible that some enzyme active sites may provide favorable environments in which hydrogen bond strengths retain a substantial fraction of their gas phase strengths.

Since hydrogen bonds are at their strongest in the gas phase, the strength of a given hydrogen bond there provides an upper limit to its maximum strength in any other environment. In effect, the strength of a hydrogen bonded couple in the gas phase tells us what would be possible in an optimized environment. Thus, measurements of hydrogen bond strengths in the gas phase supply upper limits to their strengths, providing important boundaries. Setting a quantitative benchmark for how strong hydrogen bonds can be at their strongest is the hydrogen bifluoride anion, HF_2^-, in the gas phase. This hydrogen bonded pair, i.e., $F^- \cdots HF$, can also be described as $F^- \cdots H^+ \cdots F^-$, thus its synonym, the proton-coupled bifluoride anion. With a $F^- \cdots HF$ bond strength of 45.8 ± 1.6 kcal/mol (1.99 eV) in the gas phase[20], it is the strongest known hydrogen bond. Even a modest fraction of its *gas phase* strength would be easily enough to supply the needed transition state stabilizations discussed above. Interestingly, the $F^- \cdots HF$ hydrogen bond strength in aqueous solution is only ~0.8 kcal/mol.[21]

Proton-coupled bi-carboxylates top the list as the earliest and still the best-studied systems suspected of forming LBHB's in the vicinity of the active sites of enzymes.[22-24] These hydrogen bonded couples can be depicted as:

Structure 1. 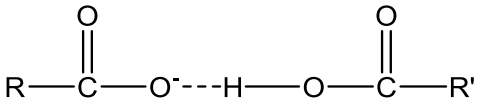

and they can be abbreviated by the general formulae, $X^{-} \cdots HX$. Proton-coupled bi-carboxylates appear in 16% of all protein x-ray structures.[25] There are at least five x-ray structures showing short (and therefore strong) hydrogen bonds between an enzyme carboxylate and a reaction intermediate or transition state analog bound at the enzyme active site; four of these hydrogen bonds are 2.2 or 2.3 Å long whereas one is 2.5 Å long.[26,27] We consider these structures to be the best *de facto* evidence for the existence of low barrier hydrogen bonds stabilizing high energy reaction intermediates at enzyme active sites. Proton-coupled bi-carboxylates are believed to be important components of the active sites of the aspartic acid proteases, e.g., HIV-1 protease.[27] Carboxylates figure prominently in the LBHB enzymatic story in part because *all* negative charges on proteins are carboxylates.

Another system that is implicated in the formation of LBHB's in the vicinity of the active sites of enzymes is imidazole. In the early days of the LBHB story, the seminal work of Knowles had shown that the neutral imidazole side chain of His-95, acting as the general acid, stabilized the enediolate intermediate (E^{-}) in the reaction catalyzed by triose phosphate isomerase.[4,5] This hydrogen bonded couple can be depicted as:

Structure 2. 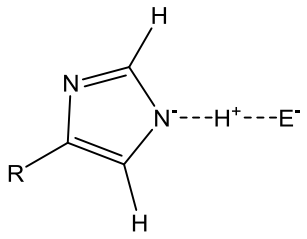

What made imidazole's role as an acid so astonishing was the fact that the pK_a of imidazole (in water) is 14. This apparent dilemma provided among the first clues that LBHB's might be playing important roles in enzyme catalysis.

Given the importance of carboxylates and imidazole in the LBHB story, it is important to know the strengths of their hydrogen bonded couples in the gas phase (*in vacuo*) in order to establish their maximal possible values. Unfortunately, the debate over the possible role of strong, low barrier hydrogen bonds in stabilizing reaction intermediates at enzyme active sites has taken place in the absence of an awareness of the upper limits to the strengths of low barrier hydrogen bonds involving amino acid side chains. To help fill this gap, we have utilized anion photoelectron spectroscopy to measure the hydrogen bond strengths of the formate-formic acid, acetate-acetic acid, and imidazolide-imidazole, anion-neutral, inter-molecular, hydrogen bonded complexes (couples) *in vacuo*. To make a uniform comparison, we also measured the hydrogen bond strength of HF_2^-, i.e., the F^--HF anion-neutral interaction energy using this same experimental technique. Proton coupled identical pairs have been used because bases with the same pK_a's form the strongest low barrier hydrogen bond, and the purpose of this work is to establish an upper limit for the strength of low barrier hydrogen bonds involving amino acid side chains.

V.1.3 Experimental Procedures

Anion photoelectron spectroscopy is conducted by crossing a mass-selected beam of negative ions with a fixed-frequency photon beam and energy-analyzing the resultant photodetached electrons. Photodetachment transitions occur between the ground state of a mass-selected negative ion and the ground and energetically-accessible excited states of its neutral counterpart. This process is governed by the energy-conserving relationship, $h\nu = EBE + EKE$, where $h\nu$ is the photon energy, EBE is the electron binding energy, and EKE is the electron kinetic energy. Measuring electron kinetic energies and knowing the photon energy, provides electron binding (photodetachment transition) energies. Since these are vertical transitions, their relative intensities are determined by the extent of Franck-Condon overlap between the anion and its corresponding neutral. Our apparatus consists of a laser vaporization anion source, a linear time-of-flight mass spectrometer for mass analysis and mass selection, a momentum decelerator, a magnetic bottle electron energy analyzer, and an ArF excimer laser. The magnetic bottle has a resolution of ~50 meV at EKE = 1 eV. In these experiments, photoelectron spectra were recorded with 193 nm (6.42 eV) photons. The photoelectron spectra were calibrated against the well-known transitions of atomic Cu^-. A detailed description of the apparatus has been reported elsewhere.[28]

To produce the fluoride, hydrogen bifluoride; formate, formate-formic acid; and acetate, acetate-acetic acid anions, a small amount of sample (5-pentafluorobenzene, formic acid, or acetic acid, respectively) was entrained in helium (~60 psi) and expanded through the nozzle orifice (0.79 mm diameter) of a pulsed (10 Hz) valve (General Valve Series 9) in a high vacuum chamber (10^{-6} Torr). To produce the imidazolide and

imidazolide-imidazole anions, imidazole was placed in a small oven (~30°C) attached to the front of the pulse valve, where helium (~60 psi) was expanded over the sample in a vacuum chamber. Just outside the orifice of the pulse valve, or in the case of imidazole, just outside the orifice of the oven, low energy electrons were produced by laser/photoemission from a pulsed Nd:YAG laser beam (10Hz, 532 nm) striking a translating, rotating, copper rod (6.35 mm diameter). Negatively-charged anions were then pulse-extracted into the spectrometer prior to mass selection and photodetachment.

V.1.4 Results

In the systems studied here, the $X^- \cdots HX$ anionic complexes are bound, while the corresponding $X \cdots HX$ neutral complexes produced as a result of photodetachment are likely to be unbound. Figure V.1.1 illustrates this situation schematically, where EA(X) is the adiabatic electron affinity of X, E_{asym} is the energy from the ground state of the $X^- \cdots HX$ anionic complex, i.e., HX_2^-, to the $X + HX + e^-$ energy asymptote, and $D(X^- \cdots HX)$ is the dissociation energy of $X^- \cdots HX$ separating into $X^- + HX$, i.e., the hydrogen bond strength of the X^- / HX couple. Thus, $D(X^- \cdots HX) = E_{asym} - EA(X)$.

In anion photoelectron studies of six hydrogen bihalide anions, HX_2^-, where here X denotes both homogeneous and heterogeneous combinations of the halogen atoms, Cl, Br, and I, Neumark found the $X \cdots HX$ neutral complexes, resulting from photodetachment of HX_2^-, to be unbound.[29,30] Importantly, inspection of his photoelectron spectra shows that E_{asym} values, which in these particular cases are known from tabulated EA(X) and $D(X^- \cdots HX)$ values, usually lie only ~0.2 eV above the EBE value of the photoelectron intensity onset, E_{OS}, in the corresponding HX_2^- photoelectron spectra. (The low intensity "tail" between E_{asym} and E_{OS} was likely due to

photodetachment of vibrationally excited HX_2^- anions, i.e., hot bands.) Furthermore, if one defines a photoelectron intensity threshold, E_T, by extrapolating a straight line to the baseline from high on the low EBE side of the lowest EBE band in each spectrum, then the difference between E_{asym} and E_T becomes even smaller than that between E_{asym} and E_{OS}. Thus, the photoelectron spectra of hydrogen bihalide anions, which are in many ways analogous to the systems under study in the present work, support the approximation that $E_{asym} \cong E_T$. With this, we obtain the working relationship, $D(X^- \cdots HX) \cong E_T(HX_2^-) - EA(X)$.

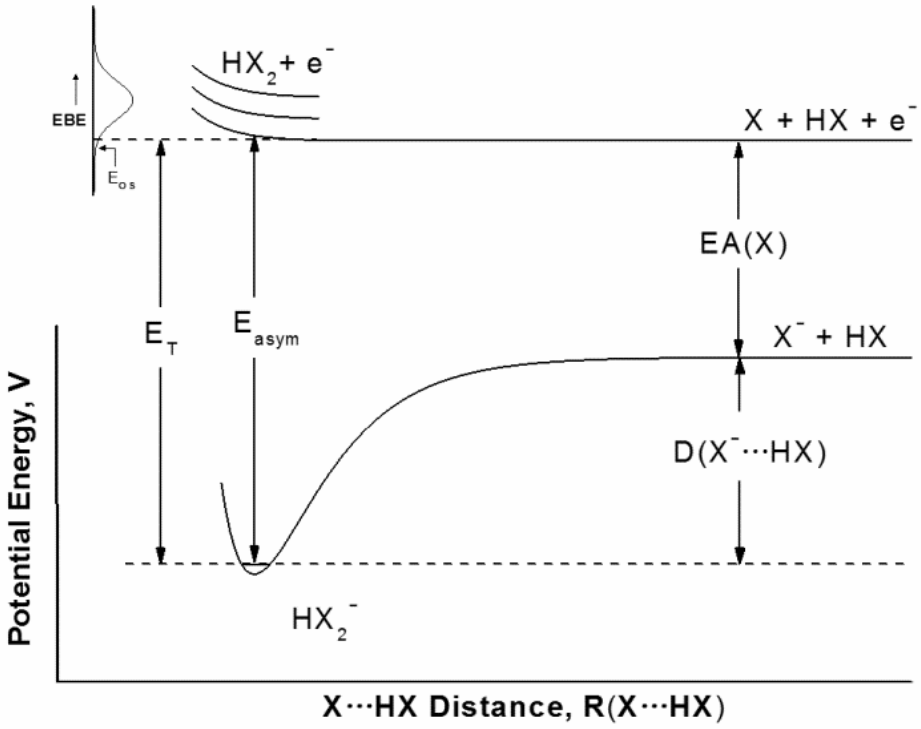

Figure V.1.1: Schematic representation of the energetics of anion photoelectron (photodetachment) spectroscopy as applied to HX_2^-. Symbols are defined in the text.

In the present work, we measured the photoelectron spectra of X^- and of $X^- \cdots HX$ for each of the LBHB candidate systems of interest. Upon determining EA(X) and

$E_T(HX_2^-)$ values, their differences provided values of $D(X^- \cdots HX)$, these being the sought-after hydrogen bond strengths of specific X^-/HX couples. In determining EA(X) values from photoelectron spectra of X^- anions, we benefited from previous photodetachment and photoelectron studies of the fluorine atomic anion[31], the formate anion[32], the acetate anion[33], and the imidazolide anion[34]. These studies assigned the origin transitions in their respective X^- photoelectron spectra, thereby providing accurate EA(X) values. While our photoelectron spectra of these same X^- anions were recorded at lower resolution, they are fully consistent with those previously recorded, allowing us to locate the EBE value of their origin transitions on the spectral profiles observed in this study. Values of $E_T(HX_2^-)$ were determined as described above by extrapolation along the low EBE side of the lowest EBE spectral band in our HX_2^- photoelectron spectra.

Figure V.1.2 presents the photoelectron spectra of corresponding sets of X^- and HX_2^- species measured in this work. In each panel, the spectrum of X^- is positioned above that of HX_2^-, but on the same energy scale, facilitating a pictorial depiction of $D(X^- \cdots HX)$ as the energy difference between specific points (see vertical tick-marks) on the two photoelectron spectra, these points designating the values of EA(X) and $E_T(HX_2^-)$, respectively. For this reason, the length of the horizontal arrow in each panel is a measure of the hydrogen bond strength, $D(X^- \cdots HX)$, of its corresponding HX_2^- species, i.e., of the X^-/HX couple. Referencing the hydrogen bond strengths of the three enzymatic model systems studied here to that of HF_2^-, by using the same experimental method for all four, puts all these measurements on a common footing and provides confidence in comparing the results. Thus, Figure V.1.2 (a-d) successively present the photoelectron spectra of the fluorine anion, F^- and the fluoride-hydrogen fluoride, hydrogen bonded complex, $F^-(HF)$,

i.e., HF_2^-; the photoelectron spectra of the formate anion, Fo^- and the formate-formic acid, hydrogen bonded complex, $Fo^-(HFo)$; the photoelectron spectra of the acetate anion, Ac^- and the acetate-acetic acid, hydrogen bonded complex, $Ac^-(HAc)$; and the photoelectron spectra of the imidazolide anion, Im^- and the imidazolide-imidazole, hydrogen bonded complex, $Im^-(HIm)$. Table V.1.1 presents values of EA(X), $E_T(HX_2^-)$, and $D(X^- \cdots HX)$ for each of the four systems that we studied here, where $D(X^- \cdots HX)$ is the measured hydrogen bond strength for that particular X^-/HX couple.

Table V.1.1: Values leading to Hydrogen Bond Strengths of X^-/HX couples, i.e., $D(X^- \cdots HX)$. All uncertainties are ± 0.1 eV or less.

$X^- \cdots HX$ System	EA(X) Literature	$E_T(HX_2^-)$ This Work	$D(X^- \cdots HX)$ This Work		% of F-HF HB Strength
	eV	eV	eV	kcal/mol	%
$F^- \cdots HF$	3.40[a]	5.4	2.0	46	100%
$Fo^- \cdots HFo$	3.50[b]	4.9	1.4	32	70%
$Ac^- \cdots HAc$	3.25[c]	4.8	1.6	37	80%
$Im^- \cdots HIm$	2.61[d]	3.5	0.9	21	45%

[a]Ref 31, [b]Ref 32, [c]Ref 33, [d]Ref 34

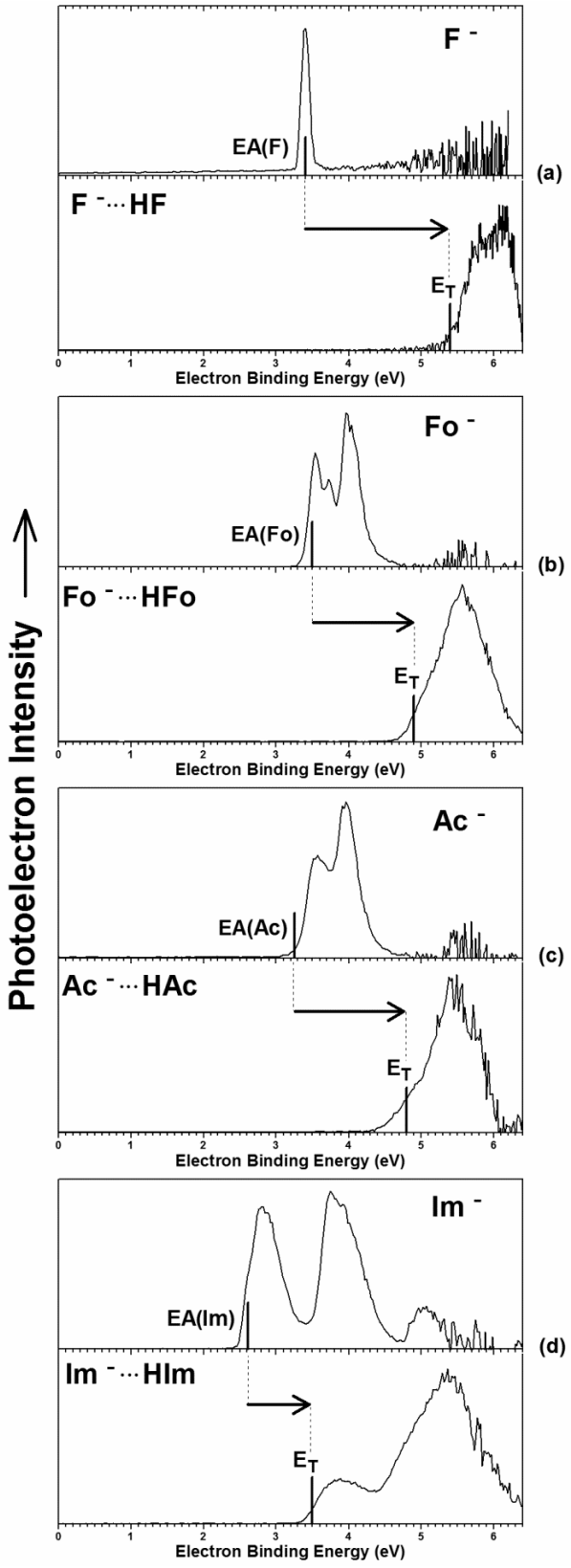
F -
EA(F)
(a)
F -···HF
E_T
Fo -
EA(Fo)
(b)
Fo -···HFo
E_T
Ac -
EA(Ac)
(c)
Ac -···HAc
E_T
Im -
EA(Im)
(d)
Im -···HIm
E_T
Photoelectron Intensity
Electron Binding Energy (eV)
0
1
2
3
4
5
6

Figure V.1.2: Anion photoelectron spectra of the four corresponding sets of X^- and HX_2^- species measured in this work. All spectra were calibrated against the well-known photoelectron spectrum of Cu^-, the anion of the copper atom.

V.1.5 Discussion

Although the combatants in the debate over enzyme active site low barrier were unaware of the work, the dissociation energies of the HX_2^- systems studied here had also been determined in the gas phase by Wenthold and Squires, using energy-resolved, collision-induced dissociation (CID)[20] and by Meot-Ner (Mautner), using high pressure mass spectrometry and van't Hoff plots.[35,36] The CID measurement of the hydrogen bond strength of HF_2^- gave 1.99 eV (45.8 kcal/mol), whereas the HF_2^- hydrogen bond strength measured in our work was 2.0 eV (46 kcal/mol). The thermodynamic/van't Hoff plot determinations of the hydrogen bond strengths of Fo^-(HFo), Ac^-(HAc), and Im^-(HIm) were 1.60 eV (36.8 kcal/mol), 1.27 eV (29.3 kcal/mol), and 1.14 eV (26.4 kcal/mol), respectively, whereas the hydrogen bond strengths of the corresponding species measured in our spectroscopic work were 1.4 eV (32 kcal/mol), 1.6 eV (37 kcal/mol), and 0.9 eV (21 kcal/mol), respectively. What is important about these complementary measurements is that their values, while measured using different techniques, are comparable. They support one another by yielding the same approximate values for corresponding hydrogen bond strengths.

The core result of both the present and previous work is that all three of the enzymatically-relevant model systems considered here exhibit upper limit (gas phase), hydrogen bond strengths that are very strong. According to our measurements, the

hydrogen bond strengths of the formate-formic acid, acetate-acetic acid, and imidazolide-imidazole complexes are respectively 70%, 80%, and 45% of the strength of the fluoride-hydrogen fluoride complex, HF_2^-, with values from previous measurements giving similar percentages. Thus, the carboxylate and imidazolide, inter-molecular hydrogen bonded X^-/HX couples queried here in the gas phase do indeed have hydrogen bond strengths that are comparable to that of the F^-/HF hydrogen bonded couple. Furthermore, it is also interesting to note that in a gas phase, photoelectron study by Wang[37], the shift between *trans*- versus *cis*- $HO_2CCH{=}CHCO_2^-$ (the fumaric/maleic acid mono-anion) spectra revealed the *intra*-molecular hydrogen bond strength in the *cis*-isomer (hydrogen maleate) to be 21.5 kcal/mol, which is 47% of the hydrogen bond strength of HF_2^-.

The threshold hydrogen bond strengths needed to account for the stabilization of enzymatic intermediates have been variously estimated to lie between 7 kcal/mol[6,7] (in the case of imidazole) and 20 kcal/mol.[8,19] The gas-phase, hydrogen bond strengths that we measured for the Fo^-(HFo), Ac^-(HAc), and Im^-(HIm) complexes are 32 kcal/mol, 37 kcal/mol, and 21 kcal/mol, respectively. The lower threshold value of 7 kcal/mol is 22%, 19%, and 33% of the measured hydrogen bond strengths of these complexes, respectively, whereas the higher threshold value of 20 kcal/mol is 63%, 54%, and 105% of these same strengths, respectively. If there were to exist enzyme active site environments that allowed hydrogen bonded couples to retain significant percentages of their gas phase (isolated) strengths, and if these exceeded the pertinent threshold values, then ionic hydrogen bonding might well figure prominently in facilitating enzymatic rate enhancements.

By definition, an environment in which a hydrogen bonded couple has no

opportunity to form alternative hydrogen bonds would preserve its strength, *viz.*, *in vacuo* (gas phase). In solution (liquids), however, where there may be many competing hydrogen bonding interactions, the strength per hydrogen bonded couple would be lowered. One can also envision a quasi-solid state regime of limited molecular mobility, lying between these extremes. There, both the opportunities for forming alternative hydrogen bonds (the degree of competition for forming them) and the corresponding strengths of their hydrogen bonds would be intermediate between those of gases and liquids. The envisioned relationship between hydrogen bond strength and the extent of competition in regard to these three environments is illustrated schematically in Figure 3.

Thus, it is plausible that some enzyme active site environments may correspond to this intermediate case, giving them the possibility of maintaining exceptionally strong hydrogen bonds. Even so, such strong hydrogen bonds would be only part of the story, since other factors, such as local geometry and protein strain, are also expected to play important roles. This work does not prove the validity of the LBHB hypothesis. However, through gas phase (*in vacuo*) measurements, it does provide upper limits to the possible strengths of several enzymatically-relevant hydrogen bond couples. It also suggests a framework for describing how some enzyme active sites might preserve a substantial portion of that strength for their use in catalysis.

References

1. Edwards, D. R., Lohman, D. C. and Wolfenden, R. (2012) Catalytic proficiency: the extreme case of S-O cleaving sulfatases, *J. Am. Chem. Soc. 134*, 525-531.

2. Davenport, R. C., Bash, P. A., Seaton, B. A., Karplus, M., Petsko, G. A., and Ringe, D. (1991) Structure of the triosephosphate isomerase phosphoglycolohydroxamate complex: an analog of the intermediate on the reaction pathway, *Biochemistry 30*, 5821-5826.

3. Collins, K. D. (1974) An activated intermediate analogue: the use of phosphoglycolohydroxamate as a stable analogue of a transiently occurring dihydroxyacetone phosphate-delivered enolate in enzymatic catalysis, *J. Biol. Chem*. 249, 136-142.

4. Lodi, P. J. and Knowles, J. R. (1991) Neutral imidazole is the electrophile in the reaction catalyzed by triosephosphate isomerase: structural origins and catalytic implications, *Biochemistry* 30, 6948-6956.

5. Komives, E. A., Chang, L. C., Lolis, E., Tilton, R. F., Petsko, G. A., and Knowles, J. R. (1991) Electrophilic catalysis in triosephosphate isomerase: the role of histidine-95, B*iochemistry 30*, 3011-3019.

6. Gerlt, J.A. and Gassman, P. G. (1993) An explanation for rapid enzyme-catalyzed proton abstraction from carbon acids: importance of late transition states in concerted mechanisms, *J. Am. Chem. Soc. 115*, 11552-11568.

7. Gerlt, J. A. and Gassman, P. G. (1993) Understanding the rates of certain enzyme-catalyzed reactions: Proton abstraction from carbon acids, acyl transfer reactions, and displacement reactions of phosphodiesters, *Biochemistry 32*, 11943-11952.

8. Cleland, W. W. and Kreevoy, M. M. (1994) Low-barrier hydrogen bonds and enzymic

catalysis, *Science 264*, 1887-1890.

9. Frey, P. A., Whitt, S. A. and Tobin, J. B. (1994) A low-barrier hydrogen bond in the catalytic triad of serine proteases. *Science 264*, 1927-1930.

10. Frey, P. A. (2001) Strong hydrogen bonding in molecules and enzymatic complexes, *Magn. Reson. Chem*. *39*, S190-S198.

11. Cleland, W. W. (2010) The low-barrier hydrogen bond in enzymic catalysis, *Adv. Phys. Org. Chem*. *44*, 1-17.

12. Cleland, W.W. (2000) Low-barrier hydrogen bonds and enzymatic catalysis. *Arch. Biochem. Biophys.* 382, 1-5.

13. Mildvan, A. S., Massiah, M. A., Harris, T. K., Marks, G. T., Harrison, D. H. T., Viragh, C., Reddy, P. M., and Kovach, I. M. (2002) Short, strong hydrogen bonds on enzymes: NMR and mechanistic studies, *J. Mol. Struct. 615*, 163-175.

14. Perrin, C. L. (2010) Are short, low-barrier hydrogen bonds unusually strong?, *Acc. Chem. Res. 43*, 1550-1557.

15. Guthrie, J.P. (1996) Short strong hydrogen bonds: can they explain enzymic catalysis? *Chem. Biol. 3*, 163-170.

16. Perrin, C. L. and Nielson, J. B. (1997) "Strong" hydrogen bonds in chemistry and biology. *Annu. Rev. Phys. Chem. 48*, 511-544.

17. Malabanan, M. M., Amyes, T. L., and Richard, J. P. (2010) A role for flexible loops in enzyme catalysis, *Curr. Opin. Struct. Biol. 20*, 702-710.

18. Snider, M. G., Temple, B. S., and Wolfenden, R. (2004)The path to the transition state in enzyme reactions: a survey of catalytic efficiencies, *J. Phys. Org. Chem. 17*, 586-591.

19. Snider, M. J., Gaunitz, S., Ridgway, C., Short, S. A., and Wolfenden, R. (2000)

Temperature effects on the catalytic efficiency, rate enhancement, and transition state affinity of cytidine deaminase, and the thermodynamic consequences for catalysis of removing a substrate "anchor", *Biochemistry 39*, 9746-9753.

20. Wenthold, P. G. and Squires, R. R. (1995) Bond dissociation energies of F_2^- and HF_2^-. a gas-phase experimental and G2 theoretical study, *J. Phys. Chem. 99*, 2002-2005.

21. Kresge, A. J. and Chiang, Y. (1973) Solvent isotope effects on the ionization of hydrofluoric acid, *J. Phys. Chem. 77*, 822-825.

22. Pan, Y. P. and McAllister, M. A. (1997) Characterization of low-barrier hydrogen bonds. 1. microsolvation effects. an ab initio and DFT investigation, *J. Am. Chem. Soc. 119*, 7561-7566.

23. Mariam, Y. H. and Musin, R. N. (2008) Transition from moderate to strong hydrogen bonds: its identification and physical bases in the case of O−H···O intramolecular hydrogen bonds. *J. Phys. Chem. A 112*, 134-145.

24. Guo, J., Tolstoy, P. M., Koeppe, B, Golubev, N. S., Denisov, G. S., Smirnov, S. N., and Limbach, H.-H. (2012) Hydrogen bond geometries and proton tautomerism of homoconjugated anions of carboxylic acids studied via H/D isotope effects on ^{13}C NMR chemical shifts, *J. Phys. Chem. A 116*, 11180-11188.

25. Langkilde, A., Kristensen, S. M., Leggio, L. L., Mølgaard, A., Jensen, J. H., Houk, A. R., Poulsen, J.-C. N., Kauppinen, S., and Larsen, S. (2008) Short strong hydrogen bonds in proteins: a case study of hamnogalacturonan acetylesterase, *Acta Crystallogr.* D64, 851-863.

26.Collins, K.D. (2012) Why continuum electrostatics theories cannot explain biological structure, polyelectrolytes or ionic strength effects in ion-protein interactions. *Biophys.*

Chem. 167, 43-59.

27. Shen, C.H., Tie, Y., Yu, X., Wang, Y.-F., Kovalevsky, A. Y., Harrison, R. W., and Weber, I. T. (2012) Capturing the reaction pathway in near-atomic-resolution crystal structures of HIV-1 protease, *Biochemistry 51*, 7726-7732. 28. O. C. Thomas, W. J. Zheng, and K. H. Bowen, "Magic numbers in copper-doped aluminum cluster anions", J. Chem. Phys., 114, 5514-5519 (2001).

29. Metz, R. B., Weaver, A., Bradforth, S. E., Kitsopoulos, T. N., and Neumark, D. M. (1990) Probing the transition state with negative ion photodetachment: the chlorine atom + hydrogen chloride and bromine atom + hydrogen bromide reactions, *J. Phys. Chem. 94*, 1377-1388.

30. Bradforth, S. E., Weaver, A., Arnold, D. W., Metz, R. B., and Neumark, D. M. (1990) Examination of the Br + HI, Cl + HI, and F + HI hydrogen abstraction reactions by photoelectron spectroscopy of $BrHI^-$, $ClHI^-$, and FHI^-, *J. Chem. Phys. 92*, 7205-7222.

31. Blondel, C. (1995) Recent experimental achievements with negative ions, *Phys. Scr. 58*, 31-42.

32. Kim, E.H., Bradforth, S. E., Arnold, D. W., Metz, R.B., and Neumark, D. W. (1995) Study of HCO_2 and DCO_2 by negative ion photoelectron spectroscopy, *J. Chem. Phys. 103*, 7801-7814.

33. Wang, X-B., Woo, H-K., Wang, L-S., Minofar, B., and Jungwirth, P. (2006) Determination of the electron affinity of the acetyloxyl radical (CH_3COO) by low-temperature anion photoelectron spectroscopy and ab initio calculations, *J. Phys. Chem. A 110*, 5047-5050.

34. Gianola, A. J., Ichino, T., Hoenigman, R. L., Kato, S., Bierbaum V. M., and

Lineberger, W. C. (2005) Photoelectron spectra and ion chemistry of imidazolide. *J. Phys. Chem. A 109*, 11504-11514.

35. Meot-Ner (Mautner), M. and Sieck, L. W. (1986) The ionic hydrogen bond and ion solvation. 5. OH-*O- bonds. gas-phase solvation and clustering of alkoxide and carboxylate anions, *J. Am. Chem. Soc. 108*, 7525-7529.

36. Meot-Ner (Mautner), M. (1988) Models for strong interactions in proteins and enzymes. 2. interactions of ions with the peptide link and with imidazole, *J. Am. Chem. Soc. 110*, 3075-3080.

37. Woo, H-K., Wang, X-B., Wang, L-S., and Lau, K-C. (2005) Probing the low-barrier hydrogen bond in hydrogen maleate in the gas phase: a photoelectron spectroscopy and ab initio study, *J. Phys. Chem. A 109*, 10633-10637.

V.2 The Hydrogen Bond Strength of the Phenol-Phenolate Anionic Complex: A Computational and Photoelectron Spectroscopic Study

Allyson M. Buytendyk, Jacob D. Graham, and Kit H. Bowen

Department of Chemistry, Johns Hopkins University, Baltimore, MD 21218, USA

Kim D. Collins

IMET and Department of Microbiology and Immunology, University of Maryland School of Medicine, Baltimore, MD 21201, USA

Chia-Hua Wu and Judy I. Wu

Department of Chemistry, University of Houston, Houston, TX 77204, USA

V.2.1 Abstract

The phenol-phenolate anionic complex was studied *in vacuo* by negative ion photoelectron spectroscopy using 193 nm photons and by density functional theory (DFT) computations at the ωB97XD/6-311+G(2d,p) level. We characterize the phenol-phenolate anionic complex as a proton-coupled phenolate pair, i.e., as a low-barrier hydrogen bond system. Since the phenol-phenolate anionic complex was studied in the gas phase, its measured hydrogen bond strength is its maximal ionic hydrogen bond strength. The D($PhO^- \cdots HOPh$) interaction energy (26-30 kcal/mol), i.e., the hydrogen bond strength in the $PhO^- \cdots HOPh$ complex, is quite substantial. Block-localized wavefunction (BLW) computations reveal that hydrogen bonded phenol rings exhibit increased ring π-electron delocalization energies compared to the free phenol monomer.

This additional stabilization may explain the stronger than expected proton donating ability of phenol.

V.2.2 Introduction

Phenol and its chemical derivatives are important building blocks in biological systems. Phenol is the side-chain functional group in the amino acid, tyrosine. Deprotonated phenol, i.e., the phenolate anion, enjoys enhanced stabilization due to the delocalization of its excess charge onto the aromatic ring.[1-5] For this reason, phenol exhibits slightly higher gas-phase acidity than most alcohols.[6-9] While the correlation between electronegativities and hydrogen bond strengths in OH/O- proton-coupled complexes has been studied theoretically,[10-13] there have been no gas-phase experiments involving the phenol-phenolate anions.

The phenol-phenolate anionic complex can also be viewed as a likely example of an ionic, low-barrier hydrogen bond (LBHB). In a LBHB, a proton is shared between anions whose conjugate acids have matching or near matching pK_a values. Some enzymologists postulate that the remarkable rate enhancements seen in enzyme catalysis are due in part to the formation of strong, short LBHBs.[14-18] A ^{1}H NMR study by Mildvan and coworkers[19] provided evidence for the existence of a LBHB between the phenolic proton of the Tyr-14 side chain in the enzyme active site of Δ^5-3-ketosteroid isomerase (KSI) and the dienolate reaction intermediate. The strength of that hydrogen bond was estimated to be at least 7.1 kcal/mol (0.31 eV), whereas typical hydrogen bond strengths in proteins are somewhat smaller. In the gas phase (*in vacuo*), this value might be expected to be significantly larger, because competition among hydrogen bonding partners in condensed phase environments usually reduces hydrogen bond strengths

compared to those in the gas phase, where there is no competition. We view the gas-phase, phenol-phenolate anionic complex as an elementary model for the above enzymatic interaction.

V.2.3 Experimental Methods

Anion photoelectron spectroscopy is conducted by crossing a mass-selected beam of negative ions with a fixed-frequency photon beam and energy-analyzing the resultant photodetached electrons. Photodetachment transitions occur between the ground state of a mass-selected negative ion and the ground and energetically accessible excited states of its neutral counterpart. This process is governed by the energy-conserving relationship hν = EBE + EKE, where hν is the photon energy, EBE is the electron binding energy, and EKE is the electron kinetic energy. Measuring electron kinetic energies and knowing the photon energy provides electron binding (photodetachment transition) energies. Because these are vertical transitions, their relative intensities are determined by the extent of Franck−Condon overlap between the anion and its corresponding neutral. Our apparatus consists of a laser photoemission anion source, a linear time-of-flight mass spectrometer for mass analysis and mass selection, a magnetic bottle electron energy analyzer, and an ArF excimer laser. The magnetic bottle has a resolution of ~50 meV at an EKE of 1 eV. In these experiments, photoelectron spectra were recorded with 193 nm (6.42 eV) photons. The photoelectron spectra were calibrated against the well-known transitions of atomic Cu−. A description of our apparatus has been reported elsewhere.[20]

To produce the phenolate and phenol−phenolate anions, phenol was placed in a small oven (~25 °C) attached to the front of a pulsed (10 Hz) valve (General Valve

Series 9), where helium (~45 psia) was expanded over the sample in a high vacuum chamber (10^{-6} Torr). Just outside the orifice of the oven, low-energy electrons were produced by laser/photoemission from a pulsed Nd:YAG laser beam (10 Hz, 532 nm) striking a translating, rotating, copper rod (6.35 mm diameter). Negatively-charged anions were then pulse-extracted into the spectrometer prior to mass selection and photodetachment.

V.2.4 Computational Methods

Geometry optimizations for the phenol, phenolate, and phenol−phenolate complex (both radical and anionic forms) as well as the electron affinity of phenolate, EA(PhO), the electron affinity of the phenol-phenolate complex, EA((PhO_2)H), the dissociation energy of the neutral phenol-phenolate complex, D(PhO···HOPh), and the dissociation energy of the anionic phenol-phenolate complex dissociating into those two units, $D(PhO^{-}\cdots HOPh)$, values were computed at ωB97XD[21]/6-311+G(2d,p)[22] (all energies reported include zero-point energy corrections). Minima structures were located and vibrational frequency analyses verified the nature of the stationary points. Basis set superposition error (BSSE) corrections to the hydrogen bonding interaction energies were computed using the counterpoise approach.[23] All computations were performed in Gaussian 09.[24]

Block-localized wavefunction (BLW)[25] computations quantified the π-resonance energies (RE) of the free (monomer) and hydrogen bonded phenol, following the Pauling-Wheland resonance energy definition. The BLW-RE's were computed by the total energy of the fully delocalized wavefunction (Ψ_{deloc}) of the phenol ring considred minus that of a localized wavefunction (Ψ_{loc}), in which π-conjugation among the C=C π-

bonds were artificially "turned off" (BLW-RE = $\Psi_{deloc} - \Psi_{loc}$). Ψ_{loc} is computed by partitioning all of the electrons and basis functions of the molecule considered into four subspaces ("blocks"): three for each of the π-C=C units (each block includes two π-electrons, as well as the p_z, d_{xz}, and d_{yz} basis functions for each carbon atom) and one for the remainder of the molecule (including the remaining electrons and basis functions); orbitals of the same subspaces are mutually orthogonal but orbitals of different subspaces overlap freely. Both Ψ_{deloc} and Ψ_{loc} are self-consistently optimized. All vertical BLW-RE computations were performed at B3LYP/6-31G(d)//ωB97XD/6-311+G(2d,p).

V.2.5 Results and Analysis

The photoelectron spectrum of the phenolate anion, PhO^- is presented in Figure V.2.1(a). Three distinct bands are present. The $v' = 0 \leftarrow v'' = 0$ (origin) transition resides under the lowest EBE band. Our photoelectron spectrum of the phenolate anion is in agreement with those reported previously.[1-4] In extracting the electron affinity value from our photoelectron spectrum of the PhO^- anion, we benefited from previous anion photoelectron studies of PhO^-. Lineberger and co-workers[1] determined the EA(PhO) value to be 2.2530 ± 0.0060 eV; Fielding and co-workers[2] reported an EA(PhO) value of 2.15 ± 0.15 eV; Neumark and co-workers[3] assigned an EA(PhO) value of 2.25380 ± 0.00080 eV; and Wang and co-workers[4] determined EA(PhO) value to be 2.25317 ± 0.00037 eV. While our photoelectron spectrum of the PhO^- anion was recorded at lower resolution, it is fully consistent with those previously recorded, allowing us to locate the EBE value of its origin transition on the spectral profile observed in this study. Our computational EA(PhO) value of 2.16 eV is also in good agreement with the previously

reported experimental values, validating our theoretical methods, but also providing a measure of the accuracy of those methods.

The photoelectron spectrum of the phenol−phenolate anionic complex, $PhO^{-}\cdots HOPh$, is presented in Figure V.2.1(b). It exhibits at least two broad features, with the onset of the first transition occurring at 3.0 eV. Although an electron affinity cannot be confidently assigned to the $PhO^{-}\cdots HOPh$ anion spectrum, an empirical threshold value (E_T), based on a linear extrapolation of the steepest rise on the low EBE side of the lowest EBE band in the spectrum, was determined to be 3.16 eV ± 0.15 eV. Our calculated EA($(PhO)_2H$) value was 3.01 eV. This is consistent with our photoelectron spectrum of the $PhO^{-}\cdots HOPh$ anion, and it is close to our estimated threshold value.

In our previous LBHB work[26] we looked to the anion photoelectron studies of six hydrogen bihalide anions, HX_2^-, where X denoted both homogeneous and heterogeneous combinations of the halogen atoms, Cl, Br, and I, as guides for interpreting our photoelectron spectra and for extracting hydrogen bond strengths, i.e., $D(X^- \cdots HX)$, directly from them. The simpler hydrogen bihalide anions are in many ways analogous to more chemically complicated proton-coupled LBHB systems. Neumark and co-workers[27,28] found the X···HX neutral complexes, resulting from photodetachment of HX_2^-, to be unbound. Our computations involving the phenol-phenolate system, however, found the PhO···HOPh neutral complex to be bound by 0.36 eV. Thus, the sought-after hydrogen bond strength of the PhO^-/HOPh couple cannot be estimated solely from the photoelectron spectral data.

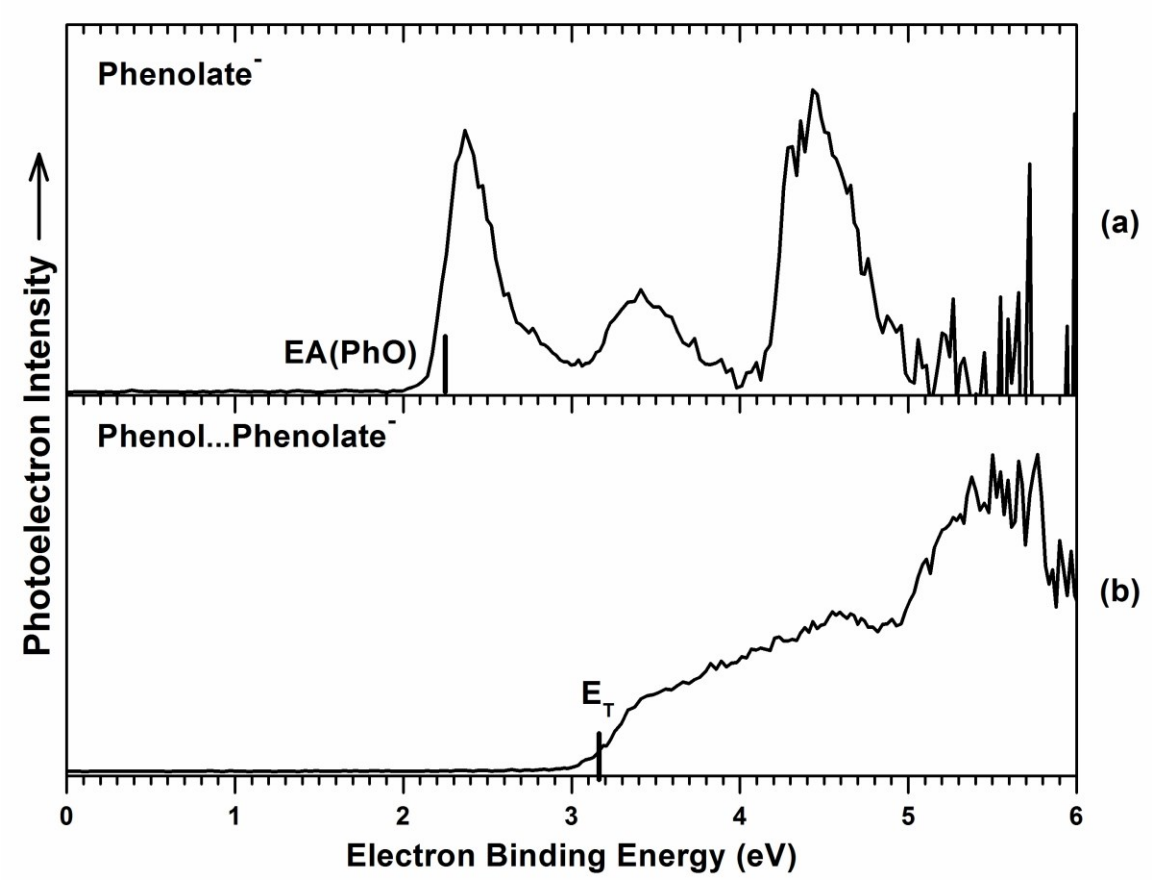

Figure V.2.1: Anion photoelectron spectra of (a) the phenolate anion and (b) the phenol-phenolate anionic complex. All spectra were calibrated against the photoelectron spectrum of Cu–, the copper atomic anion.

The phenol-phenolate anion, hydrogen bond strength, $D(PhO^{-}\cdots HOPh)$, can be determined by inputting the calculated and/or experimental values presented above into the following energetic relationship:

$$D(PhO^{-}\cdots HOPh) = EA\ ((PhO)_2H) + D(PhO\cdots HOPh) - EA(PhO) \qquad (1)$$

Using only calculated values for the quantities on the right side of this equation yields a $D(PhO^{-}\cdots HOPh)$ value of 1.21 eV (27.97 kcal/mol). This value is in excellent agreement with previous calculations performed at the composite CCSD(T) level with complete

basis set (CBS) extrapolation (1.22 eV, 28.1 kcal/mol).[10] Substituting only the experimentally very well-determined EA(PhO) value of 2.25 eV in Eqn. (1) implies a D(PhO$^-$···HOPh) value of 1.12 eV (25.8 kcal/mol). Using the experimentally-determined values of both EA(PhO) and E_T, along with the computationally-derived value for D(PhO···HOPh), implies a D(PhO$^-$···HOPh) value of 1.27 eV (29.3 kcal/mol). All of these ways for finding D(PhO$^-$···HOPh), i.e., the phenol-phenolate anion, ionic hydrogen bond strength, imply that it is quite strong. Pertinent values and relationships are exhibited in Table V.2.1 and in Figure V.2.2.

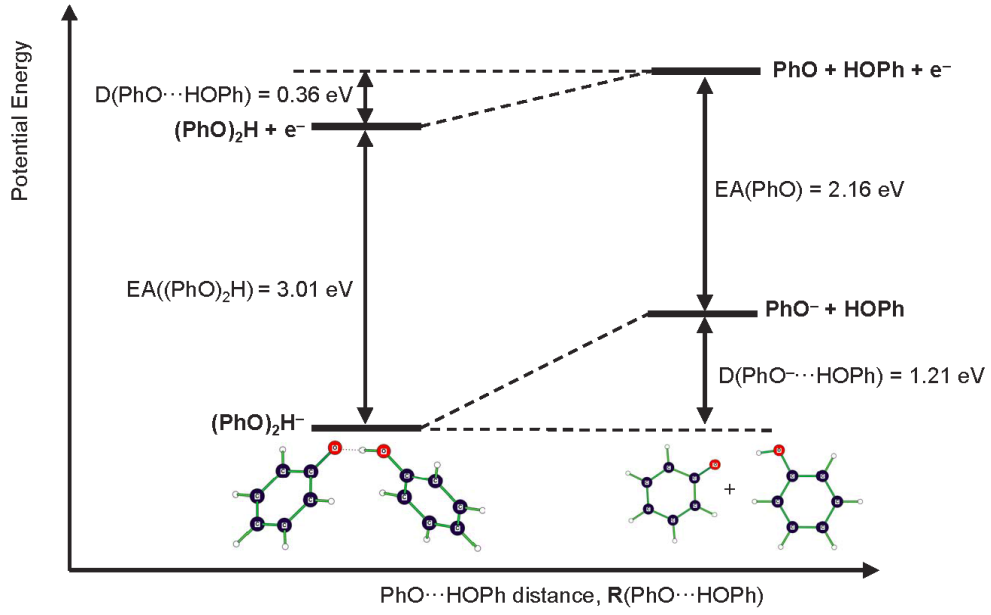

Figure V.2.2: Schematic illustration of the energetic relationships between EA(PhO), EA((PhO)2H), D(PhO···HOPh), and D(PhO–···HOPh) [all values include zero-point vibrational energy (ZPVE) and basis set superposition error (BSSE) corrections].

Table V.2.1: Computed EA(PhO), EA($(PhO)_2H$), and D(PhO···HOPh) values[a] at ωB97XD/6-311+G(2*d*,*p*) [all values include zero-point vibrational energy (ZPVE) and basis set superposition error (BSSE) corrections]. The implied D(PhO^-···HOPh) value provides a direct estimate of the PhO^-···HOPh hydrogen bonding strength. Experimental values are listed in parenthesis for comparison.

EA(PhO)	EA ($(PhO)_2H$)	D(PhO···HOPh)	D(PhO^-···HOPh)
2.16	3.01	0.36	1.21
(*2.25*)[b]	(*E_T = 3.16*)	--	--

V.2.6 Discussion

Since hydrogen bonds are expected to be at their strongest in the gas phase, the estimated phenol-phenolate anion hydrogen bond strength (26-30 kcal/mol) we report here represents the maximum interaction strength of the PhO^-/HOPh couple in other environments. In the enzyme catalyzed reaction by ketosteroid isomerase (KSI), the dienolate intermediate is thought by some to be stabilized by a strong, low-barrier hydrogen bond (LBHB) involving a tyrosine hydroxyl (Tyr14) side chain. The PhO^- /HOPh hydrogen bond, i.e, $PhO^- \cdots H^+ \cdots {}^-OPh$, is a model for this interaction, and the interaction strength seen in this work suggests that it is a low barrier hydrogen bond.

The phenol/phenolate anion's hydrogen bond strength is ~60% of the hydrogen bond strength of HF_2^- (2.0 eV), the strongest known hydrogen bond.[26] This may seem surprising, since phenol is a very weak acid with a ~pK_a value of 10 (in water). What is responsible for its unexpected proton donating ability, and how can phenol form such

strong hydrogen bonds? The answer lies in the increased ring π-resonance of the hydrogen-bonded phenol. In the $PhO^{-}\cdots HOPh$ complex, hydrogen bonds can polarize the π-electrons in the phenol ring, enhance its "phenolate-like" character (see Figure V.2.3, resonance structures on the right), and lead to increased π-electron delocalization. Note that increased π-conjugation does not necessarily reflect enhanced π-aromatic character. Upon hydrogen bonding, phenol exhibits increased net π-electron delocalization energy but reduced π-aromaticity, since the π-electrons are polarized towards the exocyclic C–O moiety (this reduces "cyclic" six π-electron character in the ring, see also resonance forms of the hydrogen bonded phenol in Figure 3, right). The degree of π-resonance (RE) increase can be estimated directly through BLW computations (see Methods). Based on this procedure (see Figure 3, left), the three π-bonds in phenol can be localized into three "blocks" (each corresponding to a localized π-molecular orbital with two π electrons); this disables π-conjugation, and when compared to the energy of the fully π-electron delocalized wavefunction, provides a measure of the RE of phenol. Remarkably, the computed BLW-RE for the hydrogen-bonded phenol (BLW-RE: 117.5 kcal/mol, in $PhO^{-}\cdots HOPh$) is +9.6 kcal/mol greater than that of the free phenol monomer (BLW-RE: 107.9 kcal/mol). This "extra" stabilization is significant and may contribute to the stronger than expected $PhO^{-}\cdots HOPh$ hydrogen bond strength.

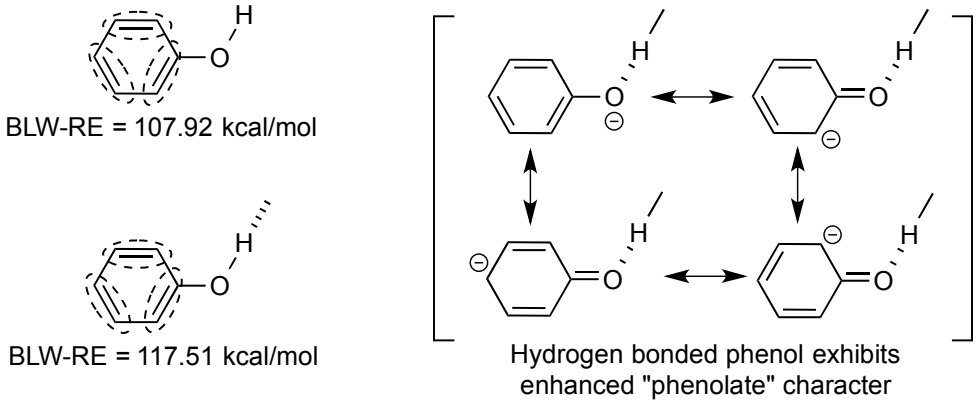

Figure V.2.3: (On the left) Computed vertical BLW-RE's (in kcal/mol, at B3LYP/6-31G*) for the phenol monomer and hydrogen bonded phenol (in PhO–···HOPh). The dotted circles represent the three π-electron localized "blocks"; this BLW procedure disables π-conjugation

The strength of the phenol-phenolate hydrogen bond is close to the previously measured gas-phase, intermolecular hydrogen bond strength of the proton-coupled pair imidazole-imidazolide (0.9 eV).[26] Imidazole is also a very weak acid with a ~pK_a value of 14 (in water). The hydrogen bond strength in the imidazole−imidazolide anionic complex, $Im^{-}\cdots HIm$, was estimated from the difference between the $E_T[H(Im)_2]$ and EA(Im). Given that the hydrogen bonding interaction, D(PhO···HOPh), in the neutral radical, Ph···HPh, was not negligible in the estimation of the PhO^{-}/HOPh hydrogen bond strength, we calculated the hydrogen bonding interaction of neutral Im···HIm and found it to be 0.29 eV. Thus, our previously reported value of 0.9 eV may be a lower limit to the hydrogen bond strength of the Im^{-}/HIm complex. A previous gas phase measurement of the dissociation energy of HIm_2^{-} reported a value of 1.1 eV.[29] Thus, a hydrogen bond strength that is slightly greater than 0.9 eV for the imidazole−imidazolide anionic complex would be reasonable and in good agreement with that measurement. In any case,

the result of both the present work on PhO^-/HOPh and the previous work on Im^-/HIm is that the ionic hydrogen bond strengths of these enzymatically relevant models are very strong in the gas phase. If even a fraction of these hydrogen bond strengths were to be retained in enzyme active site environments, they might be able to facilitate enzymatic rate enhancements.

V.2.7 Conclusions

The hydrogen bonding in the phenol-phenolate anionic complex was studied experimentally using anion photoelectron spectroscopy and theoretically using density functional theory computations at the ωB97XD/6-311+G(2d,p) level. The computed and experimentally-derived phenol-phenolate anion hydrogen bond strengths agree and are rather considerable. The unexpectedly strong bonding in the $PhO^- \cdots$HOPh complex may be due to increased π-electron delocalization stabilization in the phenol ring.

Acknowledgements

This material is based on work supported by the National Science Foundation under Grant Numbers, CHE-1360692 (KHB) and CHE-1057466 (JIW).

References

1. R. F. Gunion, M. K. Gilles, M. L. Polak and W. C. Lineberger, *Int. J. Mass. Spectrom. Ion Processes*, 1992, **117**, 601.

2. A. R. McKay, M. E. Sanz, C. R. S. Mooney, R. S. Minns, E. M. Gill and H. H. Fielding, *Rev. Sci. Instrum.*, 2010, **81**, 123101.

3. J. B. Kim, T. I. Yacovitch, C. Hock and D. M. Neumark, *Phys. Chem. Chem. Phys.*, 2011, **13**, 17378.

4. H.-T. Liu, C.-G. Ning, D.-L. Huang, P. D. Dau and L.-S. Wang, *Angew. Chem. Int. Ed.*, 2013, **52**, 8976.

5. J. D. Steill, A. L. May, S. R. Campagna, J. Oomens and R. N. Compton, *J. Phys. Chem. A*, 2014, **118**, 8597.

6. T. B. McMahon and P. Kebarle, *J. Am. Chem. Soc.*, **1977**, 99, 2222.

7. J. E. Bartmess, J. A. Scott, R. T, McIver, Jr. *J. Am. Chem. Soc.*, 1979, **110**, 6046.

8. D. F. McMillen and D. M. Golden, *Ann. Rev. Phys. Chem.*, 1982, **33**, 493.

9. R. M. Borges dos Santos and J. A. M. Simoes, *J. Phys. Chem. Ref. Data*, 1998, **27**, 707.

10. M. Kolaski, A. Kumar, N. J. Singh and K. W. Kim, *Phys. Chem. Chem. Phys.*, 2011, **13**, 991.

11. T. M. Krygowski and H. Szatylowicz, *J. Phys. Chem. A*, 2006, **110**, 7232.

12. A. K. Chandra and T. Uchimaru, *Int. J. Mol. Sci.*, 2002, **3**, 407.

13. A. Surjoosingh, S. Hammes-Schiffer, *J. Phys. Chem. A,* 2011, **115**, 2367-2377.

14. P. J. Lodi and J. R. Knowles, *Biochemistry*, 1991, **30**, 6948.

15. J. A. Gerlt and P. G. Gassman, *J. Am. Chem. Soc.*, 1993, **115**, 11552.

16. W. W. Cleland and M. M. Kreevoy, *Science*, 1994, **264**, 1887.

17. P. A. Frey, S. A. Whitt and J. B. Tobin, *Science*, 1994 **264**, 1927.

18. W. Childs and S. G. Boxer, *Biochemistry*, 2010, **49**, 2723.

19. Q. Zhao, C. Abeygunawardana, P. Talalay, and A. S. Mildvan, *Proc. Natl. Acad. Sci.*, 1996, **93**, 8220.

20. O. C. Thomas, W. J. Zheng, and K. H. Bowen, *J. Chem. Phys.*, 2001, **114**, 5514.

21. J.-D. Chai and M. Head-Gordon, *Phys. Chem. Chem. Phys.* 2008, **10**, 6615.

22. R. Krishnan, J.S. Binkley, R. Seeger and J.A. Pople, *J. Chem. Phys.* 1980, **72**, 650.

23. S. Simon, M. Duran, and J. J. Dannenberg, *J. Chem. Phys.*, 1996, **105**, 11024.

24. Gaussian 09, Revision **D.01**, M. J. Frisch, G. W. Trucks, H. B. Schlegel, G. E. Scuseria, M. A. Robb, J. R. Cheeseman, G. Scalmani, V. Barone, B. Mennucci, G. A. Petersson, H. Nakatsuji, M. Caricato, X. Li, H. P. Hratchian, A. F. Izmaylov, J. Bloino, G. Zheng, J. L. Sonnenberg, M. Hada, M. Ehara, K. Toyota, R. Fukuda, J. Hasegawa, M. Ishida, T. Nakajima, Y. Honda, O. Kitao, H. Nakai, T. Vreven, J. A. Montgomery, Jr., J. E. Peralta, F. Ogliaro, M. Bearpark, J. J. Heyd, E. Brothers, K. N. Kudin, V. N. Staroverov, R. Kobayashi, J. Normand, K. Raghavachari, A. Rendell, J. C. Burant, S. S. Iyengar, J. Tomasi, M. Cossi, N. Rega, J. M. Millam, M. Klene, J. E. Knox, J. B. Cross, V. Bakken, C. Adamo, J. Jaramillo, R. Gomperts, R. E. Stratmann, O. Yazyev, A. J. Austin, R. Cammi, C. Pomelli, J. W. Ochterski, R. L. Martin, K. Morokuma, V. G. Zakrzewski, G. A. Voth, P. Salvador, J. J. Dannenberg, S. Dapprich, A. D. Daniels, Ö. Farkas, J. B. Foresman, J. V. Ortiz, J. Cioslowski, and D. J. Fox, Gaussian, Inc., Wallingford CT, 2009.

25. Y. Mo, L. C. Song and Y. C. Lin, *J. Phys. Chem. A*, 2007, **111**, 8291.

26. J. D. Graham, A. M. Buytendyk, D. Wang, K. H. Bowen and K. D. Collins, *Biochemistry*, 2014, **53**, 344.

27. R. B. Metz, A. Weaver, S. E. Bradforth, T. N. Kitsopoulos, and D. M. Neumark, *J. Phys. Chem.*, 1990, **94**, 1377.

28. S. E. Bradforth, A. Weaver, D. W. Arnold, R. B. Metz, D. M. Neumark, *J. Chem. Phys.*, 1990, **92**, 7205.

29. Meot-Ner (Mautner), M. *J. Am. Chem. Soc.*, 1988, **110**, 3075.

VI. Solvent Stabilization of Unstable Anions

Many anions that are stable in the condensed phase are actually unstable in isolation. Solvent stabilization lowers the energy of the anion below that of the neutral. Clusters composed of these unstable anions and solvent molecules are the ideal region of interest to study solvent stabilization effects on anions. For instance, many unstable anions can be observed by mass spectroscopy when solvated by water, i.e. $X^-(H_2O)_n$. To first order, the number of solvent molecules required to stabilize an anion is an indicator of the degree of instability of the anion. Additionally, the energetics of these clusters are well suited to being studied by anion photoelectron spectroscopy. Sequential solvation shifts in electron affinities and vertical detachment energies are instructive in understanding the solvation effect.

Naphthalene is a somewhat common negative ion in organic chemistry, but does not actually have a positive electron affinity. This lab has previously shown that a single water molecule is enough to stabilize the naphthalene anion.[1] Additionally, electron affinities of larger naphthalene$(H_2O)_n$ clusters were used to extrapolate to the electron affinity of the monomer. This method yields an electron affinity estimate of -0.20 eV which is in excellent agreement with the -0.19 eV value determined by electron transmission spectroscopy.

Here, we extend this method of studying unstable anions to formaldehyde, acetaldehyde, and acetone. Electron transmission spectroscopy measurements indicate that these three carbonyl-containing molecules have greater negative electron affinities

than naphthalene and thus should require more than one solvent water molecule to stabilize the anion. Indeed, we observe the minimum number of water molecules necessary to stabilize the anions to be 2, 3, and 4 for formaldehyde, acetaldehyde, and acetone, respectively. Photoelectron spectra of observed clusters were recorded and various methods were attempted to try and extrapolate the negative electron affinity of the monomer. Additionally, the calculated vertical electron attachment, VEA, values of the monomers were determined.

References

1. S.A. Lyapustina, S. -J. Xu, M. Nilles, and K.H. Bowen, *J. Chem. Phys.*, **112**, 6643-6648 (2000).

VI.1 Solvent Stabilization of Formaldehyde, Acetaldehyde, and Acetone Anions

Xinxing Zhang, Jacob Graham, Haopeng Wang, and Kit Bowen

Department of Chemistry, Johns Hopkins University, Baltimore, MD 21218, USA

Eric Van Dornshuld, Blake A. Sowers, and Gregory S. Tschumper

Department of Chemistry and Biochemistry, University of Mississippi, University, MS, 38677, USA

VI.1.1 Abstract

We have studied the hydrated anions of formaldehyde, acetaldehyde, and acetone, i.e., $(H_2C{=}O)^-(H_2O)_n$, $(CH_3HC{=}O)^-(H_2O)_n$, and $[(CH_3)_2C{=}O]^-(H_2O)_n$, respectively. Mass spectra showed the threshold numbers of water molecules needed to stabilize the unstable anions of formaldehyde, acetaldehyde, and acetone to be n = 2, 3, and 4, respectively. Anion photoelectron spectra provided both photoelectron threshold energy, E_T, and vertical detachment energy, VDE. Calculated vertical electron attachment, VEA, values of the monomers were determined and compared with several extrapolated values from photoelectron spectra.

VI.1.2 Introduction

The simple carbonyl-containing molecules; formaldehyde, $H_2C{=}O$, acetaldehyde, $CH_3HC{=}O$, and acetone, $(CH_3)_2C{=}O$, all possess negative, adiabatic, valance electron affinities.[1,2] As a result, their anions are extremely short-lived, leading them to undergo dissociative electron attachment or autodetachment.[3-8] Of these three anions, acetone is

the most unstable as instability of these anions increases with methyl substitution. Van Veen et al. noted[5] that this can be reasoned from the electron donating methyl groups destabilizing the π* orbital that the excess electron fills. To some degree these anions could be considered neutral molecules perturbed by the presence of an excess electron. According to theory, these unstable anions all exhibit pyramidal structures with their α-carbon atoms located at the vertex and with their excess electrons occupying the carbonyl groups' π* anti-bonding orbitals.[1] In addition to temporary valence anions, acetaldehyde and acetone have also been found to support dipole bound anion states. While these ground state, dipole bound anions are stable, their measured electron binding energies are very small, e.g., 0.36 meV and 1.5 meV, respectively.[9-11] Hence, for the above three carbonyl molecules, their valence and dipole bond anions are either short-lived and unstable or very fragile.

So, how can anions that are unstable in the gas phase (in isolation) become stabilized? Solvation often accomplishes this task in condensed phases, vastly increasing the number of anions that can participate in chemical reactions. Solvation can also stabilize otherwise unstable anions within gas phase, anion-solvent molecule complexes (solvated anions), although the number of solvent molecules required varies with both the anion and the solvent. Examples of such complexes include the naphthalene anion,[12] the pyrimidine anion,[13] and the carbon dioxide anion[14-16] each stabilized and solvated by water molecules.

In the present work, we measured the photoelectron spectra of the hydrated anions of formaldehyde, acetaldehyde, and acetone, i.e., $(H_2C{=}O)^-(H_2O)_n$, $(CH_3HC{=}O)^-(H_2O)_n$, and $[(CH_3)_2C{=}O]^-(H_2O)_n$, respectively. Our mass spectra revealed the threshold numbers

of water molecules needed to stabilize the unstable anions of formaldehyde, acetaldehyde, and acetone to be n = 2, 3, and 4, respectively.

Previous investigations of relevance to the present work include FT-ICR studies of charge transfer reactions between $(H_2O)_n^-$ and both acetaldehyde and acetone to yield $(CH_3HC{=}O)^-(H_2O)_n$, and $[(CH_3)_2C{=}O]^-(H_2O)_n$, respectively[17] as well as anion photoelectron spectroscopic work on $[(CH_3)_2C{=}O]^-(H_2O)_n$.[18] Our results are compared with those from both studies.

VI.1.3 Experimental Methods

Anion photoelectron spectroscopy is conducted by crossing a mass-selected, negative ion beam with a fixed-energy photon beam and analyzing the energies of the resultant photodetached electrons. This technique is governed by the well-known energy-conserving relationship, hν = EBE + EKE, where hν, EBE, and EKE are the photon energy, electron binding energy (photodetachment transition energy), and the electron kinetic energy, respectively.

Our photoelectron spectrometer, which has been described elsewhere,[19] consists of a laser-based anion source, a linear time-of-flight mass spectrometer, a mass gate, a momentum decelerator, a neodymium-doped yttrium aluminum garnet (Nd:YAG) laser operated at third harmonic (355 nm) for photodetachment, and a magnetic bottle, electron energy analyzer with a resolution of 35 meV at EKE = 1 eV. The photoelectron spectra were calibrated against the well-known photoelectron spectrum of Cu^-.[20]

All anions in this work were generated by a laser-based anion source in which photo-emitted electrons interacted with sample molecules entrained in a helium expansion jet. Photoelectrons were produced by focusing the pulsed (10 Hz), second

harmonic (532 nm) output of a Nd:YAG laser onto a spirally rotating, copper disk, positioned just below the axis of a pulsed valve's expansion jet. In each case, a few drops of a mixture of water and the aldehyde sample of interest, i.e., formaldehyde (formalin), acetaldehyde, or acetone, was deposited inside the pulsed valve itself. The resulting anions were then extracted and mass-selected prior to photodetachment.

VI.1.4 Computational Methods

The vertical electron affinities (VEAs) for formaldehyde, acetaldehyde, and acetone in the gas phase were determined by performing density functional theory (DFT) computations on both the neutral molecule and the corresponding anion in a wide range of solvents using the polarizable continuum model (PCM). The energy difference (ΔE) between the neutral molecule and its negative ion (both at the optimized gas phase geometry of the neutral molecule) were computed in 13 different solvents with dielectric constants (ε) ranging from 78.4 (water) to 1.43 (argon).

$$\Delta E = E(\text{optimized neutral geometry}) - E(\text{anion of the optimized neutral geometry}) \quad (1)$$

The VEA in the gas phase (where $\varepsilon = 1.0$) was estimated by using a linear regression model on these quantities. The ΔE values computed in implicit solvents were plotted as a function of the inverse of the dielectric constant ($1/\varepsilon$) for formaldehyde (Figure VI.1.1), acetaldehyde (Figure VI.1.2) and acetone (Figure VI.1.3). The gas phase VEA was then determined for $1/\varepsilon = 1.0$ from the equation for the best-fit line for the data.

$$\text{VEA} = \lim_{\varepsilon \to 1} \Delta E(1/\varepsilon) \quad (2)$$

Previous implementations of this procedure on small molecules have exhibited a very strong linear correlation with reported correlation coefficients (r^2) exceeding 0.999. The technique has also been shown to provide VEAs that typically deviate by no more than one or two tenths of n eV from electron affinities obtained via experimental electron transmission spectroscopy (ETS) measurements[21-22]. For example, the VEA of acetone computed by this procedure in Reference 22 was found to be -1.46 eV, which is very close to the ETS value of -1.51 eV[8].

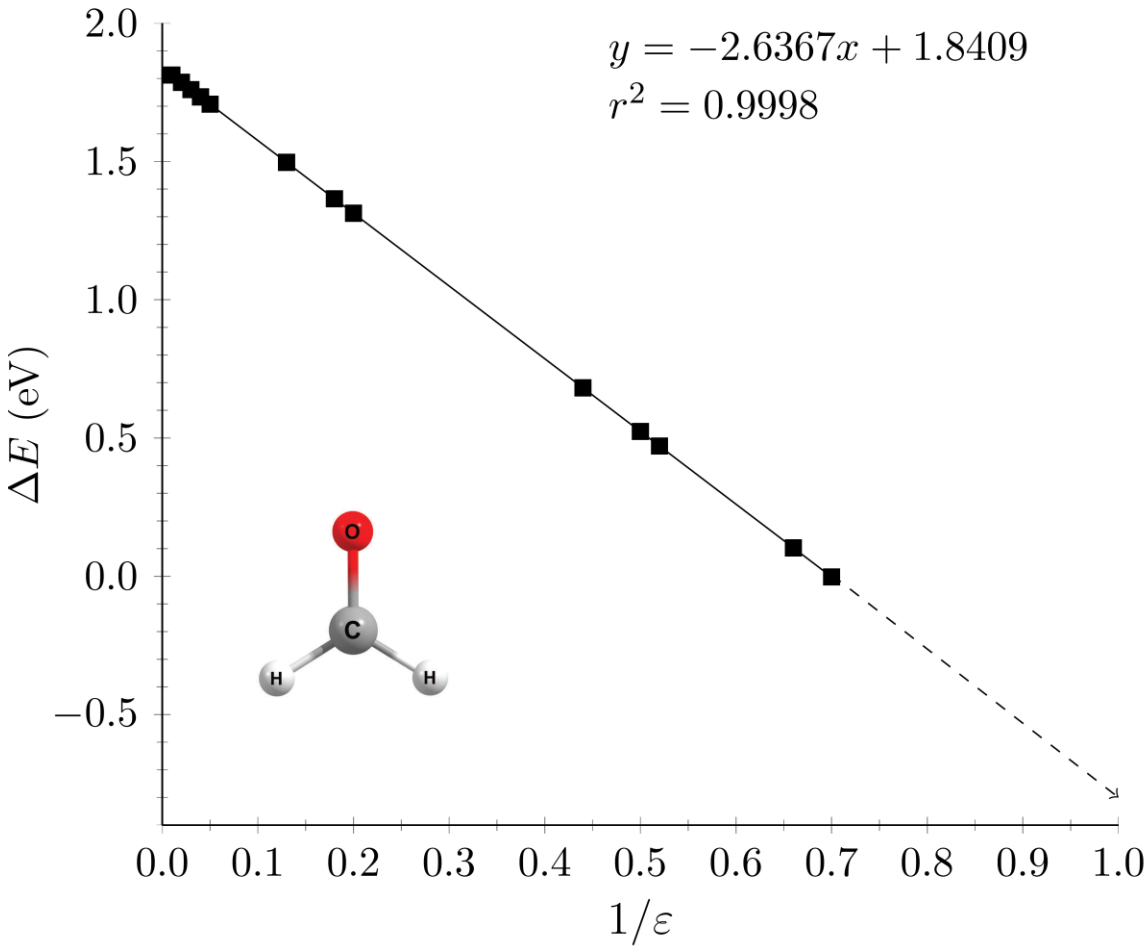

Figure VI.1.1: The inverse relationship between ΔE and ε for formaldehyde (C_{2v}) with a correlation coefficient of 0.9998 leads to an estimated VEA of -0.80 eV in the gas phase ($1/\varepsilon = 1.0$).

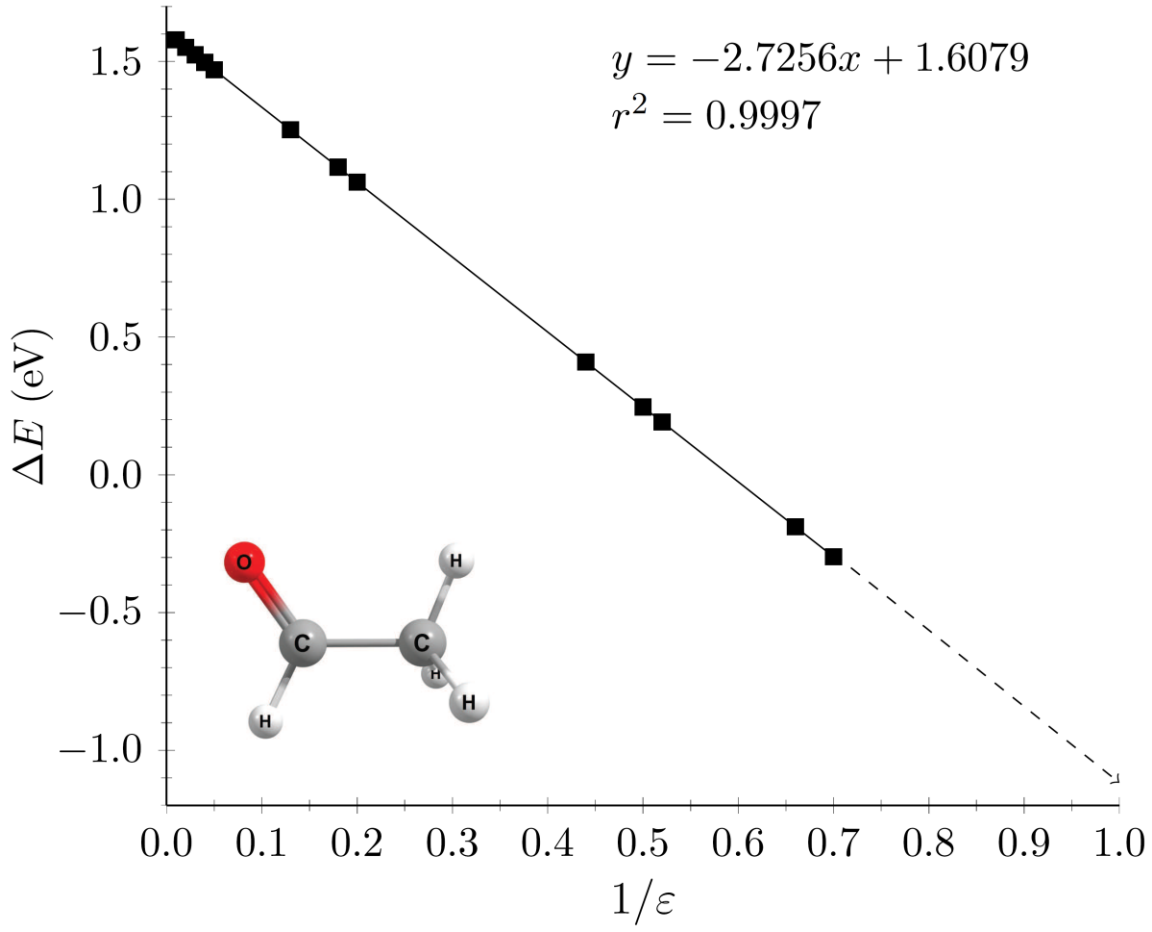

Figure VI.1.2: The inverse relationship between ΔE and ε for acetaldehyde (C_s) with a correlation coefficient of 0.9997 leads to an estimated VEA of -1.12 eV in the gas phase ($1/\varepsilon = 1.0$).

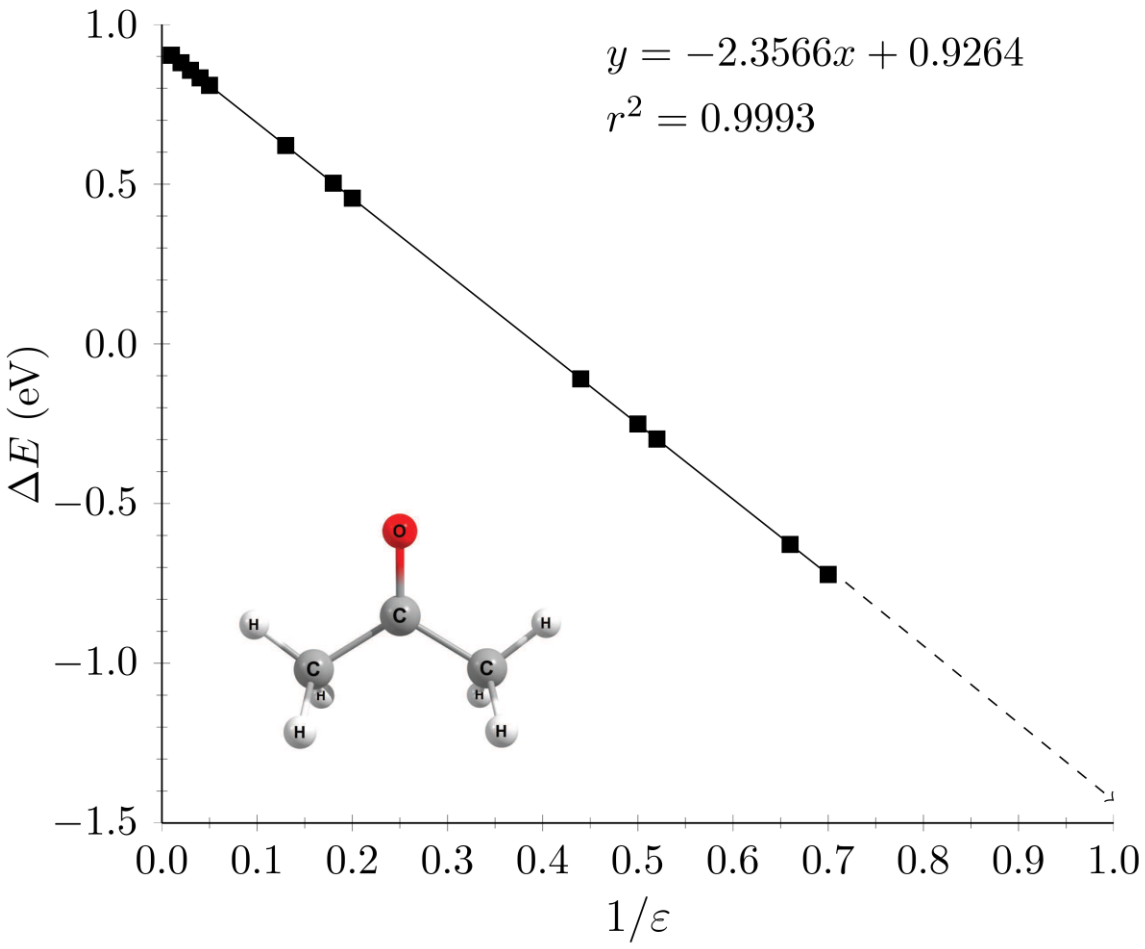

Figure VI.1.3: The inverse relationship between ΔE and ε for acetone (C_{2v}) with a correlation coefficient of 0.9993 leads to an estimated VEA of -1.43 eV in the gas phase ($1/\varepsilon = 1.0$).

Full optimizations were performed on the neutral species (corresponding point group symmetries in parenthesis) of formaldehyde (C_{2v}), acetaldehyde (C_s), and acetone (C_{2v}) with the B3LYP[23-24] method in conjugation with the split-valence 6-31+G(d) basis set.[25] These fixed geometries were used to compute the B3LYP/6-311+G(2df,p)[26-27] electronic energies of the neutral and anion with the PCM in a variety of solvents (corresponding ε in parentheses): water (78.4), dimethylsulfoxide (46.7), acetonitrile

(36.6), ethanol (24.5), acetone (20.7), tetrahydrofuran (7.6), chlorobenzene (5.6), chloroform (4.9), benzene (2.25), cyclohexane (2.02), heptane (1.92), krypton (1.52), and argon (1.43). All computations were performed with Gaussian 09[28] using default convergence criteria, numerical integration grids, basis set conventions, and PCM solvent parameters.

In addition to determining the negative VEA's of the monomers, we optimized candidate anion geometries of $(H_2C{=}O)^-(H_2O)_n$, $(CH_3HC{=}O)^-(H_2O)_n$ and $[(CH_3)_2C{=}O]^-(H_2O)_4$ for n=0-4. Here, both geometry optimizations and energy calculations were performed at the second-order, Moller-Plesset perturbation (MP2) level of theory[29] with aug-cc-pVDZ basis sets.[30,31] The vertical detachment energy (VDE) was calculated by subtracting the energy of the relaxed anion from the energy of a neutral cluster in the anion's geometry. Optimizing each anion's geometry as a neutral species yields neutral geometries and energies. The adiabatic electron affinity (EA) was then determined by subtracting the energy of the relaxed anion from the relaxed neutral.

VI.1.5 Results

Figure VI.1.4 displays the mass spectra of all three systems studied here. The mass spectrum in Figure VI.1.4 (a) shows peaks due to $(H_2C{=}O)^-(H_2O)_n$, and $(H_2C{=}O)_2^-(H_2O)_m$ cluster anions, where n = 2 and m = 1 are the threshold numbers of water solvent molecules needed to stabilize their respective cluster anions. The mass spectrum in Figure VI.1.4 (b) displays the peaks due to $(CH_3HC{=}O)^-(H_2O)_n$ and $(CH_3HC{=}O)_2^-(H_2O)_m$, where n = 3 and m = 2 are, respectively, the threshold numbers of water solvent molecules required to stabilize their particular anions. The mass spectrum in Figure

VI.1.4 (c) shows peaks due to $[(CH_3)_2C=O]^-(H_2O)_n$, where n = 4 is the threshold number of water solvent molecules needed to stabilize the acetone anion. Peaks due to $(H_2O)_n^-$ cluster anions are also apparent in this mass spectrum. No masses, having the above stoichoimetries, were detected below their stated threshold sizes.

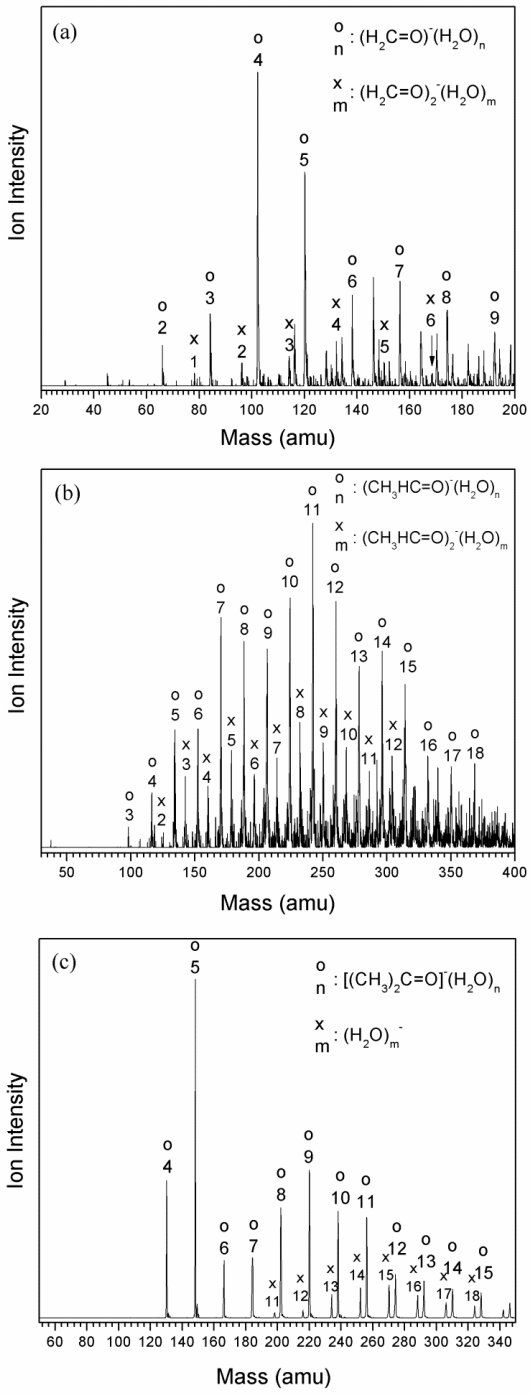

Figure VI.1.4: Mass spectra of (a) $(H_2C=O)^-(H_2O)_n$, and $(H_2C=O)_2^-(H_2O)_m$, (b) $(CH_3HC=O)^-(H_2O)_n$ and $(CH_3HC=O)_2^-(H_2O)_m$, and (c) $[(CH_3)_2C=O]^-.(H_2O)_n$ and $(H_2O)_n^-$.

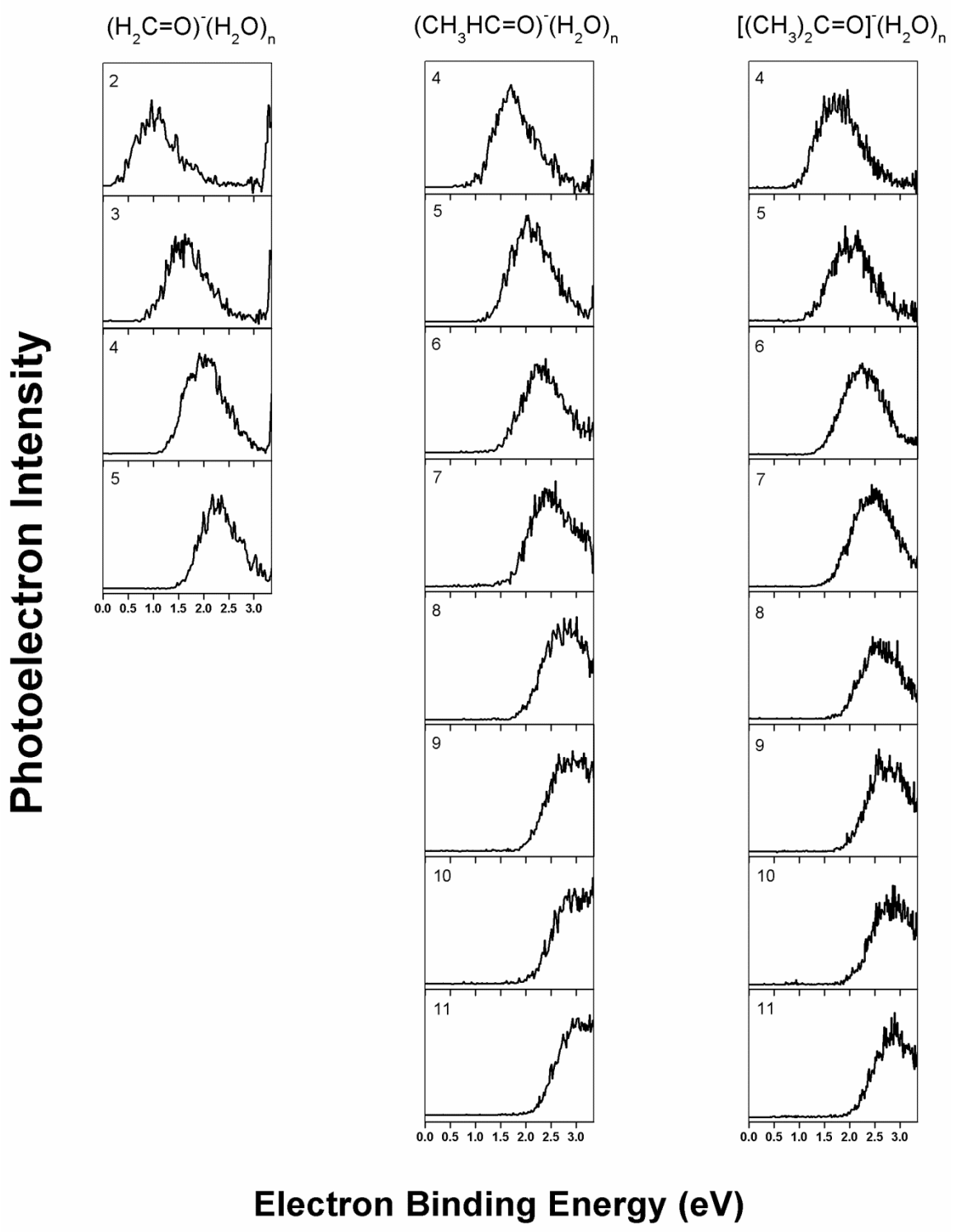

Figure VI.1.5: Anion photoelectron spectra of $(H_2C{=}O)^-(H_2O)_n$, $(CH_3HC{=}O)^-(H_2O)_n$ and $[(CH_3)_2C{=}O]^-(H_2O)_n$, all measured with 3.49 eV photons.

The anion photoelectron spectra of $(H_2C{=}O)^-(H_2O)_{n=2\text{-}5}$, $(CH_3HC{=}O)^-(H_2O)_{n=4\text{-}11}$, and $[(CH_3)_2C{=}O]^-(H_2O)_{n=4\text{-}11}$ is presented in Figure VI.1.5. All of these photoelectron spectra were recorded using 355 nm (3.49 eV) photons. While $(CH_3HC{=}O)^-(H_2O)_3$ was observed in the mass spectrum, its low ion intensity precluded our acquiring its photoelectron spectrum. Also, because ion intensities for cluster anions at their hydration threshold sizes are often weak, their photoelectron spectra tend to display lower signal-to-noise ratios than larger cluster anions in the same system.

All of the photoelectron spectra recorded in this study exhibit broad spectral bands. Nevertheless, two quantities can be extracted from each of them. These are the vertical detachment energy, VDE, and the photoelectron threshold energy, E_T. The EBE value corresponding to the intensity maximum in a given band is its VDE value, the transition energy at which the Franck Condon overlap between the wavefunctions of the anion and its neutral counterpart is maximal. The photoelectron threshold energy is the EBE value near where photoelectrons first appear in the spectrum. We have estimated E_T values by extrapolating the low EBE side of each band to zero, with the corresponding EBE value there being taken as the E_T value. All VDE and E_T values extracted from the photoelectron spectra in Figure VI.1.5 are tabulated in Table VI.1.1.

The gas phase VEAs for formaldehyde, acetaldehyde, and acetone predicted by the PCM extrapolation procedure described earlier are -0.80 eV, -1.12 eV, and -1.43 eV, respectively. Linear correlation coefficients (r^2) were larger than 0.999 for all three systems. The minor difference (0.03 eV) between the VEA for acetone computed here and that reported in Reference 22 are due to minor changes between Gaussian 09 and earlier versions of the program. The computed gas phase VEAs are very close to the

experimental ETS VEA values of -0.86 eV for formaldehyde, -1.19 eV for acetaldehyde, and -1.51 eV for acetone [5-8].

Table VI.1.2 summarizes calculated EA and VDE values determined from optimized anion and neutral geometries for clusters solvated by up to four water molecules. It should be noted that with this method the magnitudes for the negative electron affinities of the monomers have very poor agreement with ETS values and our computationally extrapolated VEA values (i.e. here acetone has the *least* negative EA). However, the results accurately predict the number of water molecules necessary to stabilize an anion and calculated observable VDEs are consistent with experiment.

Table VI.1.1: Experimental photoelectron threshold energy (E_T) and vertical detachment energy (VDE) values of the systems studied. All values (in eV) are uncertain by ± 0.1 eV.

	$(H_2C=O)^-(H_2O)_n$		$(CH_3HC=O)^-(H_2O)_n$		$[(CH_3)_2C=O]^-(H_2O)_n$	
n	E_T	VDE	E_T	VDE	E_T	VDE
0	-	-	-	-	-	-
1	-	-	-	-	-	-
2	0.4	1.0	-	-	-	-
3	0.9	1.5	*	*	-	-
4	1.3	2.0	1.0	1.7	0.9	1.7
5	1.6	2.3	1.3	2.0	1.3	2.0
6			1.6	2.3	1.5	2.2
7			1.8	2.5	1.7	2.5
8			2.0	2.8	1.9	2.7
9			2.1	2.9	2.0	2.8
10			2.2	3.0	2.1	2.9
11			2.3	3.1	2.2	3.0

*This species was observed in our mass spectra, but due to its low ion intensity, its photoelectron spectrum was not recorded.

Table VI.1.2: Calculated values of EA and VDE for all species studied with up to four solvent water molecules. All values are in eV.

	$(H_2C=O)^-(H_2O)_n$		$(CH_3HC=O)^-(H_2O)_n$		$[(CH_3)_2C=O]^-(H_2O)_n$	
n	EA	VDE	EA	VDE	EA	VDE
0	-1.0	-0.8	-0.7	-0.7	-0.6	-0.6
1	-0.3	0.2	-0.6	0.2	-0.5	-0.5
2	0.2	1.1	-0.1	0.9	-0.2	0.9
3	0.3	1.6	0.1	1.5	-0.1	1.5
4	0.5	2.2	0.3	2.0	0.1	1.9

VI.1.6 Discussion

During this work, we observed the minimum numbers of water molecules needed to stabilize the unstable, parent anions of formaldehyde, acetaldehyde, and acetone to be n = 2, 3, and 4, respectively. These results are consistent with the work of others. The FT-ICR studies of Beyer et al.[15] found the minimum number of water molecules necessary to stabilize the acetaldehyde and the acetone anions to be 3 and 4, respectively. While the photoelectron spectroscopic work by Nagata et al.[16] focused primarily on homogeneous acetone cluster anions, it also presented plots of VDE values and anisotropy parameters for $[(CH_3)_2C=O]^-(H_2O)_{n=4-9}$. Our work agrees with them both in regard to their observed threshold size and their reported VDE values. In the case of hydrated formaldehyde anions, $(H_2C=O)^-(H_2O)_n$, where we found the minimum number of water molecules

necessary to stabilize the formaldehyde anion to be 2, there had been no previous observation of these species. Additionally, we determined VEA values of the monomers computationally by PCM extrapolation. These values agree well with VEA values obtained experimentally by ETS and are summarized in Table VI.1.3.

Even though it is tempting to assume that the E_T values tabulated in Table VI.1.1 are equivalent to EA values, this is probably not the case. Presumably, the EA value of the threshold cluster size in each system is a small, positive number, i.e., not far above zero. Nevertheless, the measured E_T values for the threshold sizes seen in this study are significantly greater than zero, *i.e.,* 0.4 eV for $(H_2C{=}O)^-(H_2O)_2$ and 0.9 eV for $[(CH_3)_2C{=}O]^-(H_2O)_4$. The reason for the mismatch between E_T and EA presumably stems from structural differences between hydrated anions and their neutral counterparts. In all of the hydrated cluster anions studied here, these differences are likely to be large enough to prevent Franck-Condon overlap at their photodetachment origin transitions. This notion is additionally supported by our computed EA values as they are consistently smaller than our observed E_T values. For instance, our calculated EA value of $[(CH_3)_2C{=}O]^-(H_2O)_4$ is 0.1 eV while our observed E_T is 0.9 eV.

Nevertheless, the photoelectron spectra still carry important energetic information. In particular, the differences in VDE (and perhaps in E_T) values between photoelectron spectra of adjacent size cluster anions, i.e., their spectral shifts, may approximate the differences in the EBE values of their corresponding (unseen) origin transitions; VDE differences approximately track with EA differences. Since VDE = EA + RE, where RE is the reorganization energy of the anion's neutral counterpart during photodetachment, this rough approximation is based on the assumption that RE values do not vary greatly

among the solvated anions of a given system and that the structural relationship between solvated anions and their neutral counterparts likewise does not vary too much with size. This approximation leads to several implications, all of which are worth exploring.

First, a rough consistency check can be made by using our experimental VDE values of $(H_2C{=}O)(H_2O)_n$ to estimate the EA of the monomer. With $(H_2C{=}O)(H_2O)_n$, we can utilize the measured VDE difference between n = 3 and n = 2, i.e., 0.5 eV, to estimate EA values and then to compare these with experimental ETS values. We expect the EA value of the n = 2 threshold size to be between 0 eV and our measured threshold value of 0.4 eV. Next, consider the estimated EA value of n = 1. If we set 0 eV to be the EA value for n = 2 and the VDE difference to be 0.5 eV, even though the measured VDE difference between n = 2 and n = 1 is not available, we can roughly predict EA value for n = 1 is estimated to be -0.5 eV. Of course, if we set 0.4 eV to be the EA value for n = 2, we arrive at -0.1 eV for the EA of n=1. This give us a range of -0.5 eV to -0.1 eV for the EA of $(H_2C{=}O)(H_2O)$. If we extend this analysis to n=0 we arrive at an EA range between -1.0 eV and -0.6 eV. Although VEA and EA are different physical quantities, this range is consistent with the experimental ETS VEA value of -0.86 eV.

If one knew the size-dependences of the EA values of the three, hydrated cluster anion systems under study here, then the EA values of their three molecular (un-hydrated) aldehydes could be estimated by extrapolating the polynomial fits of their data points. By assuming the EA value of the threshold size in each system to be zero and utilizing successive VDE differences, $VDE_n - VDE_{n-1}$ (computed from VDE data in Table VI.1.1), EA values could be referenced to the zero, threshold size value and

estimated for each cluster size, n. Plots of estimated EA versus n, determined in this manner, are presented in Figure VI.1.6 for all three hydrated cluster anions under study here. The extrapolated molecular EA values (at n = 0) in each case are -1.60 eV for $H_2C=O$, -1.37 eV for $CH_3HC=O$, and -1.59 eV for $(CH_3)_2C=O$. Unfortunately, while this method's EA estimation $(CH_3)_2C=O$ would appear to be consistent with its measured ETS VEA value of -1.51 eV, $H_2C=O$ and $CH_3HC=O$ deviate unacceptably from their respective ETS VEA values of -0.86 eV and -1.19 eV.

Table VI.1.3: Summary. All values are in eV.

	Formaldehyde	Acetaldehyde	Acetone
Critical number of water molecules necessary to stabilize the anion	2	3	4
VEA from ETS	-0.86	-1.19	-1.51
VEA from PCM extrapolation	-0.8	-1.12	-1.43
Et extrapolated to n=0 with 3rd order polynomial fit	-0.9	-1.08	-1.54

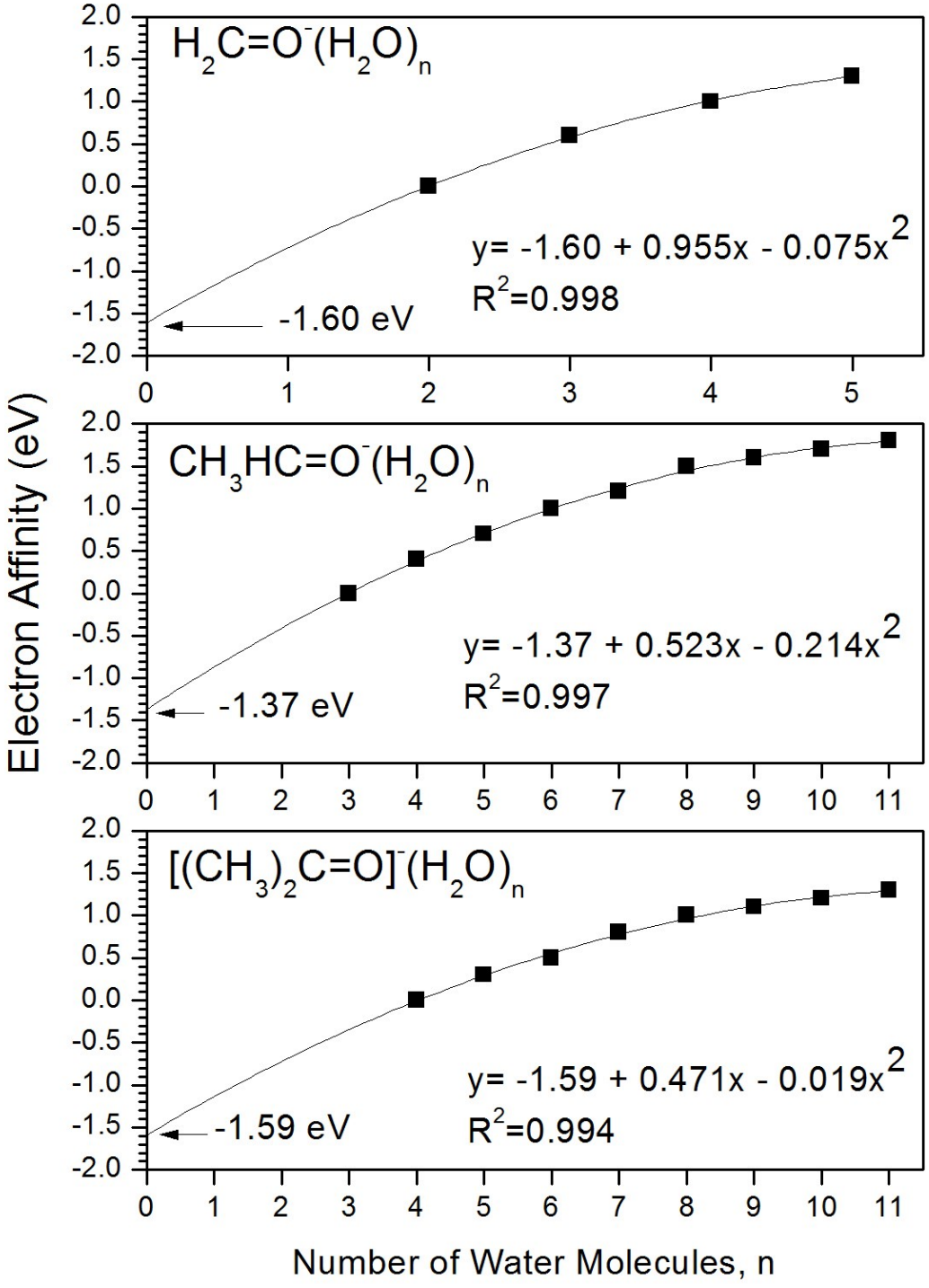
$H_2C=O^-(H_2O)_n$
y= -1.60 + 0.955x - 0.075x^2
R^2=0.998
-1.60 eV
$CH_3HC=O^-(H_2O)_n$
y= -1.37 + 0.523x - 0.214x^2
R^2=0.997
-1.37 eV
$[(CH_3)_2C=O]^-(H_2O)_n$
y= -1.59 + 0.471x - 0.019x^2
R^2=0.994
-1.59 eV
Electron Affinity (eV)
Number of Water Molecules, n

Figure VI.1.6: Plots of estimated EA values versus hydration sizes, n, for $(H_2C{=}O)(H_2O)_n$, $(CH_3HC{=}O)(H_2O)_n$ and $[(CH_3)_2C{=}O](H_2O)_n$. These data points have been fitted to polynomials and extrapolated to n = 0.

Again, by assuming that the EA value of a given threshold size lies between zero and the E_T value for that threshold size, the application of the extrapolation method described above yields a range of possible EA values for the molecule under consideration. These ranges are between -1.2 eV and -1.60 eV for $H_2C{=}O$, between -0.7 eV and -1.37 eV for $CH_3HC{=}O$, and between -0.7 eV and -1.59 eV for $(CH_3)_2C{=}O$. However, for the EA of $H_2C{=}O$, the -1.2 to -1.60 eV range does not overlap the calculated experimental ETS VEA value of -0.86 eV. Taken as a whole, the variation in molecular EA values, determined by this extrapolation method, suggests that the underlying approximations are too crude to provide more than broad estimates.

However, it should be noted that extrapolating measured threshold energies, E_T, to n=0 with a 3rd order polynomial fit yields interesting results. This extrapolation is shown in Figure VI.1.7 and results included in Table VI.1.3. This extrapolation yields values of -0.90 eV for formaldehyde, -1.08 eV for acetaldehyde, and -1.54 eV for acetone. These results are highly consistent with ETS VEA values and our calculated VEA values. While a physical interpretation for this result is unclear, and it's possible the success of this extrapolation could be some combination of overfitting and error cancelling, the agreement between this extrapolation and measured ETS values is striking.

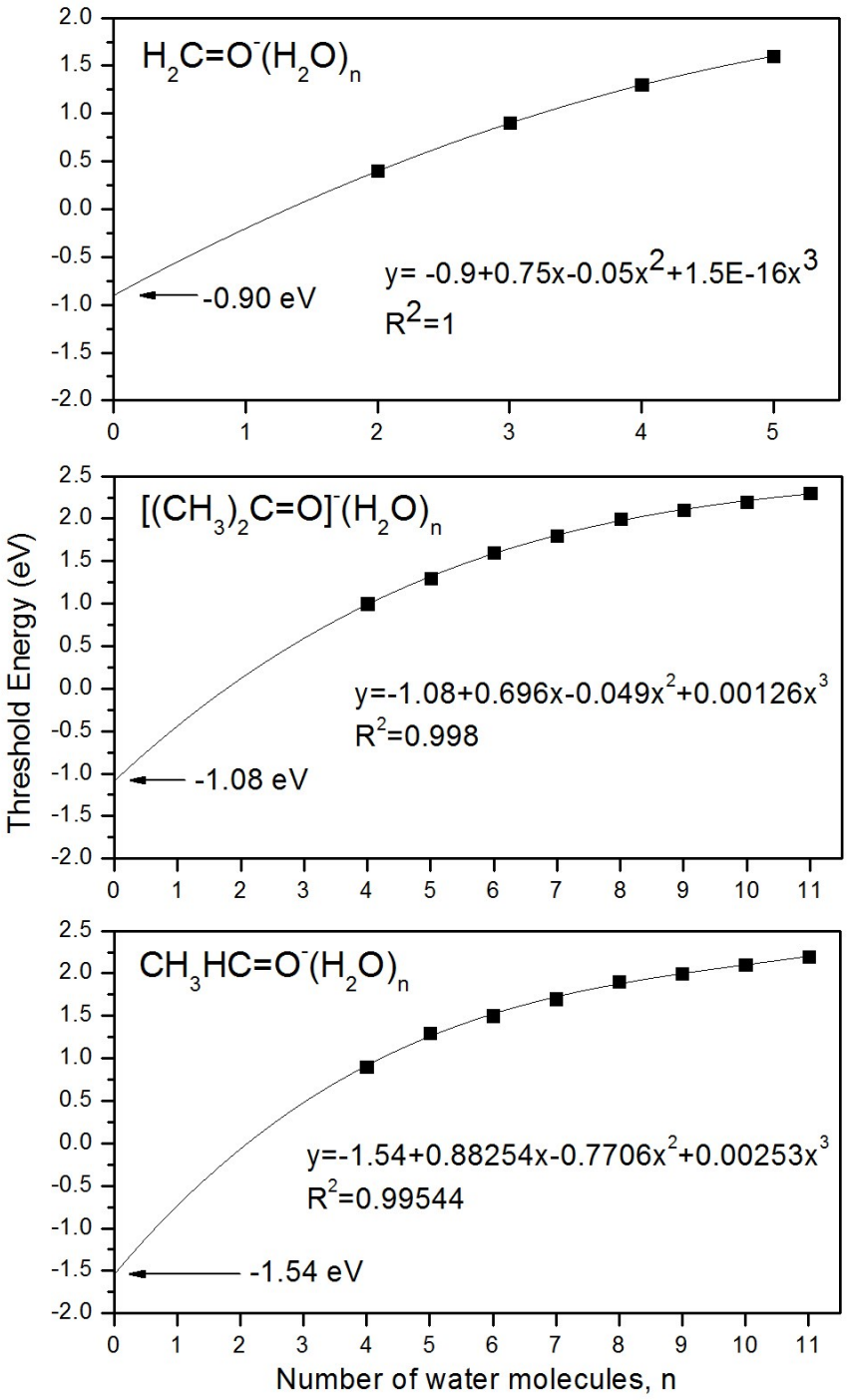

Figure VI.1.7: Plots of energy thresholds values versus hydration sizes, n, for $(H_2C{=}O)(H_2O)_n$, $(CH_3HC{=}O)(H_2O)_n$ and $[(CH_3)_2C{=}O](H_2O)_n$. A third order polynomial fitting is shown and n=0 intercepts are labeled.

Acknowledgements

This material is based upon work supported by the National Science Foundation under Grant Nos. CHE-1111693 (K.H.B.), EPS-0903787 (G.S.T.), and CHE-0957317 (G.S.T.).

References

1. I. Fourre, B. Silvi, P. Chaquin, and A. Sevin, *J. Comput. Chem.* **20**, 897 (1999).

2. D. Mariano, A. Vera, and A.P. Pierini, *Phys. Chem. Chem. Phys.* **6**, 2899 (2004).

3. W. T. Naff, R.N. Compton, and C. D. Cooper, *J. Chem. Phys.* **57**, 1303 (1972).

4. D. Jones, A. Modelli, P. R. Olivato, M. D. Colle, M. de Palo and G. Distefano, *J. Chem. Soc. Perkin Trans.* **2,** 1651 (1994).

5. E. H. van Veen, W. L. van Dijk, and H. H. Brongersma, *Chem. Phys.***16**, 337 (1976).

6. P. D. Burrow and J.A. Michejda, *Chem. Phys. Lett.* **42**, 223 (1976).

7. R. Dressler and M. Allan, *J. Electron Spectrosc. Relat. Phenom.* **41**, 275 (1986).

8. K. Jordan, P.D. Burrow, *Acc. Chem. Res.* **11**, 341 (1978).

9. C. Desfrancois, H. Aboul-Carime, N. Khelifa, and J. P. Schermann, *Phys. Rev. Lett.* **73**, 2436 (1994).

10. N. I. Hammer, K. Diri, K. D. Jordan, C. Desfrancois, and R. N. Compton, *J. Chem. Phys.* **119**, 3650 (2003).

11. N. I. Hammer, R. N. Compton, L. Adamowicz, S. G. Stepanian, *Phys. Rev. Lett.* **94**, 153004 (2005).

12. S.A. Lyapustina, S.-J. Xu, M. Nilles, and K.H. Bowen, *J. Chem. Phys.* **112**, 6643 (2000)

13. J. T. Kelly, S. Xu, J. Graham, J. M. Nilles, D. Radisic, A. M. Buonaugurio, K. H. Bowen, N. I. Hammer, and G. S. Tschumper, *J. Phys. Chem. A* **118**, 11901-11907(2014).

14. C. E. Klots, *J. Chem. Phys. 71, 4172 (1979).*

15. T. Tsukuda and T. Nagata, J. Phys. Chem. 107, 8476 (2003).

16. A. Muraoka, Y. Inokuchi, N. I. Hammer, J.-W. Shin, M.A. Johnson, and T. Nagata, J. Phys. Chem. A 113, 8942 (2009).

17. O. P. Balaj, C.-K. Siu, I. Balteanu, M. Beyer, and V. E. Bondybey, *Int. J. Mass Spectrom.* **238**, 65 (2004).

18. R. Nakanishi, A. Muraoka, and T. Nagata. *Chem. Phys. Lett.* **427**, 56 (2006).

19. M. Gerhards, O. C. Thomas, J. M. Nilles, W.J. Zheng, and K. H. Bowen, *J. Chem. Phys.* **116**, 10247 (2002).

20. J. Ho, K. M. Ervin, and W. C. Lineberger. *J. Chem. Phys.* **93**, 6987 (1990).

21. D. Mariano, A. Vera, B. Pierini. *Phys. Chem. Chem. Phys.* **6**, 2899-2903 (2004).

22. M. D. Puiatti, M. A. Vera, A. B. Adriana, *Phys. Chem. Chem. Phys.*, 2008, **10**, 1394-1399

23. A. D. Becke, *J. Chem. Phys.*, **98**, 5648−5652 **(**1993**).**

24. C. Lee, W. Yang, R. G. Parr, *Phys. Rev. B*, **37**, 785−789 (1988).

25. G. Fogarasi, X. Zhou, P. W. Taylor, P. Pulay, *J. Am. Chem. Soc.*, **114** (21), 8191-8201 (1992).

26. A. D. McLean, G. S. Chandler, *J. Chem. Phys.*, **72**, 5639 (1980).

27. R. Krishnan, J. S. Binkley, R. Seeger, J. A. Pople, *J. Chem. Phys.*, **72**, 650 (1980).

28. Frisch, M. J.; Trucks, G. W.; Schlegel, H. B.; Scuseria, G. E.; Robb, M. A.; Cheeseman, J. R.; Scalmani, G.; Barone, V.; Mennucci, B.; Petersson, G. A. et al. *Gaussian 09*, revision D.01. 2009; Gaussian Inc.: Wallingford, CT, 2009.

29. M. Head-Gordon, J. A. Pople, and M. J. Frisch, Chem. Phys. Lett. **153**, 503 (1988).

30. D. E. Woon and T. H. Dunning, Jr. J. Chem. Phys. **90**,1007 (1989).

31. D. E. Woon and T. H. Dunning, Jr. J. Chem. Phys. **98**, 1358 (1993).

VII. Appendix: Rydberg Electron Transfer

The Pulsed Source Apparatus (PSA) has been upgraded to add Rydberg electron transfer capability. This appendix contains design details and operational notes as well as progress and performance data. This work was performed alongside fellow graduate student Allyson Buytendyk and complimentary notes on Rydberg electron transfer can be found in the appendix section of her thesis.

Rydberg electron transfer (RET) involves the collisional transfer of an electron from a highly excited Rydberg atom to a target neutral species. The relatively large size of Rydberg atoms (~85nm Bohr radius for n=40) and low electron binding energy (~8 meV for n=40) makes them particularly suitable for collisional electron transfer. Although RET can be used as a method to generate "typical" valance anions, it is uniquely well suited to the production of dipole bound anions and low (<0.1eV) binding energy anions. Historically, the rate and Rydberg level dependence of anion formation was the sought after information obtained from RET as these were primarily mass spectroscopy experiments. Here, we have added RET capability to an existing anion photoelectron spectrometer with the goal of studying anions that are best prepared by RET with anion photoelectron spectroscopy.

There are a wide variety of methods previously used to generate Rydberg atoms. These include: electron bombardment of rare gases (Kondow[1]), discharge & optical pumping of rare gases (Schermann[2] and Hotop[3]), and optical pumping of alkali beams

(Compton[4] and Dunning[5]). From the advice of Compton, to maximize anion intensity, we have chosen optical pumping of alkali atoms.

VII.1 Rydberg Atoms

Atoms in highly excited electronic states are termed Rydberg atoms. In these atoms the core electrons shield the excited electron from the nucleus such that the excited atom has hydrogenic properties. A table of properties for hydrogen atoms as a function of principle quantum number, n, is given in Table VII.1.1.

Table VII.1.1: Properties of Highly Excited Hydrogen Atoms.

Property	n-dependence	n=1	n=25	n=50
Bohr Radius	$a_0 n^2$	0.053 nm	33 nm	132 nm
Binding Energy	R_∞/n^2	13.6 eV	21 meV	5 meV
Velocity of excited electron	v_0/n	2.2×10^6 m/s	8.8×10^4 m/s	4.4×10^4 m/s
Lifetime for ℓ=1	$\tau_0 n^3$	1 ns	15 µs	125 µs
Classical field detachment	E_1/n^4	3.2×10^8 V/cm	819 V/cm	51 V/cm

For alkali atoms, these properties can be scaled with an effective principle quantum number:

$$n^* = n - \delta_\ell$$

where n* is the effective principle quantum number, n is the principle quantum number and δ_ℓ is the ℓ-dependent quantum defect.

The binding energy of a Rydberg alkali atom can then be described by:

$$E_{n,\ell} = \frac{-R_\infty}{(n-\delta_\ell)^2}$$

where R_∞ is the Rydberg constant. For potassium, quantum defects are 2.19, 1.71, 0.25 for $\ell = 0$, 1 and 2, respectively.

Optical excitations of alkali atoms obey the LaPorte selection rule where $\Delta\ell = \pm 1$. For ground state potassium in a ^{2}S state this limits transitions to p states. Two color excitation, through a p state resonance, yields $\Delta\ell = 0, \pm 2$. Therefore with two color excitation of ^{2}S potassium, s and d Rydberg states are allowed. A two color pumping scheme for potassium is shown in Figure VII.1.1.

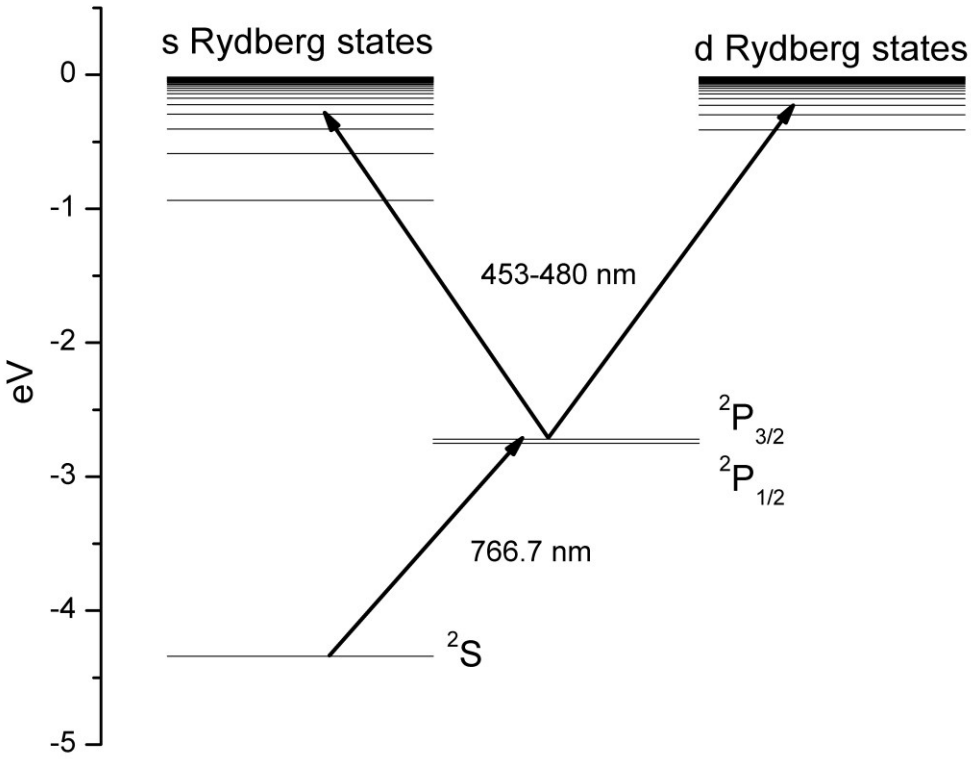

Figure VII.1.1: Two Color Optical Pumping Scheme for Potassium

Electron transfer collisions between Rydberg atoms and neutral species are influenced by a wide variety of conditions. Some of these factors include the velocity of the collision, the Rydberg n level, the ℓ value of the Rydberg state, and the cross section of the neutral target for low energy electron attachment. The dependence on these parameters haven been explored by a variety of researchers. Schermann and co-workers[2] examined the collision energy dependence between Rydberg atoms and SF_6. RET at low collision energies can produce ion pair complexes where the resulting cation (K^+) does not separate from the anion product (SF_6^-). For example:

$$K^{**} + SF_6 \rightarrow K^+SF_6^-$$

Naturally, this condition is undesirable for production of anions. By varying the collision energy Schermann was able to demonstrate that above n* = 8 for SF_6 seeded in helium, no appreciable quantities of ion-pairs are formed. However for SF_6 at thermal energies, ion pair production dominates until n*=25. Compton and co-workers[4] demonstrated the ℓ dependence of RET and found that d states have higher RET rate constants than s states. Dunning and co-workers[5] quantified some cross sections for low energy electron attachment with RET. For SF_6, cross sections approaching 10^3 Å^2 are observed.

VII.2 Chamber design

Initially, the Pulsed Source Apparatus used a single large cubic vacuum chamber (Chamber 0) to house both an ion source and time-of-flight extraction plates. Ideally for RET, the alkali oven and target neutral beam should be generated in individually pumped vacuum chambers and both should intersect inside the ion extraction region of our time of flight mass spectrometer. This extraction region should also be accessible to the output of two dye lasers. An idealized overview of how the two laser beams, pulsed valve output and alkali beam intersect in the time-of-flight ion extraction region is shown in Figure VII.2.1.

A new chamber was designed (shown in Figure VII.2.2) that incorporates the design goals outlined above. An “internal box” concept was used where the time-of-flight extraction plates are located in a vacuum chamber inside a larger vacuum chamber. The larger vacuum chamber that surrounds the “internal box” provides an intermediate or differential pumping region between the RET collision region and both the alkali oven chamber and the skimmed output of the Chamber 0 Ion Source Chamber. This chamber was built by Kurt J. Lesker and detailed plans for this chamber are found on the fileserver under Public/Shared Documents/PSA Documents/Lesker. Naming schemes for vacuum regions inside instruments in this lab are incremented from the ion source chamber “Chamber 0”. So, this new chamber is referred to as “Chamber 1” and the internal box is referred to as “Chamber 2”.

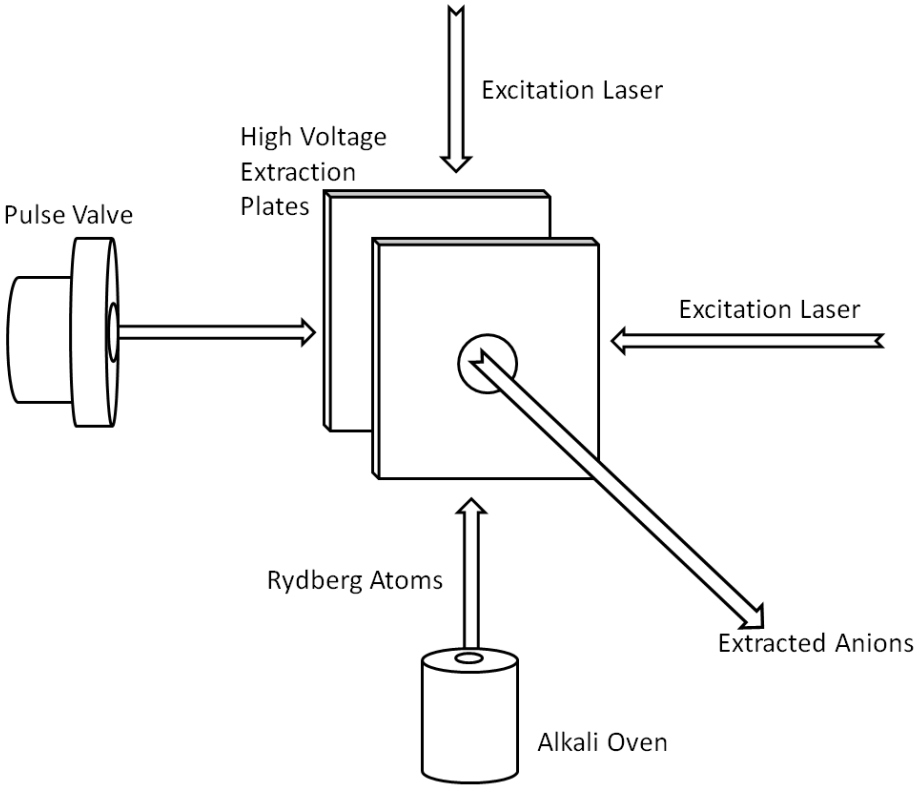

Figure VII.2.1: Rydberg Electron Transfer Overview

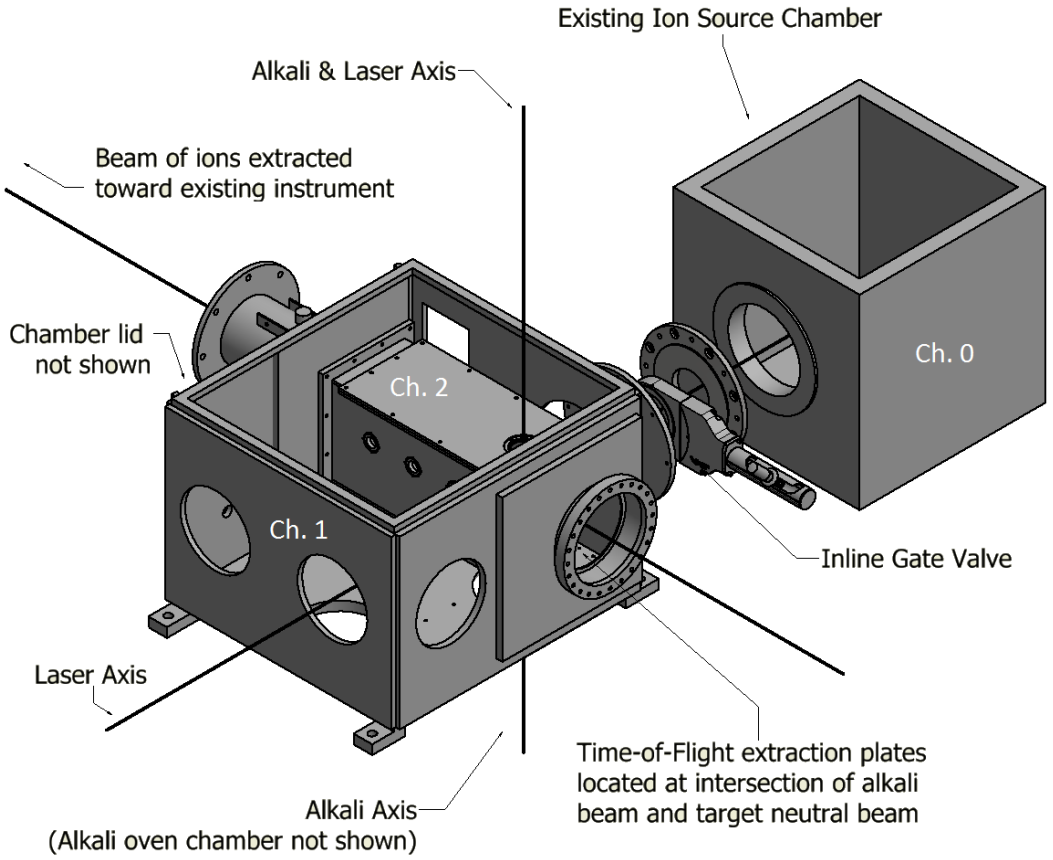

Figure VII.2.2: Newly Designed Vacuum Chamber with RET Collision Region. Chamber 0, 1, and 2 are labeled.

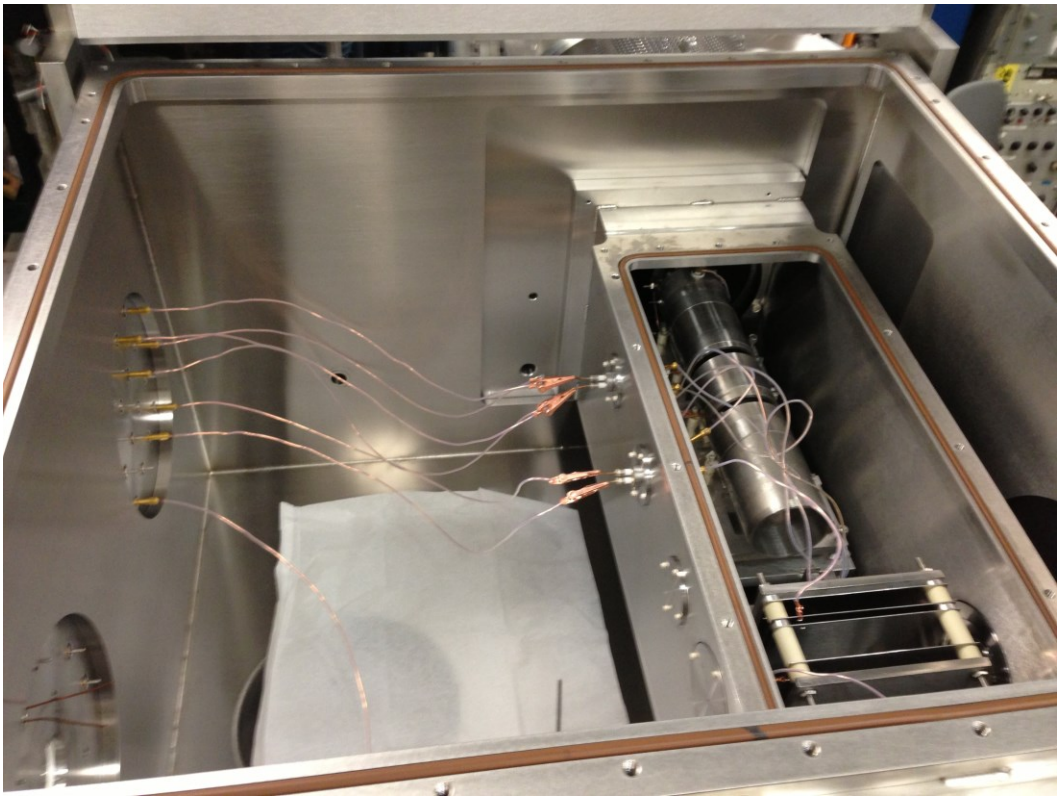

Figure VII.2.3: View inside Chamber 1 and Chamber 2. Newly designed ion extraction plates, deflectors and einzel lens can be seen.

VII.2.1 Extraction Plate Assembly

The extraction plate assembly was designed to be a removable unit that retains alignment when removed and reinstalled. A photo of the assembly is shown in Figure VII.2.4. A labeled overview of the assembly is shown in Figure VII.2.5. The assembly consists of an Adjustable Base (Figure VII.2.6), a Base Plate (Figure VII.2.7), two L Brackets (Figure VII.2.8), and four Extraction Plates (Figure VII.2.9). All dimensions shown are in decimal inch. Every part of the assembly is made from 304 Stainless Steel and the Extraction Plates are spaced between the L Brackets with ceramic spacers.

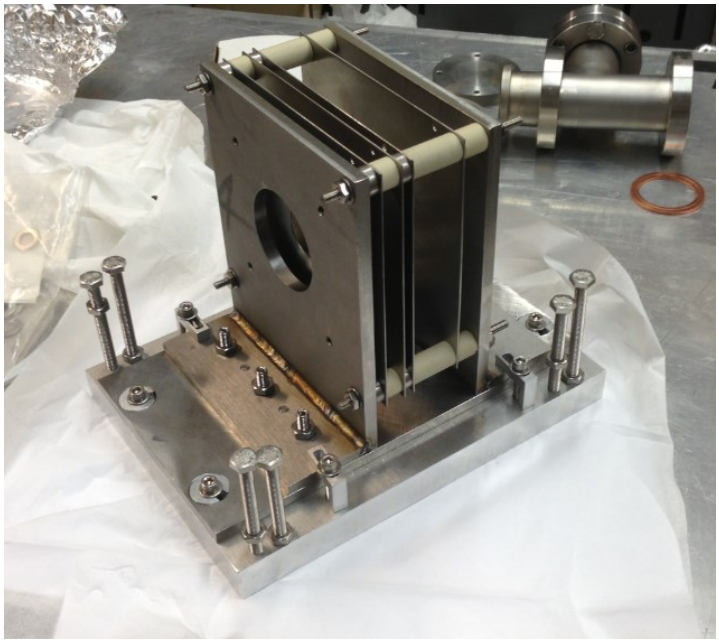

Figure VII.2.4: Extraction Plate Assembly

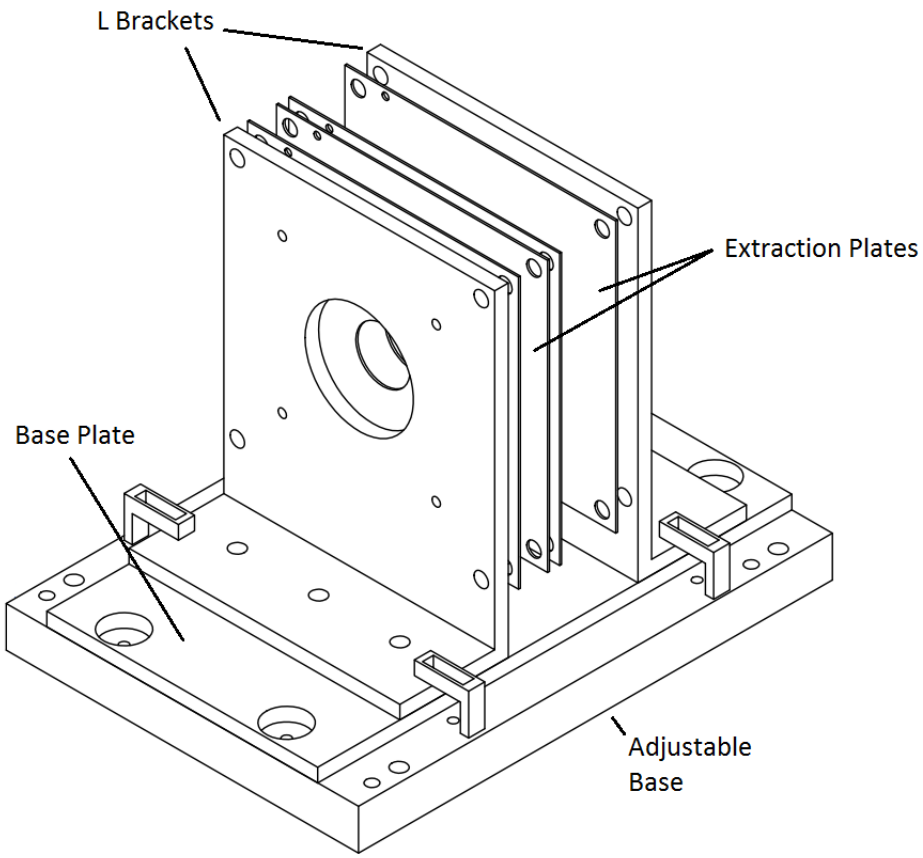

Figure VII.2.5: Extraction Plate Overview

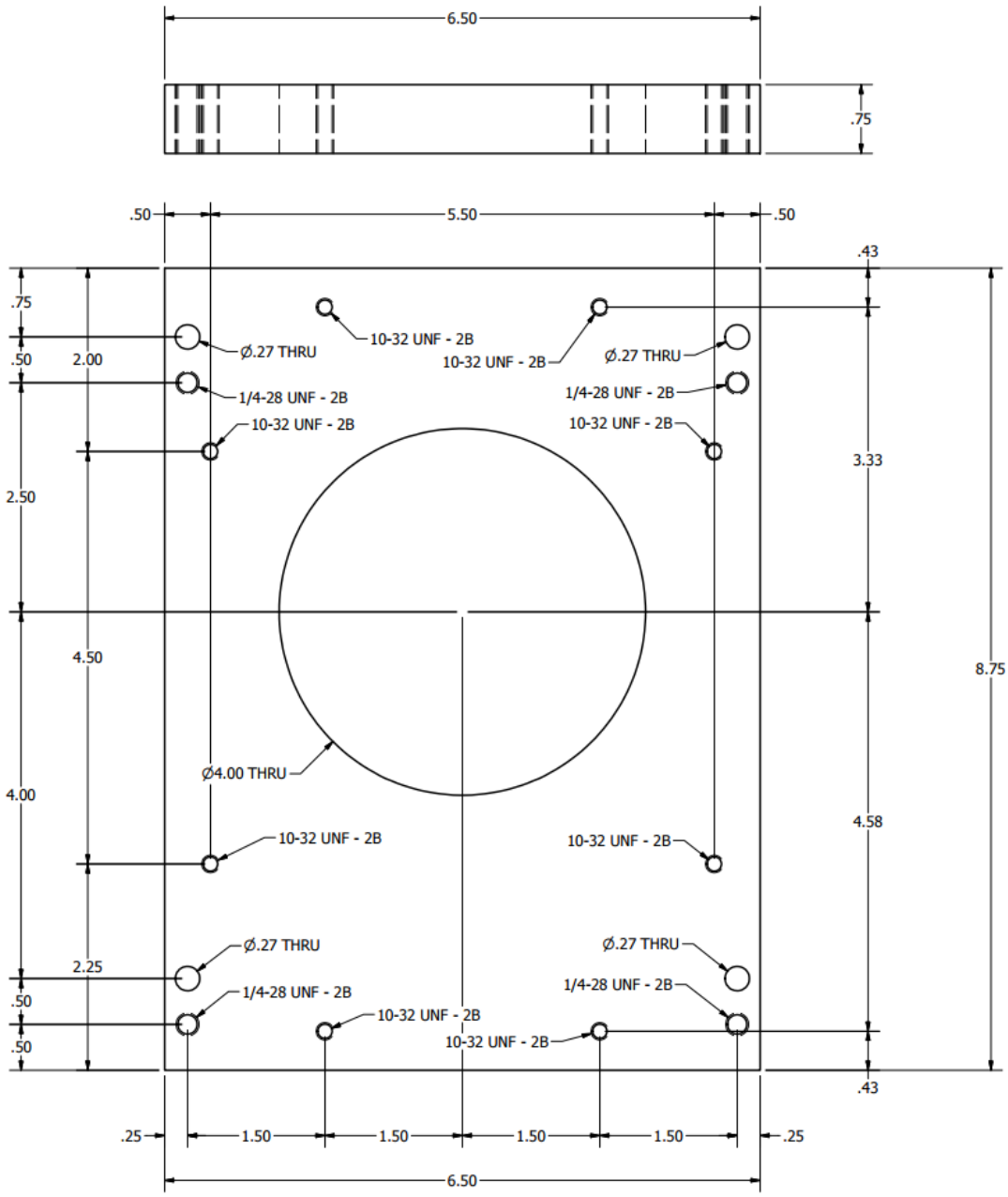

Figure VII.2.6: Extraction Plate Assembly - Adjustable Base

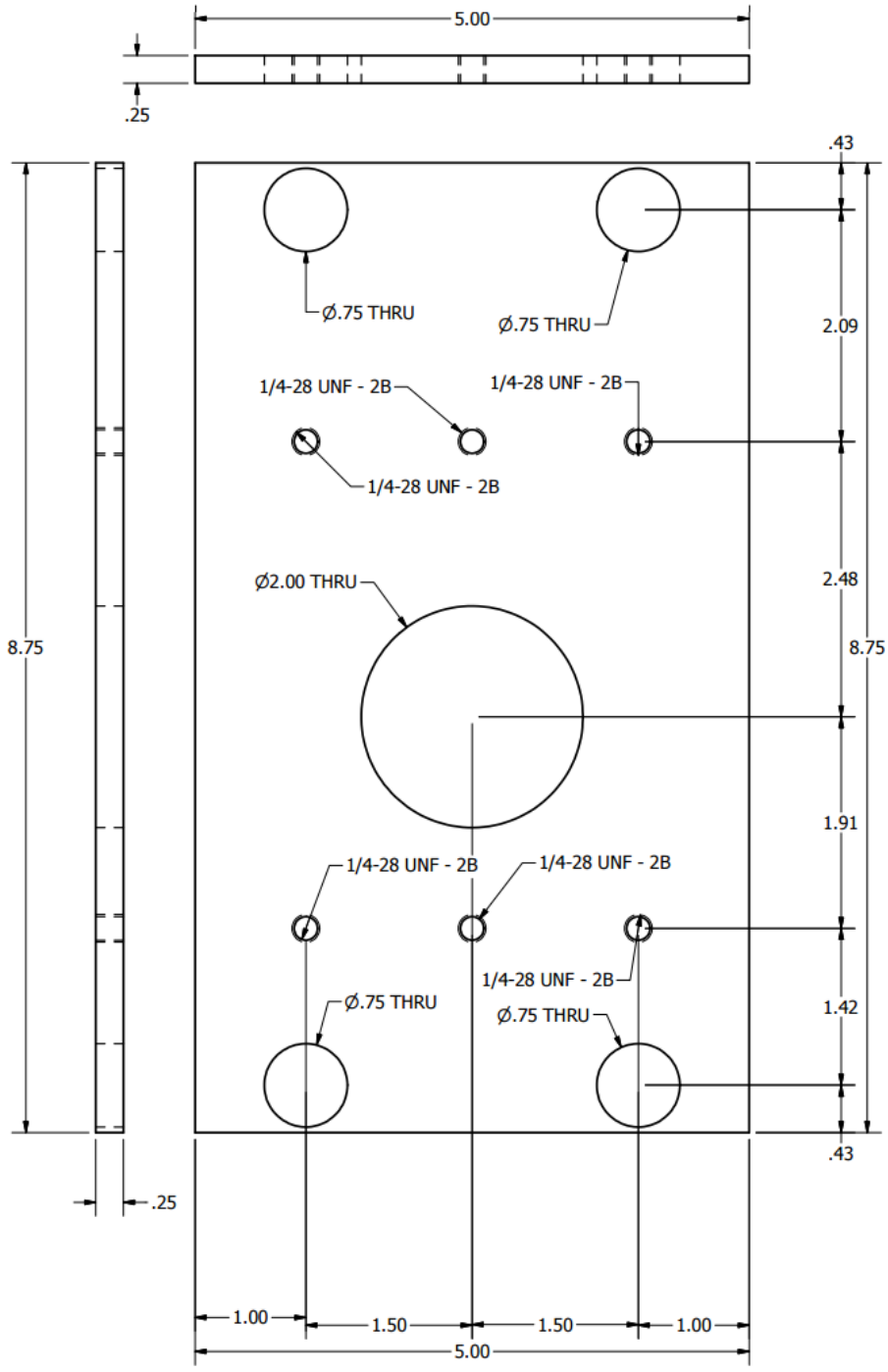

Figure VII.2.7: Extraction Plate Assembly - Base Plate

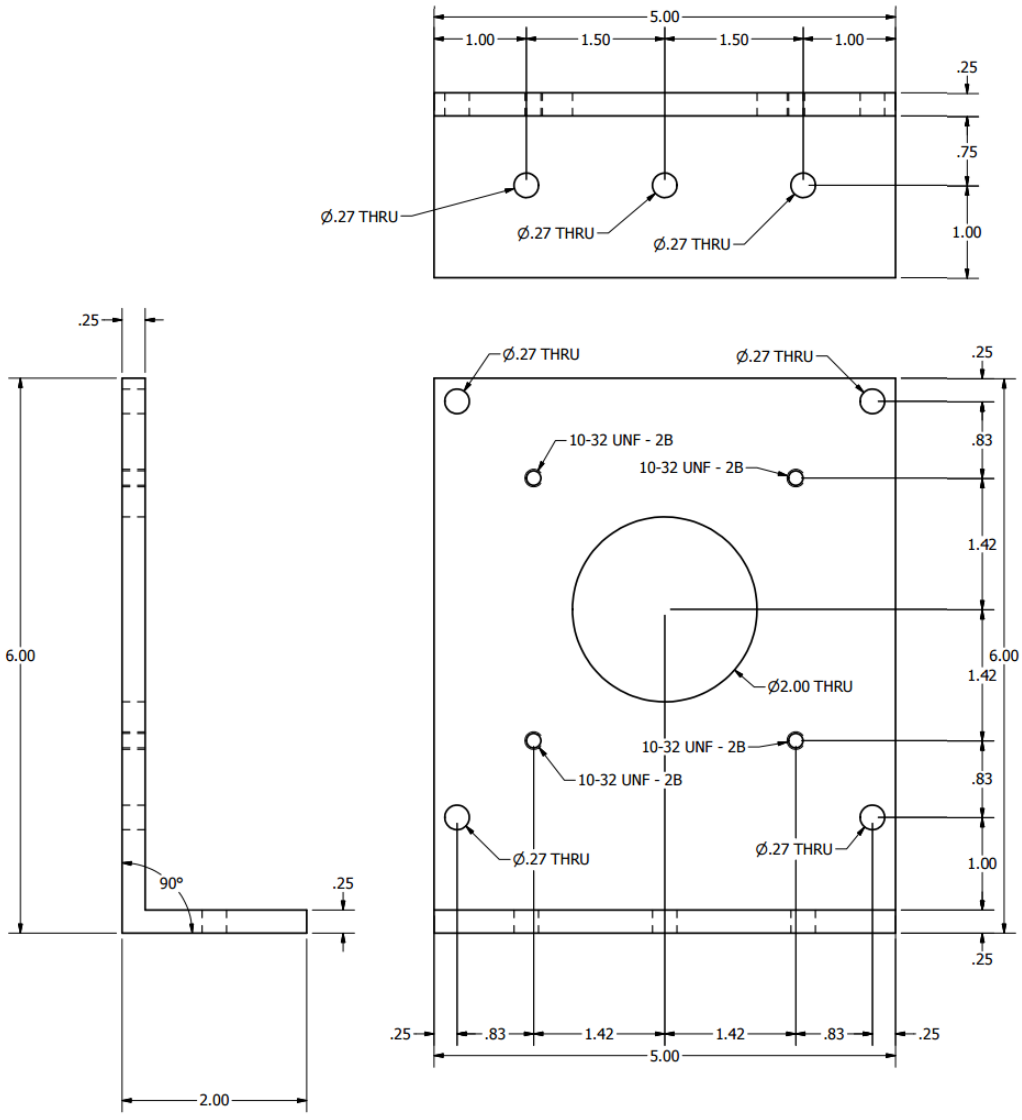

Figure VII.2.8: Extraction Plate Assembly - L Bracket

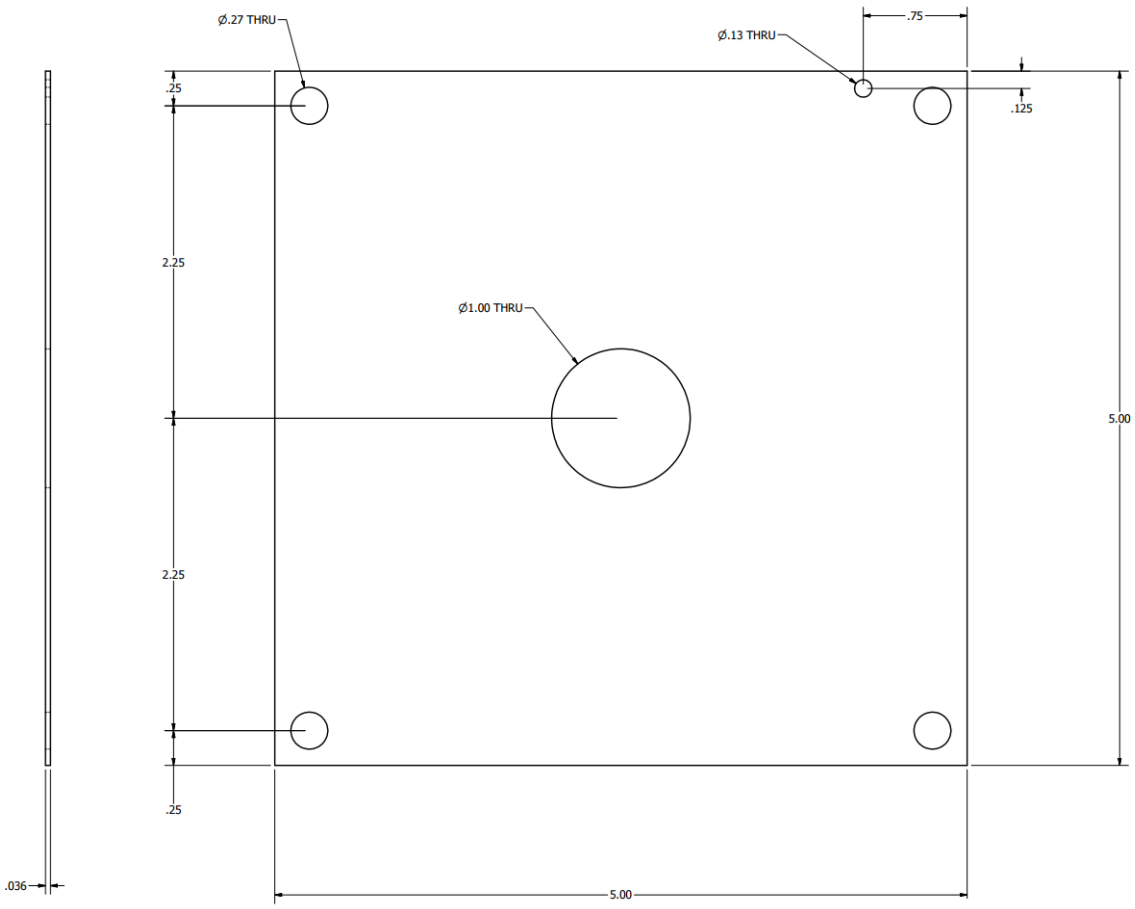

Figure VII.2.9: Extraction Plate Assembly - Extraction Plates

VII.2.2 Conductance Limiting Aperture

Since Chamber 1 surrounds the internal box, a large pressure differential between the two during rough pumping can either stress the walls of the internal box or cause large volumes of air to flow through the small apertures that connect the two vacuum regions. To avoid these undesirable conditions, a conductance limiting aperture was installed. Chamber 1 and the internal box are rough pumped by the same pump and through the same valve, but have different volumes. The conductance limiting piece attempts to scale the rough pump conductance relative to the volume of the two chambers, thus maintaining a lower pressure differential between the two regions during rough pumping.

The volume of Chamber 1 includes the volume of Chamber 1 minus the volume of the internal box, while volume of the internal box needs to include the internal box, the quadrupole tee chamber and the Chamber 2 tee chamber. The volume of Chamber 1 is roughly 2.25 times larger than the combined volume of the internal box and its connected chambers. Chamber 1 is rough pumped through a bellows that has an internal diameter of 1.27 cm and is roughly 25 cm long. The conductance of rough pumping the internal box needs to be 2.25 times smaller than Chamber 1. Since we're more concerned about roughing down from atmosphere to Torr pressures we can use a viscous flow formula for conductance. For air at room temperature:

$$Conductance = 180\frac{D^4}{L}P\ \frac{Liters}{second}$$

where D and L are the diameter and length of a tube in centimeters and P is the average pressure in Torr. However, since we're scaling conductance to a 2.25 ratio we can obtain the following relationship:

$$\left(\frac{1.25^4}{25}\right) = \left(\frac{D^4}{L}\right) 2.25$$

A custom KF centering ring was made to constrict rough pumping for the internal box. It has a thickness of 0.85 cm and a 0.5 cm diameter hole that satisfies the above relationship and scales the conductance between the two vacuum regions.

VII.2.3 Alkali Oven Chamber Interlock

The Alkali Oven Chamber is positioned below Chamber 1. This chamber is continuously evacuated by a turbomolecular pump and kept at a base pressure of $2x10^{-7}$ Torr which permits safe storage of alkali samples. A simple interlock system was added to protect both the turbomolecular pump and alkali in the event of a power outage or roughing pump failure. This circuit is shown in Figure VII.2.10. When the front selector switch is set to "Interlock Enabled" either the loss of electrical power or foreline pressure rising above the set point will close the VAT foreline valve and isolate both the turbomolecular pump and alkali oven chamber from the roughing pump. The turbomolecular pump is powered by a TCP 380 controller which is configured to power down the turbomolecular pump when it senses the VAT foreline valve is closed. This is accomplished by monitoring a sensing relay in the VAT foreline valve. As a safety precaution, the interlock circuit will not automatically reopen the VAT foreline valve once power or foreline vacuum is restored.

To vent the alkali oven chamber:

1. Turn off the TCP 380 controller.
2. Wait 15 minutes for the turbomolecular pump to spin down.
3. With the “Interlock Enabled” selected on the interlock box, slowly open the vent valve on the body of the turbomolecular pump. The VAT foreline valve will close as the alkali oven chamber is brought to atmospheric pressure.

To pump down the alkali oven chamber:

1. Close the vent valve on the body of the turbomolecular pump.
2. Change the selector switch on the interlock box to “Hold Foreline Valve Open”
3. Wait for the foreline pressure to drop below 0.5 Torr.
4. Turn on the TCP 380 controller and switch the interlock box back to “Interlock Enabled”

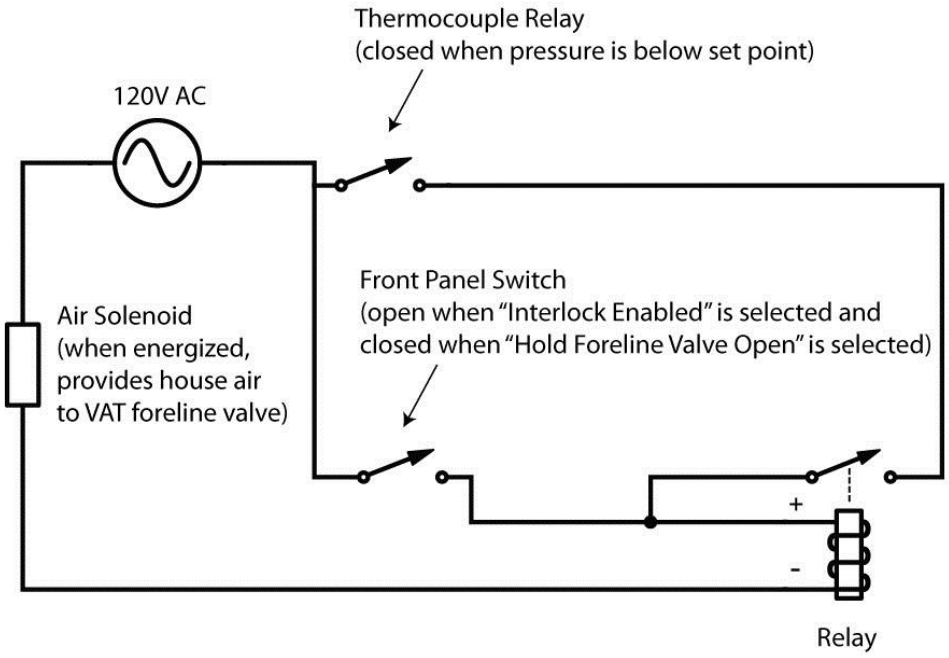

Figure VII.2.10: Alkali Chamber Interlock Circuit

VII.3 Dye Laser Notes

Two Quanta Ray PDL-2 dye lasers are used to optically excite the alkali beam and generate Rydberg atoms. Each dye laser is pumped by a Continuum Surelite II Nd:YAG laser.

For exciting potassium to the $^2P_{3/2}$ state, one dye laser is operated with LDS751 dye in ethanol and is parked at 766.70 nm. This output of this laser is in the near infrared region and is referred to as the "red dye laser". The LDS751 dye is pumped with 532nm light and usually lasts several months of daily use before needing to be replaced. When tuned to 766.70 nm the grating counter should read 31129. Additionally, the $^2P_{1/2}$ state (at

770.10 nm) was found to have a counter reading of 31269. This counter value responds linearly with wavelength and has the following relationship: (wavelength in nm) = (counter reading / 40.6).

For exciting potassium from the $^2P_{3/2}$ state to a Rydberg level, a second dye laser is operated with either Coumarin 480 or Coumarin 460 dye in ethanol. With either dye, the output of this laser is blue and is referred to as the "blue dye laser." Both Coumarin dyes are pumped with 355nm light and degrade rapidly with use, sometimes needing to be replaced after one day. Coumarin 460 has a useful tuning curve from about 453 nm to about 461 nm. For potassium, this encompasses ionization down to n=19. Coumarin 480 has a useful tuning curve from about 461 nm to about 480 nm which encompasses n=19 down to n=10.

Currently, the output of the red dye laser is directed co-linearly with the alkali beam. Initial alignment is done via the top and bottom apertures of the internal box. The blue laser is directed co-linearly with the target neutral beam. Here, initial alignment is accomplished by maximizing the beam passing through the skimmer. Once RET anion signal is found, both laser's alignment is re-optimized to maximize the anion signal.

One useful technique for finding Rydberg levels is by detecting potassium cations. With the blue dye laser parked at the blue edge of its tuning curve with Coumarin 460, one should be able to find both the $^2P_{1/2}$ and $^2P_{3/2}$ states of potassium through tuning the red dye laser and monitoring production of potassium cations. Once the $^2P_{3/2}$ state is found, the wavelength of the blue dye laser can be tuned to longer wavelengths until

Rydberg states are found. Although this is a three photon process ($^2S \rightarrow {}^2P_{3/2} \rightarrow$ Rydberg level $\rightarrow$ ionization), the resonant nature of this ionization produces large signals of K^+.

A Burleigh 4500 wavemeter is also available to analyze the output of either dye laser. Typically, a pick off optic used at the output of the blue dye laser diverts ~5% of the blue laser light into the wavemeter. This permits wavelength monitoring during experimental runs.

VII.4 Experimental Conditions and Performance

The three following anion systems listed below are shown as examples of anions made with RET.

VII.4.1 $(H_2O)_n^-$

Negatively charged water clusters were successfully generated via RET. A mass spectrum is shown in Figure VII.4.1 and experimental conditions are listed in Table VII.4.1.

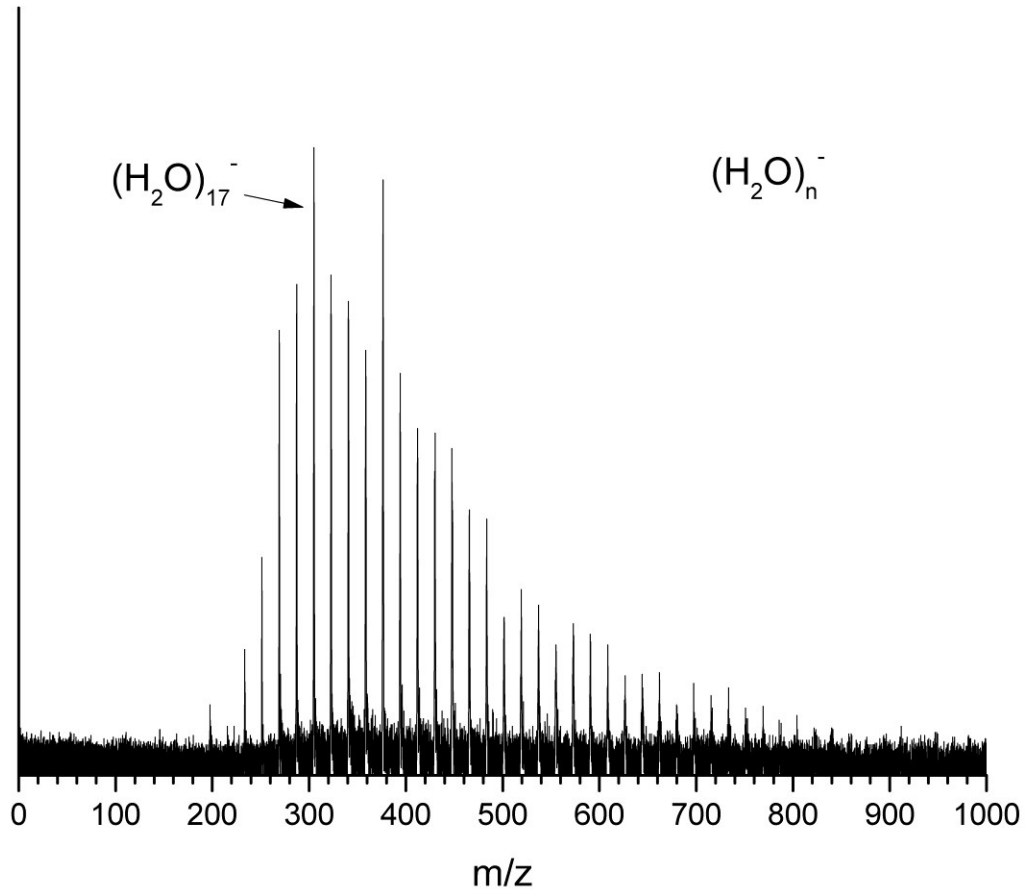

Figure VII.4.1: Mass Spectrum of (H2O)n- generated with RET

Table VII.4.1: Experimental Conditions (with H_2O in pulsed valve)

Pulsed valve orifice size	0.8 mm
Pulsed valve backing pressure	40 psig Helium
Horizontal deflector 1 (all other deflectors are at 0V)	+100V
"Blue" Dye laser	467.75 nm at 3 mJ
"Red" Dye laser	$^2P_{3/2}$ transition at 3 mJ
Pulse Valve Opening Time	-840.000 µs
Q-Switch for Nd:YAG pumping “Blue” Dye Laser	-0.138 µs
Q-Switch for Nd:YAG pumping “Red” Dye Laser	0.000 µs
Extraction Plates	5.000 µs
Intensity of $(H_2O)_{17}^-$	0.0004 Volts/cycle

VII.4.2 SF_6^-

SF_6 has a very high zero electron kinetic energy cross section and is perhaps the easiest anion to make with RET. Shown below in Figure VII.4.2 is a measurement of the SF_6^- anion intensity as a function of the "blue" dye laser wavelength. This spectrum shows the insensitivity to Rydberg levels that is characteristic of a valance anion. Intensities for SF_6^- can reach in excess of 0.5 V/cycle.

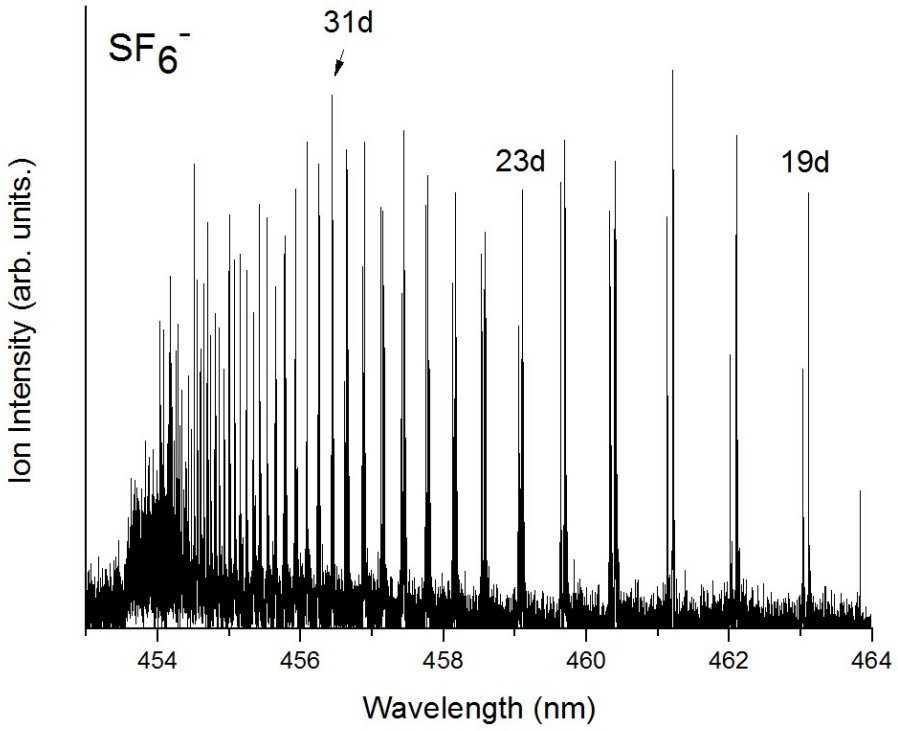

Figure VII.4.2: SF_6^- anion signal as a function of Rydberg level

VII.4.3 Dipole Bound Acetonitrile Anions

Dipole bound anions can be formed by RET in a "resonant" manner. Charge transfer between a Rydberg atom and polar molecule has been described in terms of a curve crossing model.[6] Experimentally, only a narrow range of Rydberg levels (dependent on the magnitude of the dipole moment) will generate a given dipole bound anion. While acetonitrile does not form a stable valance anion, its high dipole moment of 3.92 Debye can capture an electron. Figure VII.4.3 shows the Rydberg level dependence of the acetonitrile dipole bound anion.

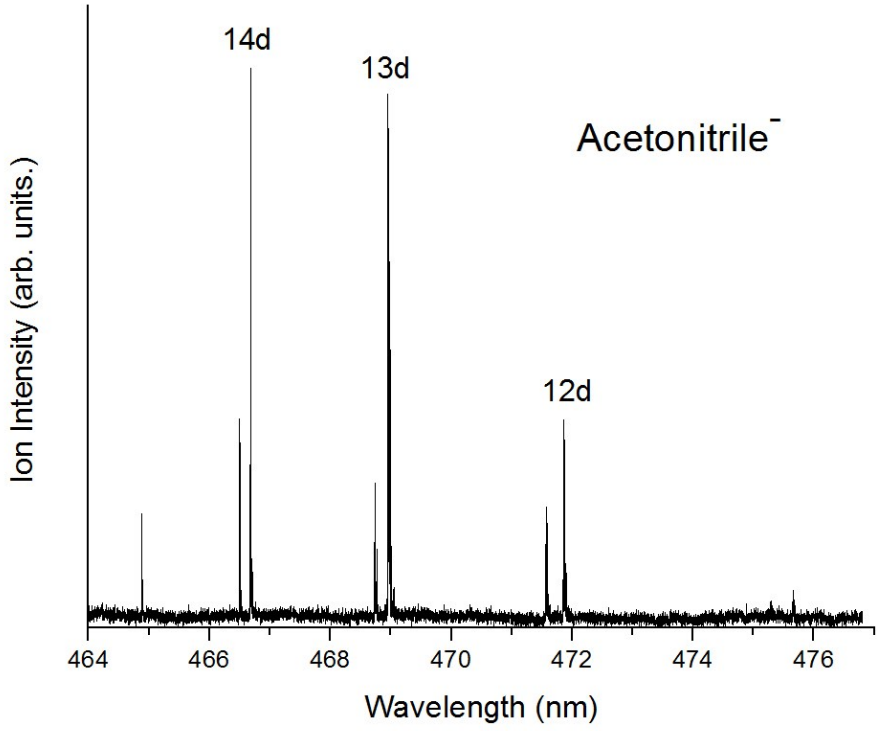

Figure VII.4.3: Acetonitrile anion signal as a function of Rydberg level

Dipole bound electrons are held in large, diffuse orbitals and induce nearly zero geometry change. As a result, the photoelectron spectra of dipole bound anions consist of a single, sharp, low binding energy transition. Using our velocity map imaging setup and 1.1 eV photons (from the 1st Harmonic of Nd:YAG laser), we recorded the photoelectron spectrum of the acetonitrile anion generated by RET. The spectrum is shown in Figure VII.4.4 and is consistent with that of a dipole bound species.

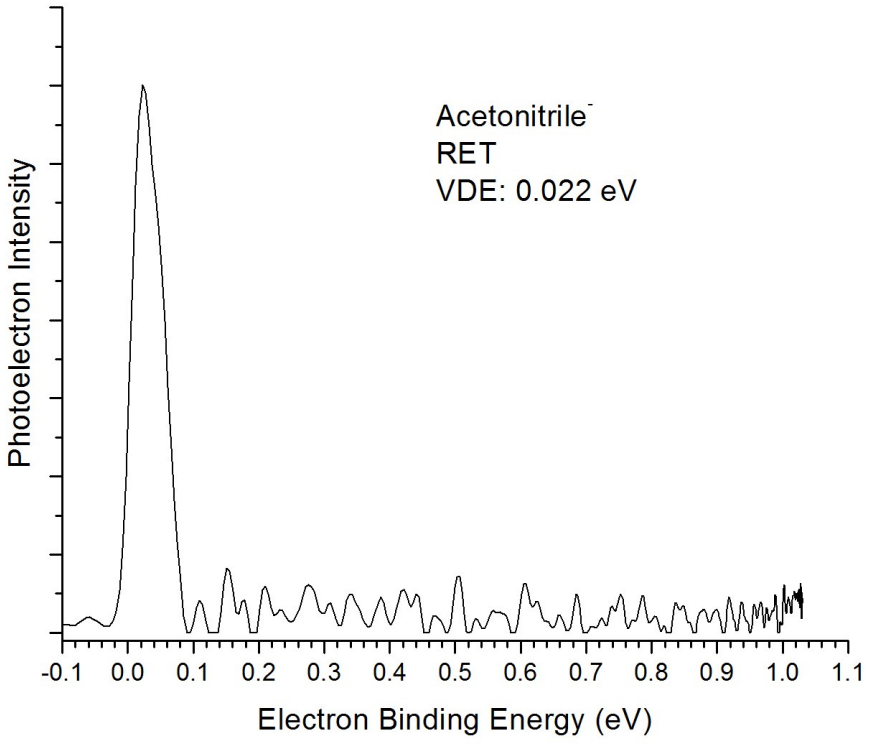

Figure VII.4.4: Photoelectron Spectrum of Acetonitrile-

References

1. T. Kondow, J. Phys. Chem. **91**, 1307-1316, (1987).

2. C. Desfrancois, N. Khelifa, A. Lisfi, and J. P. Schermann, J. Chem. Phys. **96**, 5009 (1992).

3. T. Kraft, M.-W. Ruf, and H. Hotop, Z. Phys. D **14**, 179-185 (1989).

4. H. S. Carman, Jr., C. E. Klots, and R. N. Compton, J. Chem. Phys. **90**, 2580 (1989).

5. F. B. Dunning, J. Phys. Chem. **91**, 2244-2249 (1987).

6. C. Desfrançois, Phys. Rev. A **51**, 3667 (1995).

JACOB DAVID GRAHAM

Contact

Department of Chemistry
Johns Hopkins University
Baltimore, MD 21218

Email: jdgraham@jhu.edu
Mobile: (239) 980-1987

Education

Ph.D. Chemistry	2015	Johns Hopkins University Advisor: Dr. Kit Bowen Thesis: "Photoelectron Spectroscopy Studies of Anionic Clusters: CO_2 Reduction, Metal Hydrides, Low Barrier Hydrogen Bonding, and Solvent Stabilization"
M.A. Chemistry	2012	Johns Hopkins University
B.S. Chemistry	2009	University of Mississippi Advisor: Dr. Nathan Hammer

Awards

2014 Owens Graduate Summer Fellowship

2009 ACS Undergraduate Award in Inorganic Chemistry

Walker Undergraduate Scholarship

Teaching Experience

Spring 2011	Teaching Assistant for Introductory Chemistry II
Spring 2010	Teaching Assistant for Introductory Chemistry II
Fall 2009-10	Teaching Assistant for Physical Chemistry Laboratory III

Presentations

"Photoelectron Spectra of Porphyrin Anions: A Preliminary Test for Theory," J. Graham, A. Buytendyk, J. Gould, K. Bowen, Nanoporous Materials Genome Center All-Hands Meeting 2014, St. Paul, MN

"Aluminum hydride clusters and their derivatives: anion photoelectron spectroscopic studies," J. Graham, S. Li, A. Grubisic, K. Bowen, P. Jena, G. Gantefoer, H. Schnoeckel, XVIIth Symposium on Atomic, Cluster and Surface Physics 2010, Obergurgl, Austria

Publications

J. Graham, A. Buytendyk, S. Kim, M. Pederson and K. H. Bowen, "Carbon Dioxide is Tightly Bound in the $[Co(Pyridine)(CO_2)]^-$ Anionic Complex," *in preparation.*

X. Zhang, J. Graham, H. Wang and K. H. Bowen, "Solvent stabilization of carbonyl anions," *in preparation*.

A. Buonaugurio, J. Graham, A. Buytendyk, Y. Wang and K. H. Bowen, "Photoelectron spectroscopy of the proton transferred 1,8-bis(dimethylamino)naphthalene HCl complex," *in preparation.*

A. Buytendyk, J. Graham, K. Collins, K. Bowen, C. Wu and J. Wu, "The Hydrogen Bond Strength of the Phenol-Phenolate Anionic Complex: A Computational and Photoelectron Spectroscopic Study," *accepted to Physical Chemistry Chemical Physics.*

A. Buytendyk, J. Graham, J. Gould and K. H. Bowen, “Parent Anions of Iron, Manganese, and Nickel Tetraphenyl Porphyrins: Photoelectron Spectroscopy and Computations,” *Journal of Physical Chemistry A* **119**, 8643-8646 (2015).

J. Graham, A. Buytendyk, Y. Wang, S. K. Kim and K. H. Bowen, “CO_2 Binding in the (Quinoline-CO_2)$^-$ Anionic Complex,“ *Journal of Chemical Physics,* **142**, 234307 (2015).

A. M. Buytendyk, Y. Wang, J. D. Graham, A. K. Kandalam, B. Kiran and K. H. Bowen, "Photoelectron spectrum of a polycyclic aromatic nitrogen heterocyclic anion: quinoline−,” *Molecular Physics* (2015). DOI: 10.1080/00268976.2014.1003261

J. T. Kelly, S. Xu, J. Graham, J. M. Nilles, D. Radisic, A. M. Buonaugurio, K. H. Bowen, N. I. Hammer and G. S. Tschumper, "Photoelectron Spectroscopic and Computational Study of Hydrated Pyrimidine Anions," *Journal of Physical Chemistry A*, **118**, 11901-11907 (2014).

A. Buonaugurio, J. Graham, A. Buytendyk, K. H. Bowen, M. R. Ryder, Z. G. Keolopile, M. Haranczyk and M. Gutowski, "Communication: Remarkable electrophilicity of the oxalic acid monomer: An anion photoelectron spectroscopy and theoretical study," *Journal of Chemical Physics*, **140**, 221103 (2014).

J.D. Graham, A. M. Buytendyk , X. Zhang , E. L. Collins , K. Boggavarapu , G. Gantefoer , B. W. Eichhorn , G. L. Gutsev , S. Behera , P. Jena and K. H. Bowen, “Alanate Anion, AlH_4^-: Photoelectron Spectrum and Computations," *The Journal of Physical Chemistry A,* **118**, 8158–8162 (2014).

A. Buytendyk, J. Graham, H. Wang, X. Zhang, E. Collins, Y. J. Ko, G. Gantefoer, B. Eichhorn, A. Regmi, K.Boggavarapu and K. H. Bowen, "Photoelectron Spectra of the MgH^- and MgD^- Anions," *International Journal of Mass Spectrometry,* **365-366**, 140-142 (2014).

J. D. Graham, A. M. Buytendyk, D. Wang, K. H. Bowen and K. D. Collins, "Strong, Low Barrier Hydrogen Bonds may be Available to Enzymes," *Biochemistry*, **53**, 344–349 (2014).

J. D. Graham and N. I. Hammer, "Photocatalytic Water Splitting and Carbon Dioxide Reduction," in *Handbook of Climate Change Mitigation*, Springer, 2012.

D. Wang, J.D. Graham, A.M. Buytendyk and K.H. Bowen, "Photoelectron spectroscopy of the molecular anions, Li3O- and Na3O-," *Journal of Chemical Physics*, **135**, 164308 (2011).

D. J. Scardino, M. McDowell, J. D. Graham and N. I. Hammer, "The Multiphoton Ionization Spectrum of Methyl Iodide Revisted: 1.67 - 2.2 eV Excitation," *Journal of Atomic and Molecular Science*s, **2**, 93-98 (2011).